Azimuthal Dependence of Pion Interferometry in Au + Au Collisions at a Center of Mass Energy of $130 AGeV$

DISSERTATION

Presented in Partial Fulfillment of the Requirements for

the Degree Doctor of Philosophy in the

Graduate School of The Ohio State University

By

Randall C. Wells, B.S., M.S.

* * * * *

The Ohio State University

2002

Dissertation Committee:

Michael A. Lisa, Adviser

Richard Furnstahl

Thomas Humanic

Douglas Schumacher

Approved by

Adviser
Department of Physics

ABSTRACT

The study of two-pion Bose–Einstein correlations provides a tool to extract both spatial and dynamic information regarding the freeze–out configuration of the emission region created in heavy ion collisions. Noncentral heavy ion collisions are inherently spatially and dynamically anisotropic. The study of such collisions through the ϕ dependence of the HBT radii, R^2_{ij}, relative to the event plane allows one to observe the source from all angles, leading to a richer description of the interplay between geometry and dynamics.

The initial heavy ion running of the Relativistic Heavy Ion Collider (RHIC) at Brookhaven National Laboratory provided Au + Au collisions at $130GeV$. The focus of the heavy ion program at RHIC is the search for a new state of strongly interacting matter, the quark gluon plasma (QGP). STAR is a large acceptance detector at RHIC with azimuthal symmetry, allowing the study of a large variety of observables on an event–by–event basis to provide a better characterization of the freeze–out conditions. The detector geometry for the first year's data consisted of a time projection chamber (TPC) immersed in a $0.25T$ magnetic field oriented along the symmetry axis to provide identification of particles with transverse momenta $p_T \gtrapprox 100MeV/c$.

The focus of this dissertation is the study of the ϕ dependence of the transverse HBT radii from $\pi^-\pi^-$ & $\pi^+\pi^+$ correlations in non–central collisions. 2^{nd} order oscillations are observed in all transverse radii ($R^2_o(\phi)$, $R^2_s(\phi)$, and $R^2_{os}(\phi)$). The oscillations

are found to be consistent in phase and magnitude to both RQMD and hydrodynamic predictions, yet both models (over)underpredict $(R_o^2)R_s^2$ whose relative size indicates a short emission time–scale. A modified blast wave prameterization is successful at reproducing a variety of observables at RHIC (i.e. particle spectra, $v_2(p_T)$, $R_{ij}^2(p_T)$, and $R_{o,s,os}^2(\phi)$) with a univeral set of freeze–out parmeters. The results describe a freeze–out geometry extended out–of–plane indicative of a short source life–time.

ACKNOWLEDGMENTS

This is the culmination of many years of study and in those years I've come across many people I'd like to extend my gratitude. STAR is a collaboration of some 400+ members most of whom I have not been able to get to know. I'd like to begin with thanks to everyone involved in the success of the STAR experiment. Without their hard work and dedication to the experiment, this dissertation would not be possible. In particular, I'd like to thank David Hardtke and Iwona Sakredja for helping to introduce me to the STAR software and Frank Laue for keeping me up to date. I'd like to thank the members of the HBT physics–working–group especially the co-convenors, John Cramer and Sergey Panitkin for providing an independent source of comments and criticisms of my analysis. In addition, thanks to both Raimond Snellings and Art Postanzer for assisting in the early development of the analysis.

Several people have had a large impact on my progress as a student of physics. First, I'd like to thank the physics faculty at UW-Parkside especially my friend and advisor, Pirooz Mohazzabi. Helen Caines also deserves many thanks for her endless help and conversations which helped me to better understand the detector and physics of STAR.

I'd also like to thank all of the friends that I have made in graduate school. They have been a source of support while providing laughs and enjoyment. Special thanks to Matt Fulkerson, John Skinta, and Robert Willson.

These acknowledgements would not be complete without thanks to my advisor, Michael Lisa. His ability to absorb my endless plots and provide questions was instrumental in helping me learn about the intricacies of interferometry.

I'd like to thank all of the people at the Van de Graaff including Selemon Bekele, Howard Dyke, Tom Humanic, Ivan Kotov, Alex Murphy, Bjørn Nilsen, Mercedes López Noriega, Dennis Reichhold, Florence Shanks, and Mary Smith for making the VdG a nice place to spend my days.

I'd also like to say thanks to my family: Mom, Rex, Alison, Spencer, David, Lisa, Gunnar, Peyton, Shea, and of course Mandy!

VITA

June 26, 1973	Born - Racine, WI
1996	B.S. Physics & Mathematics University of Wisconsin - Parkside Kenosha, WI
1996-1997	Graduate Teaching Assistant, Department of Physics The Ohio State University Columbus, OH
1998	M.S. Physics The Ohio State University Columbus, OH
1998-present	Graduate Research Assistant, Department of Physics The Ohio State University Columbus, OH

PUBLICATIONS

Research Publications

Centrality dependence of high p_T hadron suppression in Au + Au collisions at $\sqrt{s_{NN}} = 130GeV$
C. Adler *et al.* (STAR Collaboration), Phys. Rev. Lett. **89** 202301 (2002)

Elliptic flow from two– and four–particle correlations in Au + Au collisions at $\sqrt{s_{NN}} = 130GeV$
C. Adler *et al.* (STAR Collaboration), Phys. Rev. C. **66** 034904 (2002)

Azimuthal anisotropy of K^0_S and $\Lambda + \overline{\Lambda}$ production at mid-rapidity from Au+Au collisions at $\sqrt{s_{NN}} = 130$GeV
C. Adler *et al.* (STAR Collaboration), Phys. Rev. Lett. **89** 132301 (2002)

Mid–rapidity Λ and $\overline{\Lambda}$ Production in Au + Au Collisions at $\sqrt{s_{NN}} = 130$GeV
C. Adler *et al.* (STAR Collaboration), Phys. Rev. Lett. **89** 092301 (2002)

Mid–rapidity ϕ production in Au + Au collisions at $\sqrt{s_{NN}} = 130$GeV
C. Adler *et al.* (STAR Collaboration), Phys. C **65** 041901(R) (2002)

Measurement of Inclusive Antiprotons from Au + Au Collisions at $\sqrt{s_{NN}} = 130$GeV
C. Adler *et al.* (STAR Collaboration), Phys. Rev. Lett. **87** 262302–1 (2001)

$\overline{d}$ and $^3\overline{He}$ Production in $\sqrt{s_{NN}} = 130$GeV Au + Au Collisions
C. Adler *et al.* (STAR Collaboration), Phys. Rev. Lett. **87** 262301–1 (2001)

Identified Particle Elliptic Flow in Au + Au collisions at $\sqrt{s_{NN}} = 130$GeV
C. Adler *et al.* (STAR Collaboration), Phys. Rev. Lett. **87** 182301 (2001)

Model–independent Source Imaging Using Two–Pion Correlations in 2 to 8 AGeV Au + Au Collisions
S. Panitkin *et al.* (E895 Collaboration), Phys. Rev. Lett. **87** 112304 (2001)

Multplicity distribution and spectra of negatively charged hadrons in Au + Au collisions at $\sqrt{s_{NN}} = 130$GeV
C. Adler *et al.* (STAR Collaboration), Phys. Rev. Lett. **87** 112303 (2001)

Pion Interferometry of $\sqrt{s_{NN}} = 130$GeV Au + Au Collisions at RHIC
C. Adler *et al.* (STAR Collaboration), Phys. Rev. Lett. **87** 082301 (2001)

Midrapidity Antiproton-to-Proton Ratio from Au + Au Collisions at $\sqrt{(s_{NN})} = 130$GeV
C. Adler *et al.* (STAR Collaboration), Phys. Rev. Lett. **86** 4778 (2001)

Elliptic Flow in Au + Au Collisions at $\sqrt{(s_{NN})} = 130$GeV
K.H. Ackermann *et al.* (STAR Collaboration), Phys. Rev. Lett. **86** 402 (2001)

Azimuthal Dependence of Pion Interferometry at the AGS
M.A. Lisa *et al.* (E895 Collaboration), Phys. Lett. **B496** 1 (2000)

The STAR Silicon Drift Detector
S. Pandey *et al.* (STAR Collaboration), Nucl. Phys. **A661** 686c (1999)

The STAR Time Projection Chamber
J. Thomas *et al.* (STAR Collaboration), Nucl. Phys. **A661** 681c (1999)

A Forward TPC for STAR
A. Schüttauf *et al.* (STAR Collaboration), Nucl. Phys. **A661** 677c (1999)

Results from the Experiment E895 at the BNL AGS
G. Rai *et al.* (E895 Collaboration), Nucl. Phys. **A661** 162c (1999)

Extraction of Boltmann dynamics from a gas of constant speed particles
P. Mohazzabi, J.R. Schmidt, R.C. Wells, Can. Jour. Phys. **75** 67 (1997)

FIELDS OF STUDY

Major Field: Physics

TABLE OF CONTENTS

Page

LIST OF FIGURES

LIST OF TABLES

CHAPTER 1

HEAVY ION PHYSICS

1.1 Introduction

In 1963 two Bell Labs scientists, Arno Penzias and Robert Wilson, discovered and measured the cosmic microwave background radiation which resulted in the acceptance of the Big Bang model of the origin of the universe over competing theories such as the steady state theory [13]. The discovery of this 2.7K remnant temperature of the universe agreed with a prediction by Dicke of 3K. In the late 1980s a new series of measurements such as COBE were begun to measure anisotropies in the background radiation to probe further back, with better resolution, towards the earliest moments after the Big Bang [14]. The Big Bang theory postulates that the universe was created from the explosion of a point singularity of infinite density. The subsequent expansion and cooling allowed the particle constituents to condense from an initial soup of fermions, photons, quarks, and gluons to the present composition of the universe where quarks and gluons are the composite particles of mesons and baryons. Through the study of the structure of the microwave background radiation, cosmologists are attempting to gain a better understanding of the conditions present shortly after the creation of the universe.

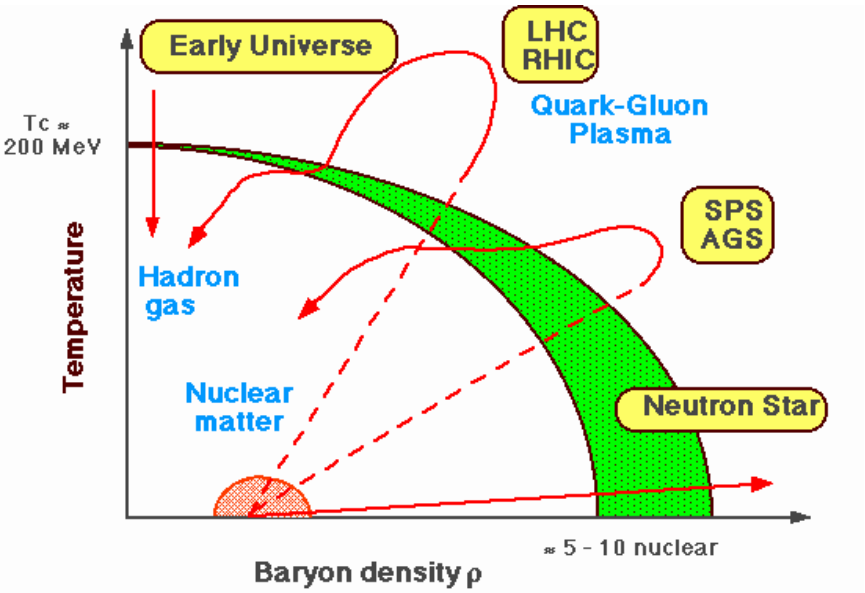

Figure 1.1: The phase diamgram for nuclear matter.

The study of relativistic heavy ion collisions is also allowing scientists to probe the conditions of the early universe. Present theoretical understanding suggests the presence of a phase transition for nuclear matter in which the building blocks (quarks and gluons) become asymptotically free from the strong nuclear force constraining their movement within a nucleon. This phase is commonly referred to as a quark gluon plasma, QGP. A quark gluon plasma constitutes a new state of matter and as such requires thermalization to characterize the bulk properties of the system. The use of heavy ions provides an extended system in collisions necessary to produce a large volume of quark matter. A phase diagram for nuclear matter is shown in Fig. 1.1. Trajectories in the temperature–baryon density plane predicted for both RHIC and the LHC are also indicated. Modern lattice theory suggests that a temperature of

$\sim 2.3 \times 10^8 K$ is necessary to produce this phase transition for no net baryon density, $\mu_B = 0$. The conditions necessary for this phase transition (high temperature and/or high matter density) are thought to have existed shortly after the big bang, ($t \sim 10^{-6} s$), and also in the cores of neutron stars. To create these conditions in a laboratory setting requires the use of high energy collisions between very heavy nuclei. By compressing the matter within the collision, it is thought that dense regions undergo a phase transition to a QGP and allow one to create and study conditions present shortly after the big bang. The expected evolution of the nuclear matter in heavy ion collisions is shown in Fig. 1.2. The two nuclei collide at approximately the spped of light and enter along the light cone trajectories. The pre–equilibrium that immediately follows describes the matter prior to thermalization. At sufficient energy density, a QGP is then formed which cools and re–hadronizes during the mixed phase. This mixed phase fully hadronizes and subsequently freezes out to free streaming particles.

Evidence confirming a phase transition is expected to come from a variety of measurements. The STAR detector was designed to correlate a variety of observables on an event–by–event basis. In this way, the STAR experiment is well positioned to provide evidence confirming the existence of a QGP. Of most relevance to this thesis is the prediction of a rapid increase in the emission life time of the particle source should a QGP form. Within a hadronic gas, one has $(n_f^2 - 1)$ degrees of freedom (DOF) where $T \sim 0$. When matter undergoes a phase transition to a QGP, the number of DOF increase to $(16 + \frac{21}{2} n_f)$ [1]. Here, n_f represents the number of quark flavors. As the fireball cools, this difference in the number of DOF lengthens the time for the nuclear matter to hadronize as the quarks must realign themselves inside hadrons

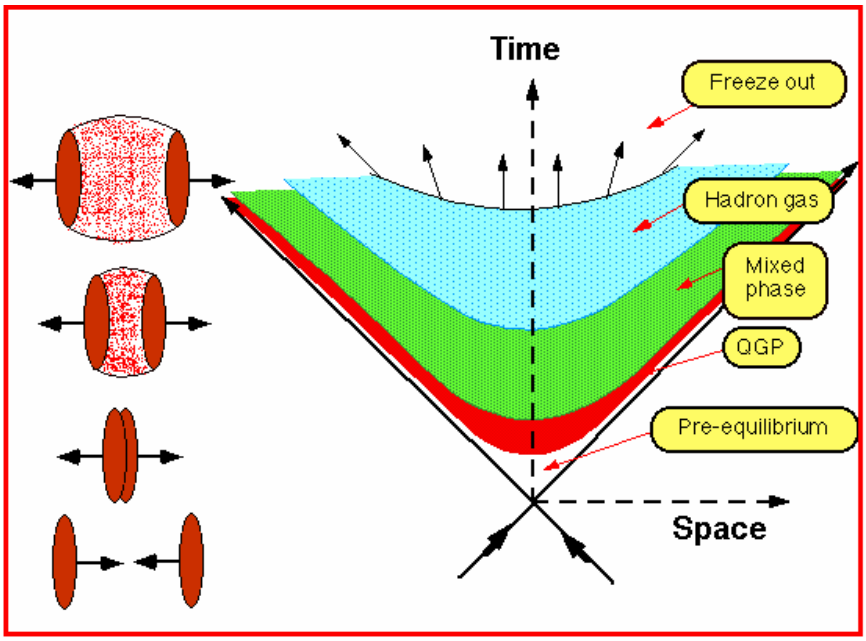

Figure 1.2: Theoretical evolution of a heavy ion collisions.

before freeze–out. Particle interferometry measures the spacetime structure of the emission region and thereby provides information regarding the emission timescale. A large increase in the timescale of particle emission was suggested by Pratt, Csörgő, and Zimányi as an indicator of a phase transition to a QGP [15]. Gyulassy and Rischke have shown that a phase transition induces in hydrodynamic calculations a strong increase in emission timescale and that this increase is generic, independent of implementation details [16] As discussed in the next chapter, an observable sensitive to this timescale is the ratio of two "HBT radii" R_o/R_s. Fig. 1.3 shows the ratio R_o/R_s, a measure of emission timescale, from a hydrodynamic simulation with and without a phase transition to QGP, showing an increase when one includes a phase transition. As discussed in Chapter 2, the present colliding energy dependence of this

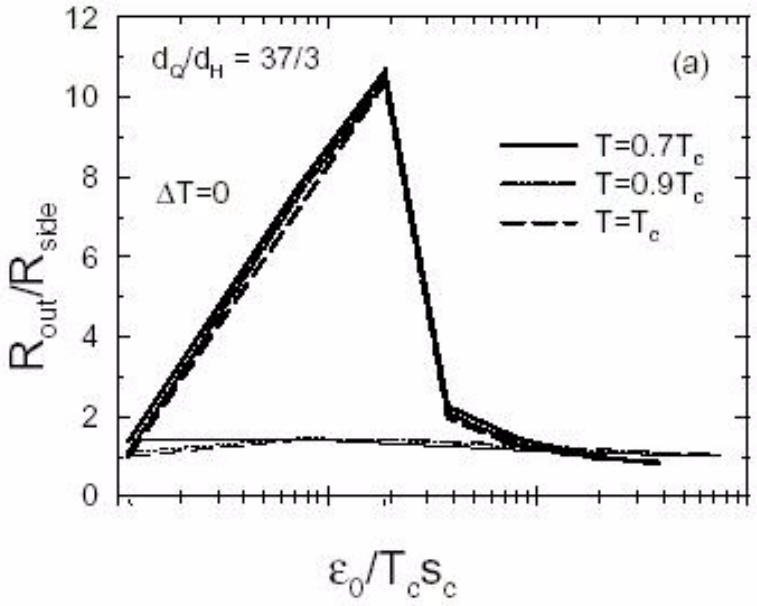

Figure 1.3: The ratio of R_o to R_s for a hydrodynamic simulation. The upper curves represent a simulation with a QGP phase transition while the lower curves correspond to an ideal gas expansion [1].

out–side ratio does not display a clear signal of QGP formation. The inclusion of a RQMD after–burner increases the emission time and makes comparison between data and theory even less consistent.

While the R_o/R_s ratio as a signature of QGP formation focuses on results from central heavy ion collisions, QGP formation was also predicted in non–central events. An analysis of non–central collisions with a hydrodynamic model by Teaney and Shuryak indicated the presence of a "nutlike" matter distribution with a crescent shaped emission regions at RHIC energies [17]. While oddly shaped emission region are invisible to standard HBT correlation analyses, which average the source shape

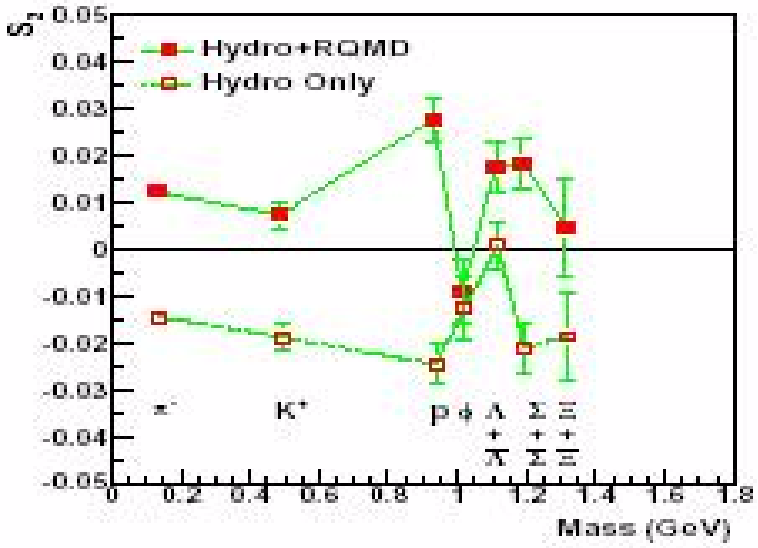

Figure 1.4: The mean spatial anisotropy s_2' as a function of particle mass with and without the RQMD hadronic after–burner [2].

over azimuthal dependencies, the study of the source geometry relative to the emission angle can resolve finer detail in the space time structure of the emission region. Fig. 1.4 shows the spatial anisotropy parameter s_2' for various particle masses. This parameter characterizes the average freeze–out geometry of the emission region and shows a clear change in the source shape when one considers only a hydrodynamic source (open squares) to a hydrodynamic source with a later stage RQMD hadronic after–burner. The pions in particular show a drastic change in the s_2' parameter from a out–of–plane ellipse, $s_2' < 0$, from hydrodynamics to an in–plane extended source with Hydrodynamics+RQMD. A study of the ϕ dependence of the HBT radii provides the information necessary to determine which model scenario better describes the heavy ion collisions at RHIC.

1.2 Organization

The data presented here are taken from the initial heavy ion run from the Relativistic Heavy Ion Collider (RHIC) using Au + Au collisions at $\sqrt{s_{NN}} = 130 AGeV$ as measured with the Solonoidal Tracker At RHIC (STAR) detector. The focus of Chapter 2 will be to present background information and development of HBT interferometry and discuss previous measurements. Chapter 3 presents an overview of the RHIC accelerator complex and the STAR detector in addition to a brief description of the event reconstruction. This thesis will focus on measuring pion correlations through HBT interferometry measurements relative to the event plane to extract the ϕ dependence of the HBT radii. The study of the ϕ dependence of the source radii is a novel analysis technique for corrrelation data that requires additional machinery from the standard azimuthally integrated analysis. Chapter 4 focuses on the development of these tools within the STAR data model. In addition, experimental interferometric issues such as track splitting and track–pair merging and the systematic behaviors they introduce to correlation data are discussed along with procedures developed to correct for them. Chapter 5 will be devoted to presenting the analysis results and to interpret and discuss the implications of the measurements. The measurements will be interpreted in relation to a hydrodynamic parametrization of the emission region and qualitative comparisons to hydrodynamic and molecular dynamic models will be included.

1.3 Author's Contribution

The STAR collaboration is made of up over 400 scientists who, over the past 10 years, have designed, fabricated, and operated the STAR detector to collect and

analyze data from the RHIC collider. The development and testing of analysis and reconstruction software was a primary concern and this is where my conributions were focused. Specific contributions varied from writing software and applying it to analyze changes in performance in event reconstruction codes to serving as a primary developer of the HBT analysis infrastrucutre. The inital HBT analysis software (*StRandyHbtMaker*) was used to perform the first STAR–specific HBT analysis to simulation data. This analysis software gave way to a better design in the modular *StHbtMaker*. One of these modules was written to correct for Coulomb interactions, *StHbtCoulomb*. This software was used to search a table of correction values and is vital to HBT **all** HBT analyses. Reconstruction inefficiencies such as track splitting have a large effect on correlation data. A topological method to characterize the amount of track splitting in STAR and to correct the data was developed and tested in early simulation tests of the analysis software. The success of this topological "cut" lead to its propagation to non–HBT analysis groups such as strangeness. Further, theoretical model HBT studies were carried out in Relativistic Quantum Molecular Dynamics (RQMD), who's results will be compared in this thesis.

CHAPTER 2

OVERVIEW OF MULTIPARTICLE INTERFEROMETRY

In the early 1950's, astronomers were using a technique called interference or Michelson interferometry to measure the angular size of stellar objects. This method took advantage of the phase information of the photons detected and the interference which occurred due to path length differences between the waves to extract size information. At this time interference interferometry was reaching a critical point. The techniques used require phase information to be compared between the two detectors and distortions introduces by atmospheric scattering reduced the effectiveness of the technique. In the late 1950's a pair of scientists, Robert Hanbury–Brown and Richard Twiss, developed the idea of intensity interferometry into a valid alternative to Michelson interferometry [18]. This new method differs from Michelson interferometry in that it uses the quantum correlations to resolve space–time information about the particle source by comparing the two particle coincidence rate P_2 to the product of one particle coincidence rates P_1

$$SIGNAL \rightarrow \frac{P_2(|1\rangle, |2\rangle)}{P_1(|1\rangle)P_1(|2\rangle)}. \tag{2.1}$$

Due to their pioneering work the technique of intensity interferometry is commonly referred to as Hanbury–Brown and Twiss interferometry or HBT.

In the 1960's a similar snenario was introduced by Goldhaber, Goldhaber, Lee, and Pais (GGLP) to explain the angular distributions of π^+ π^+ and π^- π^- pairs emitted from p–$\overline{p}$ annihilations [19]. They found the 2–particle probability was higher for like–sign pion detection at small angle relative to the opposite sign case. While initially this was a puzzle, in this paper, they used symmetrized plane waves to represent the emitted particles to calculate the two particle momentum probability

$$P_2(\vec{p}_1, \vec{p}_2) \approx 1 + \exp\left(-s^2\right), \qquad s = \left|\vec{p}_1 - \vec{p}_2\right| \lambda^{\frac{1}{2}} \tag{2.2}$$

when a Gaussian source was assumed. Here, λ is a measure of the size of the particle source $\lambda = \rho^2/4.63$ and $\vec{p}_i$ is the momentum of particle i. Assuming $\rho = 0.75\hbar/\mu c$ they were able to obtain good agreement between the predicted angular distribution and that which was measured. The successes of Goldhaber lead to the widespread use of HBT to study the spacetime structure of nuclear matter over the past decades. In nuclear or particle physics, then, one often refers to the GGLP effect. At the same time, technological developments lead to Michelson interferometry continuing to play a strong role in astronomy.

The importance of interferometry measurements can be seen in the wealth of information it can provide about the particle emitting source. In this chapter, I will describe how, in addition to being an effective method to obtain 3–dimensional source geometries, interferometry also provides information about the evolution timescale, the emission duration of the source, and source dynamics such as collective flow. With the increased energies available at present and future colliders (RHIC and LHC) the particle multiplicities will be such that interferometry analyses will be done using a variety of particles including some neutral particles such as Λ and K^0 which will provide information about strangeness production in heavy on collisions [20].

2.1 Basic Interferometry

In the most basic example of intensity interferometry, one considers the case of a pair of free–streaming particles emitted from two points $R_{1,2}$, at positions $\vec{r}_1$ and $\vec{r}_2$, within some generalized source and then observed by a pair of detectors $D_{1,2}$, at positions $\vec{r}'_1$ and $\vec{r}'_2$, with momenta $\vec{p}_1$ and $\vec{p}_2$, as seen in Fig. 2.1. Planar wave functions are used to represent the emitted particles and must be symmetrized (antisymmetrized) according to the bose (fermi) statistics present

$$\Psi = u(\vec{r}_1,\vec{p}_1)\ u(\vec{r}_2,\vec{p}_2)\ e^{i\vec{p}_1\cdot(\vec{r}'_1-\vec{r}_1)}e^{i\vec{p}_2\cdot(\vec{r}'_2-\vec{r}_2)} \pm u(\vec{r}_2,\vec{p}_1)\ u(\vec{r}_1,\vec{p}_2)\ e^{i\vec{p}_1\cdot(\vec{r}'_1-\vec{r}_2)}e^{i\vec{p}_2\cdot(\vec{r}'_2-\vec{r}_1)}. \tag{2.3}$$

Here, $u(\vec{r}_i,\vec{p}_j)$ is the source function for emitting a particle of momentum $\vec{p}_j$ from point $\vec{r}_i$. Assuming the emission function has a smooth momentum dependence, the smoothness approximation, the source functions become functions of the emission position, $\vec{r}$, and the total pair momentum, $\vec{K} = (\vec{p}_1+\vec{p}_2)/2$ [21]

$$u(\vec{x},\vec{p}_1)u(\vec{y},\vec{p}_2) = u(\vec{x},\vec{K}+\frac{1}{2}\vec{q})u(\vec{y},\vec{K}-\frac{1}{2}\vec{q}) = u(\vec{x},\vec{K})u(\vec{y},\vec{K}), \tag{2.4}$$

where $\vec{q} = \vec{p}_1 - \vec{p}_2$ is the relative momentum. This gives a two–particle probability

$$\left|\Psi\right|^2 = |u(\vec{r}_1,\vec{K})|^2|u(\vec{r}_2,\vec{K})|^2\ (1\pm\cos(\vec{q}\cdot\Delta\vec{r})), \tag{2.5}$$

where $\Delta\vec{r}$ is the vector between emission points. Normalizing (2.5) by the single particle probabilities, $|u(\vec{r},\vec{K})|^2$, gives the 2–particle correlation function

$$C_2(\vec{p}_1,\vec{p}_2) = 1\pm\cos(\vec{q}\cdot\vec{r}). \tag{2.6}$$

In equations (2.3,2.5, and 2.6), the $+(-)$ correspond to the case of Boson (Fermion) correlations. From (2.6), we see a relation betwen the measured momentum difference

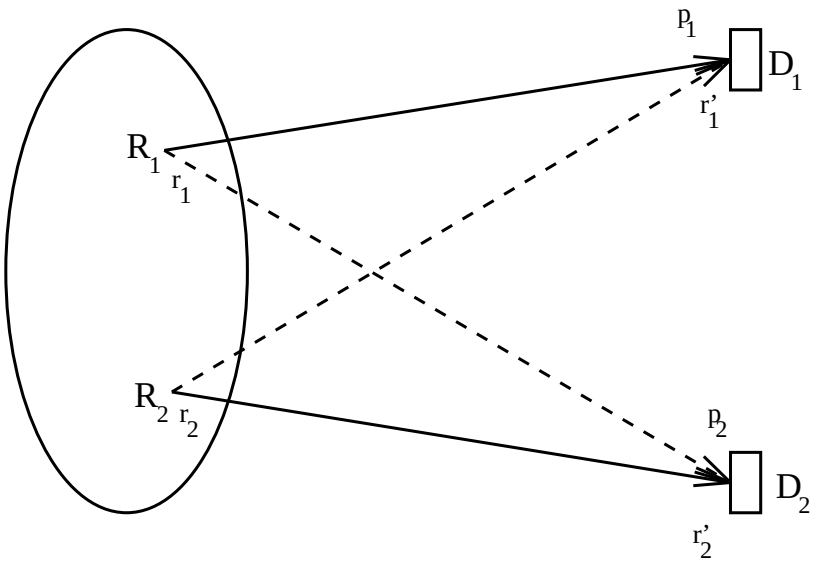

Figure 2.1: Symmetrization of the pion wavefunctions.

$\vec{q}$ and the spatial separation of the emission points of the two particles $\vec{r}$. The above example considers only the symmetrization of a pair of particles.

2.1.1 Continuous Emission Region

Realistically one must consider a more complicated collection of emitted particles. The quantum state $|\phi_f\rangle$ describing the particles emitted from the particle source can be written [22] as

$$|\phi_f\rangle = e^{-\bar{n}/2} \exp\left(i \int d^3k \; J(\vec{p}) a^\dagger(\vec{p}) \right) |0\rangle, \tag{2.7}$$

where $J(\vec{p})$ is the Fourier transform of the current operator from the pion Klein–Gordon equation, $(\Box + m_\pi^2)\phi(x) = J(x)$, and $a^\dagger$ is the creation operator. The state

$|\phi_f\rangle$ has the property that it is an eigenstate of the annihilation operator[23]

$$a_p|\phi_f\rangle \;=\; i\int d^4x\;\frac{e^{ip\cdot x}}{\sqrt{2E_p(2\pi)^3}}\;J(x)\;|\phi_f\rangle. \tag{2.8}$$

Using the creation and annihilation operators, the single particle production probability for state $|\phi_f\rangle$ can be expressed as

$$P_1(p) = E_p\frac{dN}{d^3p} \;=\; E_p\langle\phi_f|a_p^\dagger a_p|\phi_f\rangle \tag{2.9}$$

and the pair production probability is given by

$$P_2(p,q) = E_pE_q\frac{dN}{d^3p\;d^3q} \;=\; E_pE_q\langle\phi_f|a_p^\dagger a_q^\dagger a_q a_p|\phi_f\rangle. \tag{2.10}$$

There are two limits to consider for the emission of particle pairs from the source, coherent or chaotic emission. The planar wave functions used to desribe the emitted particles each have a creation phase associated with them. If these phases are identical, the particles are described as coherent. If these phase are uncorrelated, the source is termed chaotic. In the case of a coherent source, (2.10) simplifies to

$$P(p,q) \;=\; E_pE_q\langle\phi_f|a_p^\dagger a_p|\phi_f\rangle\;\langle\phi_f|a_q^\dagger a_q|\phi_f\rangle, \tag{2.11}$$

resulting in a constant correlation function $C(\vec{p}_1,\vec{p}_2) = 1$. In this case there is no correlation between the emitted particles. If one assumes chaotic particle emission, the expectation in (2.10) can be expanded through the use of the Wick theorem [24] to

$$\langle\phi_f|a_p^\dagger a_q^\dagger a_q a_p|\phi_f\rangle = \langle\phi_f|a_p^\dagger a_p|\phi_f\rangle\langle\phi_f|a_q^\dagger a_q|\phi_f\rangle + \langle\phi_f|a_p^\dagger a_q|\phi_f\rangle\langle\phi_f|a_q^\dagger a_p|\phi_f\rangle. \tag{2.12}$$

This can be interpreted as the sum of probabilities of particles being emitted from two points within the source with the interchange probabilities. Using (2.8) and (2.12),

the pair production probability can be expressed as[23]

$$\begin{aligned}\langle\phi_f|a_p^\dagger a_q^\dagger a_q a_p|\phi_f\rangle &= \int d^4r\ d^4r'\ S(r,p)S(r',q) \\ &\quad \pm \int d^4r\ d^4r'\ S(r,\frac{p+q}{2})S(r',\frac{p+q}{2})e^{ip\cdot r}e^{-iq\cdot r'} \\ &= \int d^4r\ d^4r'\ S(r,p)S(r',q) \\ &\quad \pm \Big|\int d^4r\ S(r,\frac{p+q}{2})e^{i(p-q)\cdot r}\Big|^2 \end{aligned} \tag{2.13}$$

Here, $S(r,p)$ is the phase space density function and represents the probability of producing a particle with momentum p at a space–time point r. Using this, the correlation function can be expressed as[23]

$$C(\vec{p}_1,\vec{p}_2) \ = \ 1 \pm \frac{\Big|\int d^4r\ S(r,\vec{K})e^{iq\cdot r}\Big|^2}{\int d^4r\ S(r,\vec{p}_1)\ \int d^4r'\ S(r',\vec{p}_2)}, \tag{2.14}$$

a function of the total pair momentum, $\vec{K} = (\vec{p}_1 + \vec{p}_2)/2$, and the pair relative momentum, $q = (p_1 - p_2)$. The numerator is seen to be the Fourier transform of $S(q,\vec{K})$, the source function of particles with relative momentum q.

The dependence of the correlation function on the total pair momentum introduces a relationship between the dynamics of the particle source (i.e. space–momentum correlations) and the measured size. A study of the $\vec{K}$ dependence of the HBT source parameters can be used to obtain information about the dynamics of the emission region. It should be noted that the source parameters returned from an HBT analysis do not provide the actual source dimensions, but provide information regarding the size of the *source producing particle pairs within a portion of momentum phase space*. The expression in italics is often called a "region of homogeneity" [25].

2.1.2 Lengths of Homogeneity

By using a saddle point method, the phase space density function was shown to be approximated by[26]

$$S(x,K) \;\simeq\; S(\bar{x},K)\;\exp\,[-\frac{1}{2}(x-\bar{x})^{\mu}(x-\bar{x})^{\nu}\;B_{\mu\nu}(K)]. \tag{2.15}$$

where $\bar{x}_{\mu} = \langle x_{\mu} \rangle$ is the saddle point, equal to the average emission point of particle pairs with total momentum K. The saddle point approximation provides a relation between the symmetric curvature tensor, $B_{\mu\nu}$, and the expectation values of x_{μ}

$$(B^{-1})_{\mu\nu} \;=\; \langle x_{\mu}x_{\nu}\rangle - \langle x_{\mu}\rangle\langle x_{\nu}\rangle \;=\; \langle \tilde{x}_{\mu}\tilde{x}_{nu}\rangle. \tag{2.16}$$

The diagonal terms $(B^{-1})_{\mu\mu}$ of the curvature tensor are seen to be "lengths of homogeneity" and provide a measure of the size of the source of particle pairs with momentum K. Inserting (2.15) to (2.14) one can calculate the expression for the correlation function from a Gaussian particle source,[26]

$$C(\vec{q},\vec{K}) \;=\; 1 \pm \exp\,[-q^{\mu}q^{\nu}R^{2}_{\mu\nu}]. \tag{2.17}$$

Here, $R^{2}_{\mu\nu}$ has replaced the curvature tensor and are referred to as the source radii. These radii are not measures of the geometric size of the whole source; they represent the size of regions in which particles similar in momentum phase space are emitted. While the diagonal terms measure these regions of homogeneity, the off–diagonal terms indicate the presence of tilts, or momentum correlations, in the correlation function. These terms can have both positive and negative signs distiguishing negative and positive tilts [27]. Equation (2.17) is the chaotic expectation from a Gaussian phase space density function. In general, the emission of particles is neither perfectly chaotic nor truly coherent. In addition, correlation functions are effected by pions

emanating from strong decays (i.e. σ, ρ, and ω) and misidentified particles. The presence of pions originating from particle decays introduce a shadow source with a size determined by the lifetime of the parent particle. Pions entering the analysis from misidentified particles such as a kaon introduce totally uncorrelated pairs. These 3 effects reduce the intercept point $C(0)$ of the correlation function. A λ parameter is then included within the correlation function to account for this

$$C(q, K) \;=\; 1 \pm \lambda \exp\left[-q^{\mu} q^{\nu} R^{2}_{\mu\nu}\right]. \tag{2.18}$$

This also represents the functional form of the correlation function used to fit to experimental data.

2.1.3 Final State Interactions

In the above development of interferometry it was assumed that the outgoing particles are free–streaming and can be described by non–interacting plane waves. This is not the case for the emitted particles which are affected by a series of interactions including Coulomb effects from both the remnant source and other emitted particles as well as the strong nuclear force.

Strong Interaction

The strong nuclear force is an interaction between quarks whose residual effects are responsible for binding nucleons (neutrons and protons) in the nuclei of atoms where it overwhelms the electromagnetic interactions. All hadrons experience strong interactions on a small distance scale. The estimated range of interaction for the strong nuclear force between pions is about 0.2 fm [28]. The typical size of the emission region in Au + Au collisions in several fermi and so the typical separation

between emission points for pion pairs is much larger then the relevant scale for the strong interaction. For this reason effects due to the strong interaction will be ingored in this analysis.

Coulomb Interaction

All charged particles interact electromagnetically via the Coulomb force which is attractive for opposite signed charges while repulsive for like signed particles. There are two Coulomb forces present for the emitted particles. The emitted particles interact with each other as they emerge from the emission region. In addition, the positively charged remnant particle source introduces Coulomb interactions between the emitted particles and the source itself.

To account for the interaction between emitted particles, one factorizes the particle pair wavefunction into a center of mass term and a relative part:[29]

$$\Psi_{12}(\vec{p}_1, \vec{x}_1, \vec{p}_2, \vec{x}_2) = \exp\left[i(\vec{p}_1 + \vec{p}_2) \cdot (\vec{x}_1 + \vec{x}_2)/2\right] \times \phi_r(\vec{p}_1 - \vec{p}_2, \vec{x}_1 - \vec{x}_2). \tag{2.19}$$

The wave equation of scattering solutions for a pure Coulomb potential are given by[29, 30]

$$\phi_c(\vec{k}, \vec{r}) = e^{\frac{\pi\gamma}{2}} \Gamma(1 + i\gamma) e^{ikz} F[-i\gamma; 1; i(kr - i\vec{k} \cdot \vec{r})] \tag{2.20}$$

with symmetrized solution given by

$$\phi_r(\vec{k}, \vec{r}) = \frac{1}{2}(\phi_c(\vec{k}, \vec{r}) + \phi_c(\vec{k}, -\vec{r})). \tag{2.21}$$

Here,

$$\begin{aligned} \vec{v} &= \text{relative velocity} \\ \vec{k} &= \frac{m}{\hbar}\vec{v} \\ \gamma &= \frac{ZZ'e^2}{\hbar|\vec{v}|}. \end{aligned} \tag{2.22}$$

Combining equations (2.19) and (2.21) and integrating into the pair production probability (2.10) one obtains the Coulomb corrected two particle probability distribution. This is then integrated to obtain the correction factor for the Coulomb interaction between emitted particles. Experimental considerations about the Coulomb correction will be discussed in Chapter 4.

In addition to the attraction(repulsion) felt by the emitted particles from interactions with each other there is a potentially large Coulomb potential from the positively charged source. The effects on the pion correlation function was found to be very small and decreases as the collisions energy becomes ultrarelativistic [31, 32]. One would intuitively recognize that the central potential would have a similar effect on the entire momentum spectrum thereby reducing any changes that would be measured in the relative momentum distributions. In addition the relativistic speeds at which pions are emitted from the source greatly reduces the amount of time for the central Coulomb potential to effect the momentum distribution. We do not apply any correction to the data due to the central Coulomb potential, in accordance with standard practice.

2.1.4 Coordinate Parameterizations

Up to now the interferometry discussion has been presented in the full 6-dimensional phase–space defined by the components of the momenta of the two particle distributions. To extract information from the experimentally determined correlation fuction one must choose a coordinate system in which to work. The coordinate system used generally depends on the geometry of the detector used as well as the amount of

statistics available for the analysis. In addition one must consider the frame of reference used in previous measurements to allow comparisons and extend systematic studies.

$\mathbf{q_{inv}}$ Parametrization

The standard parametrization for the correlation function is of a Gaussian form. A simple form of the correlation function is called the q–invariant, $q_{inv} = \sqrt{\mathbf{q}^2 - q_o^2}$, parametrization which compresses all of the spatial and temporal information into a single Gaussian parameter, R_{inv}. In this case the correlation function is given by

$$C(\vec{q}, \vec{K}) = 1 + \lambda(\vec{K}) \exp\left[-q_{inv}^2 R_{inv}^2(\vec{K})\right]. \tag{2.23}$$

This 1–dimensional parametrization is valuable from the experimental standpoint in that it allows the use of lower statistics data than other multi–dimensional analyses. This allows the experimentalist to perform interferometry analyses in experiments at lower energies where the particle multiplicty drops or where the detector acceptance reduces the number of measured particles. In addition the q–invariant parametrization allows one to perform HBT analyses to additional event classes such as "rare" events found at higher energies. Fig. 2.2(a) shows the result of a q_{inv} analysis of the $130 AGeV$ STAR data [3]. While such a simple parametrization of the correlation function brings flexibility to the experimentalist, the process of combining the spaital–temporal information into a single parameter makes the interpretation of the result more difficult; the radius extracted through a q–invariant analysis does not represent a physical extension of the system. By expanding the number of dimensions one can study not only the geometric size but also properties of the evolution of the paricle emitting source.

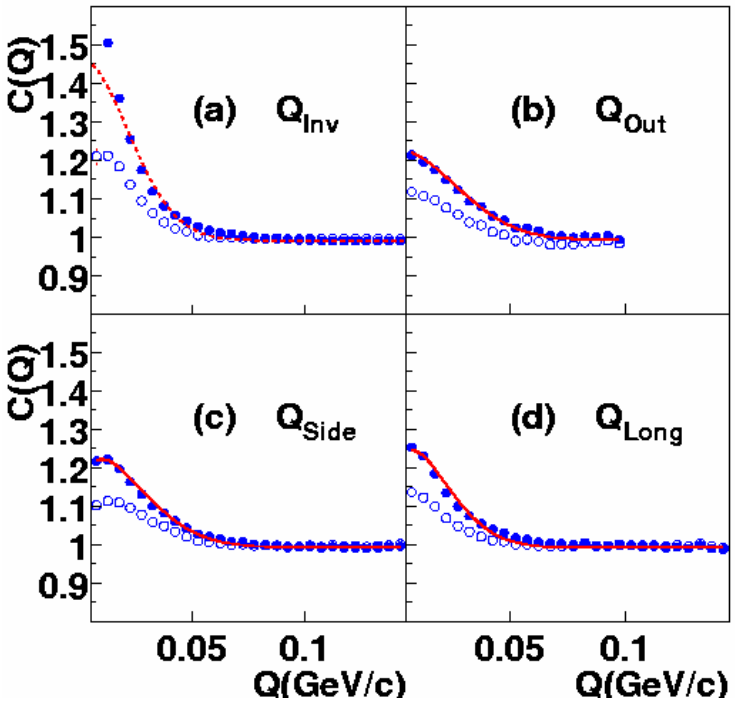

Figure 2.2: 1D (q_{inv}) histogram and 1D projections of Pratt–Bertsch parameterization correlation functions for $\sqrt{s_{NN}} = 130GeV$ Au + Au collisions. Shown are histograms for both uncorrected (open circles) and Coulomb corrected (closed circles) with Gaussian source fits to the corrected data (lines) [3].

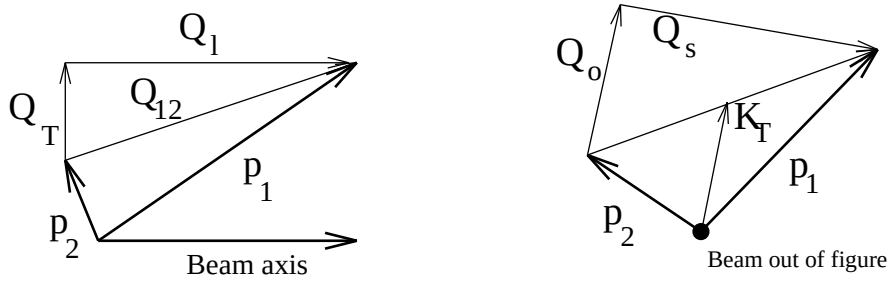

Figure 2.3: Pratt-Bertsch decomposition of the momenta to a longitudinal q_l and transverse q_T components (left figure) and the decomposition to outward q_o and sideward q_s (right figure).

Pratt–Bertsch Parametrization

With increasing statistics, a 3–dimensional analysis allows the extraction of additional information about the source geometry and dynamics of the emission region. A commonly used parameterization is the Pratt–Bertsch or Cartesian parameterization [29, 33]. This reference frame is spanned by three vectors referred to as the outward, sideward, and longitudinal axes. These axes are determined by the beam direction and the pair transverse momentum, $\vec{K}_T = (\vec{p}_1 + \vec{p}_2)_T/2$. The longitudinal or long axis is taken to be parallel to the beam direction, while the outward and sideward axes are components of the pair transverse momentum. The outward or "out" axis is defined to be parallel to the transverse momentum while the sideward axis is perpendicular to both the long and out axes, $q = (q_o, q_s, q_l)$. The Pratt–Bertsch axes are shown in Fig. 2.3 for an example pair.

Expressing (2.18) in terms of the Bertsch–Pratt momenta gives

$$C(\vec{q},\vec{K}) = 1 \pm \lambda \exp\,(\sum_{i,j=o,s,l} -q_i q_j R_{i,j}^2). \tag{2.24}$$

By using the mass–shell constraint,

$$q^0 = \vec{\beta}\cdot\vec{q}, \qquad \vec{\beta} = \vec{K}/K \tag{2.25}$$

where $\vec{\beta} = (\beta_T, 0, \beta_l)$ is the pair velocity, the explicit time dependence of the correlation function drops out. An implicit time dependence remains in the outward and longitudinal components of the HBT radii

$$R_o^2 = \langle(\tilde{x_o} - \beta_T\tilde{t})^2\rangle, \tag{2.26}$$

$$R_l^2 = \langle(\tilde{x_l} - \beta_l\tilde{t})^2\rangle, \text{ and} \tag{2.27}$$

$$R_s^2 = \langle\tilde{x_s}^2\rangle. \tag{2.28}$$

Additional terms (R_{os}^2, R_{ol}^2, and R_{sl}^2) are also present in the full expansion of (2.24). If cylindrical source symmetry is assumed, the out–side and side–long components cancel due to symmetry and at midrapidity, the out–long component also vanishes. In standard practice, the form of the correlation function which is fit to data is

$$C(\vec{q},\vec{k}) = 1 \pm \lambda e^{-q_o^2R_o^2 - q_s^2R_s^2 - q_l^2R_l^2}. \tag{2.29}$$

Fig. 2.2(b,c,d) show the projections of the correlation function of an azimuthally integrated Pratt–Bertsch analysis of the $130AGeV$ STAR data [3]. The effects of the Coulomb suppression at low–q can be seen by comparing the raw data (open diamonds) to the Coulomb corrected result (closed stars). Projections of a fit to (2.29) is also included.

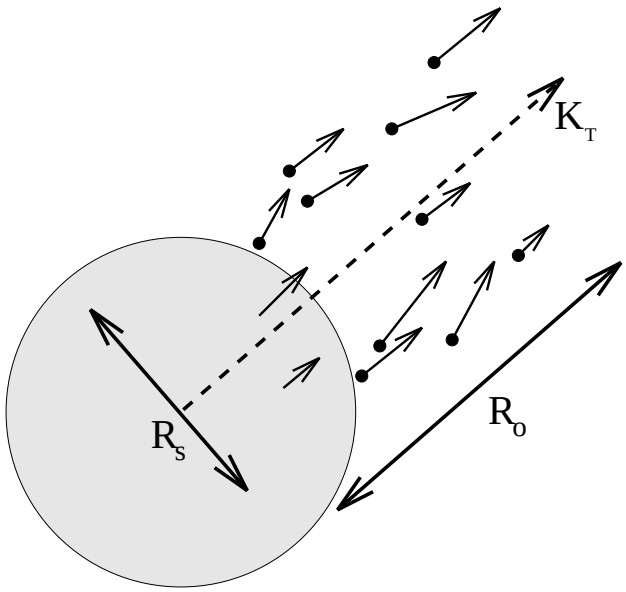

Figure 2.4: Diagram of the Pratt-Bertsch axes showing how R_o^2 is effected by emission duration.

Equations (2.26–2.28) show the dependence of the lengths of homogeneity on the particle emission time–scale also seen in Fig. 2.4. In particular, the absence of time dependence in the sideward radius when compared to the outward radius allows an estimation of the emission time-scale when all correlations (space–time, space–momentum) are ignored. It is expected that with a phase transition to a QGP, the emission time–scale will increase providing a signal in 3–dimensional Pratt–Bersch analyses. Fig. 2.5 shows a compendium of HBT radii measured in various experiments for a series of colliding energies. In Fig. 1.3, a signal for a phase transition was expected to be visible in the comparison of the outward and sideward radii. While not definitive, Fig. 2.5 suggests that this energy range provides no evidence for the

presence of a phase transition. The large collision energy gap present between the SPS ($\sim 20GeV$) and RHIC ($\sim 200GeV$) will be filled in by future runs of RHIC.

2.2 Experimental HBT Procedure

The experimental correlation function is formed through the creation of two histograms, referred to as the numerator and denominator. The numerator is formed from particle pairs in the same event and represents the distribution of the two–particle probabilities for a quantity. In the case of HBT interferometry, the distribution is the relative momentum. These pairs are typically called "real" pairs. The denominator is formed by mixing particles in separate events. In this way, there are no physical interactions between the pairs which are simply called "mixed" pairs and represent the single particle probabilities. The denominator for each event is formed by mixing each particle in that event with all of the particles in a collection of events called a "mixing buffer" which typically consists of ~ 5 events. It is implied that the particles which are used to form these histograms have passed some criteria to select for only pions. The correlation function is then the ratio of the numerator histogram divided by the denominator

$$C(\vec{q}) = \frac{N(\vec{q})}{D(\vec{q})}. \tag{2.30}$$

This experimental correlation function is then used to fit to Eq. (2.17).

2.3 Azimuthally sensitive particle interferomery

Noncentral collisions are characterized by an almond shaped (ellipsoidal) geometry built from the overlap sections of the participant nuclei which then evolves to some average freeze–out geometry. This freeze–out geometry is what is measured through

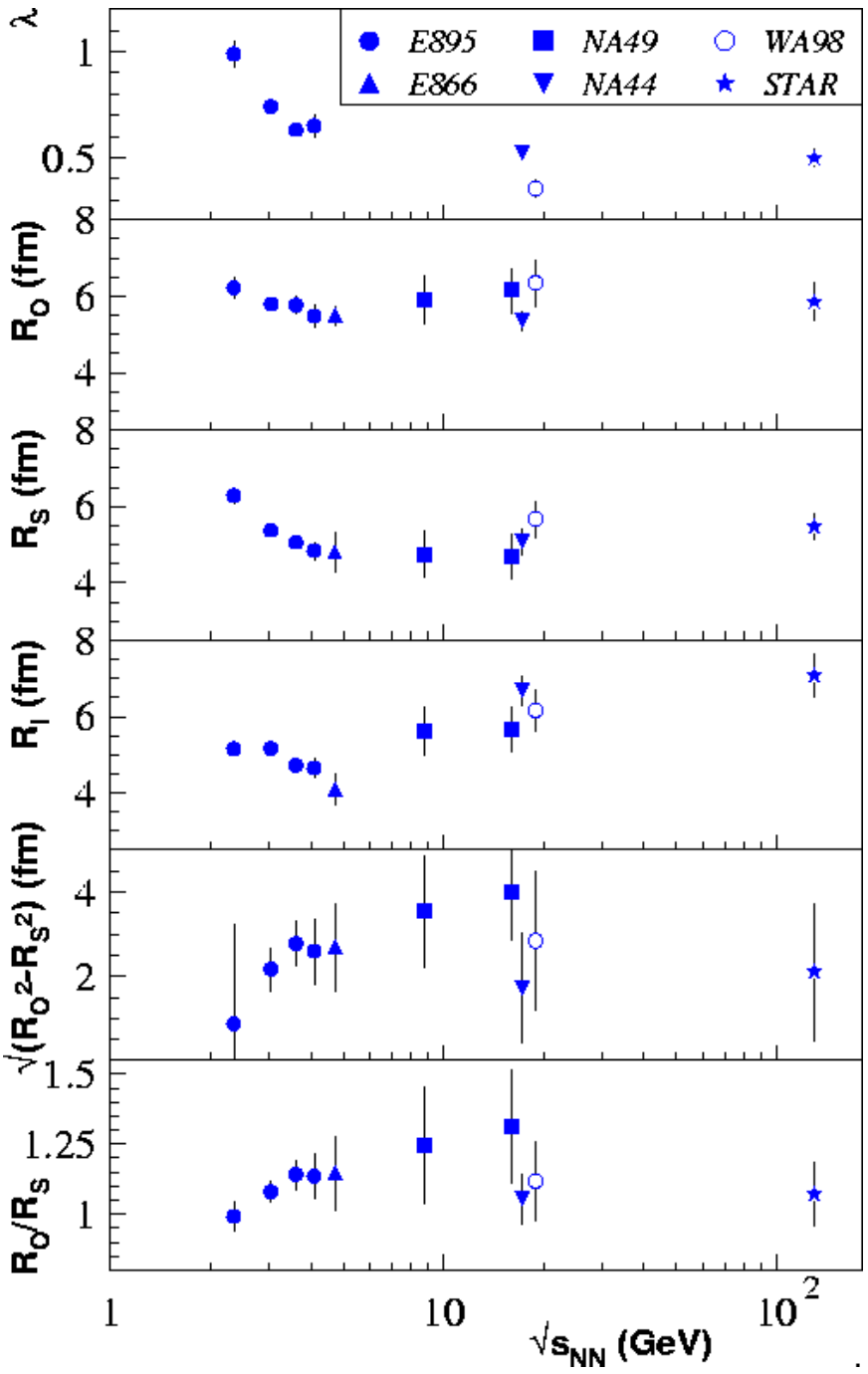

Figure 2.5: The energy dependence of midrapidity π^- HBT radii from central Au + Au or Pb + Pb collisions at $p_T \sim 0.17 GeV/c$ [4, 5, 6, 7].

interferometric studies. The study of particle interferometry relative to the event plane allows one to resolve changes in the shape of the source as one observes from different angles. Thus, it will measure the change in the transverse source shape and can discriminate between a source which has retained its initial configuration (extended out–of–plane) to one which has evolved to cylindrical or even one extended in–plane. The study of interferometry relative to the event plane thus studies the freeze–out configuration of such an input geometry and provides information about the source evolution. Fig. 2.6 shows the overlap region created in a noncentral collision in addition to indicating the direction of the impact parameter, $\vec{b}$. The input geometry can be characterized by an in–plane extension which is substantially smaller than the out–of–plane extension. If the system retains any anisotropy upon freeze–out, the assumption of a cylindrical emission region would be an oversimplication. This assumption is at the heart of azimuthally integrated analyses, which is almost all of what has been studied so far.

2.3.1 Analyzing non–central collisions

Noncentral collisions are inherently both spatially and dynamically anisotropic. The standard HBT analysis which integrates the collision data over event plane angles does not take into account the changes in the source characteristics as one observes the source from various angles relative to the event plane. To take into account the changes in the relative source geometry as one measures from different angles the source extensions or homogeneity lengths must be rotated[21]

$$R_{ij}^2 = \langle [(\mathbf{F}_\phi \tilde{x})_i - (\mathbf{F}_\phi \beta)_i \tilde{t}][(\mathbf{F}_\phi \tilde{x})_j - (\mathbf{F}_\phi \beta)_j \tilde{t}] \rangle. \tag{2.31}$$

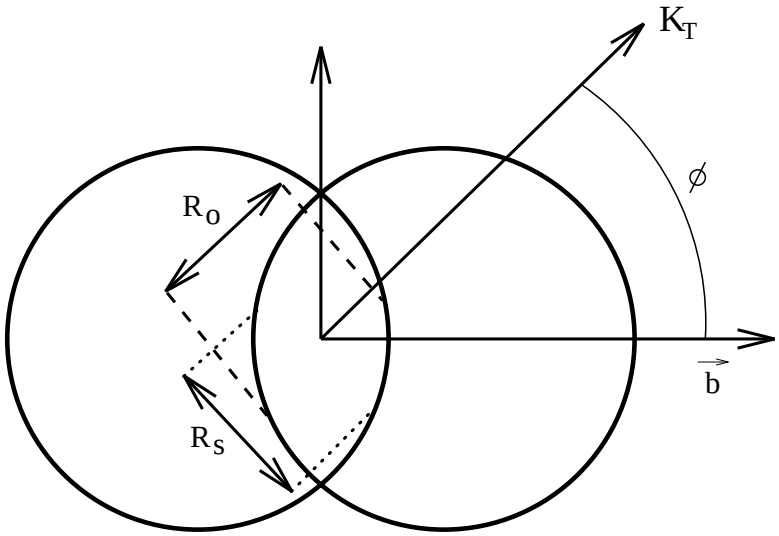

Figure 2.6: Decomposition of the ϕ dependent transverse Bertsch–Pratt axes for an example K_T. The outward radius R_o is parallel to the pair transverse momentum and the sideward radius R_s is perpendicular.

Here, F_ϕ is a rotation matrix, with ϕ indicating the angle between the impact parameter and the angle of emission of the particle pair, and $F_\phi\beta = (\beta_T, 0, \beta_l)$. The homogeneity lengths are given in the source fixed frame so that $\tilde{x}$ represents the source extension along $\vec{b}$. This provides a relation between the HBT radii, R_{ij}, and the source extensions in the source fixed frame,[34]

$$\begin{aligned}
R_o^2(K_T,\phi,y) &= S_{11}\sin^2(\phi) + S_{22}\cos^2(\phi) + S_{12}\sin(2\phi) - \\
&\quad - 2\beta_T S_{01}\cos(\phi) - 2\beta_T S_{02}\sin(\phi) + \beta_T^2 S_{00}, \\
R_s^2(K_T,\phi,y) &= S_{11}\sin^2(\phi) + S_{22}\cos^2(\phi) - S_{12}\sin(2\phi), \\
R_l^2(K_T,\phi,y) &= S_{33} - 2\beta_l S_{03} + \beta_l^2 S_{00}, \\
R_{os}^2(K_T,\phi,y) &= S_{12}\cos^2(2\phi) + \frac{1}{2}(S_{22} - S_{11})\sin(2\phi) + \\
&\quad + \beta_T S_{01}\sin(\phi) - \beta_T S_{02}\cos(\phi), \\
R_{ol}^2(K_T,\phi,y) &= (S_{13} - \beta_l S_{01})\cos(\phi) - \beta_T S_{03} + \\
&\quad + (S_{23} - \beta_l S_{02})\sin(\phi) + \beta_l\beta_T S_{00}, \\
R_{sl}^2(K_T,\phi,y) &= (S_{23} - \beta_l S_{02})\cos(\phi) - (S_{13} - \beta_l S_{01})\sin(\phi).
\end{aligned} \tag{2.32}$$

Here, $S_{\mu\nu}$ is called the spatial correlation tensor and represents the source extensions in the impact–parameter fixed frame

$$S_{\mu\nu} = \begin{pmatrix} \tilde{t}^2 & \tilde{t}\tilde{x} & \tilde{t}\tilde{y} & \tilde{t}\tilde{z} \\ \tilde{x}\tilde{t} & \tilde{x}^2 & \tilde{x}\tilde{y} & \tilde{x}\tilde{z} \\ \tilde{y}\tilde{t} & \tilde{y}\tilde{x} & \tilde{y}^2 & \tilde{y}\tilde{z} \\ \tilde{z}\tilde{t} & \tilde{z}\tilde{x} & \tilde{z}\tilde{y} & \tilde{z}^2 \end{pmatrix}. \tag{2.33}$$

In addition to the explicit ϕ dependence introduced through the rotation matrix, the S_{ij} components also contain emission angle dependence from contributions from collective motion, radial and elliptic flow, present in the source.

The measured oscillations with respect to ϕ are also affected by the opacity of the source. Heiselberg and Levy determined the dependence of the transverse radii for

both a transparent and opaque source[35]

$$R_s^2 = g_s R^2[1 + \delta\cos(2\phi)] \tag{2.34}$$

$$R_o^2 = g_o R^2[1 - \delta\cos(2\phi)] + \beta^2\delta\tau^2 \tag{2.35}$$

$$R_{os}^2 = g_{os} R^2\delta\sin(2\phi)] \tag{2.36}$$

Here, $R^2 = (R_x^2 + R_y^2)/2$ is the average radius of the source, $\delta = b/2R_a$ measures the overlap region, and $g_{o,s,os}$ are model dependent factors characterizing the opacity of the source. $g_{o,s,os} = 1$ when the source is transparent and decrease with increasing opacity. In all cases $g_{os} \simeq g_s$ and $g_o < g_s$. The magnitude of the oscillations become equal only in the case of a fully transparent source.

Transverse flow also modifies the transverse HBT radii. In [35, 36], a transverse flow gradient was included in calculations that showed a decrease in the measured radii by a factor $\sim (1 + u_o^2 m_T/T)$, where u_o is a flow scaling factor. A similar effect is seen in various dynamical models.

The development of studying the transverse source shape using ϕ dependent HBT interferometry has been paralleled by a simlar development is astronomy. Recently interferometric measurements were used to measure the degree of oblateness for the $A7IV - V$ star Altair [37].

2.3.2 Determination of the event plane

The angle ϕ in the previous equations is defined relative to the impact parameter or the event plane. The impact parameter is used to describe the distance between the centers of the particles in a collision. A noncentral collision is characterized by nonzero values of the impact parameter. In such collisions, the geometry of the overlap

region of the two colliding nuclei is non-cylindrical. The pressure gradients are thus different from the in–plane and out–of–plane axes. The difference in the pressure gradients (and surface geometry) cause a greater flow of particles and energy to be emitted along the impact parameter, "in" the event plane. This "number" or energy flow anisotropy is then used in the calculation of the event plane.

The calculation of the event plane in heavy ion collisions is done through an analysis of the distribution of freeze–out momenta, the momenta when particles are free–streaming from the emission region. At lower energies, the flow angle is sufficiently large that a determination of the event plane can be made through the formation of the full sphericity tensor[38]

$$S_{ij} = \sum_{\nu=1}^{M} w(\nu) p_i(\nu) p_j(\nu). \tag{2.37}$$

Here, $p_i(\nu)$ is the i^{th} component of the ν^{th} particle and $w(\nu)$ is a weighting associated with that particle. This particle weighting is typically taken such that the sphericity tensor is a measure of the total kinetic energy from the outgoing particles. The matrix has three eigenvalues, f_i, with three eigenvectors, $\hat{e}_i$. The symmetry associated with collisions of equal mass nuclei, as is the case with $Au + Au$ collsions, requires one eigenvector to point out of the event plane, perpendicular to both impact parameter and beam directions. This eigenvector then allows one to determine the event plane.

At higher collision energies, the amount of longitudinal momentum present reduces the flow angle and the relative magnitude of the transverse eigenvalues from the sphericity tensor [39]. Ollitrault shows that a transverse sphericity tensor, continues to allow the calculation of the event plane [40]. This method was used to determine the event plane for azimuthally sensitive analyses in E895 to extract flow values as well as HBT parameters [41, 42, 8].

A generalized formalism for determining the n^{th} order event plane was proposed by Poskanzer and Voloshin [39]. This method couples the calculation of the event plane with the flow coefficients. These coefficients represent a Fourier expansion of the momentum distribution:

$$E\frac{dN^3}{d^3p} = \frac{1}{2\pi}\frac{d^2N}{p_t dp_t dy}\left(1 + \sum_{n=1}^{\infty} 2v_n \cos[n(\phi - \Psi_r)]\right). \tag{2.38}$$

The reaction plane is then determined through a set of equations[39]

$$Q_n \cos(n\Psi_n) = \sum_i w_i \cos(n\phi_i), \tag{2.39}$$

$$Q_n \sin(n\Psi_n) = \sum_i w_i \sin(n\phi_i), \text{ and} \tag{2.40}$$

$$\Psi_n = \tan^{-1}\left(\frac{\sum_i w_i \sin(n\phi_i)}{\sum_i w_i \cos(n\phi_i)}\right)/n. \tag{2.41}$$

One may then calculate the flow vector Q_n and the event plane angle Ψ_n of order n. One can show the equivalence of this method for $n = 2$ and the sphericity tensor [39]. Experimental issues such as acceptance corrections and event plane resolution will be discussed in Chapter 4.

2.3.3 Previous measurements

While essentially all HBT analyses have implicitly assumed azimuthally symmetric emission regions (valid in principle only for $b = 0$ collisions, which occur with vanishing probability), interferometry relative to the event plane has been studied previously at the AGS by experiments E877 and E895 [43, 8]. While the E877 mesaurement presented a general source size in–plane versus out–of–plane, the E895 measurement increased the number of fit parameters by using the full experimental correlation function including cross–terms in the radii. E895 not only measured the eccentricity

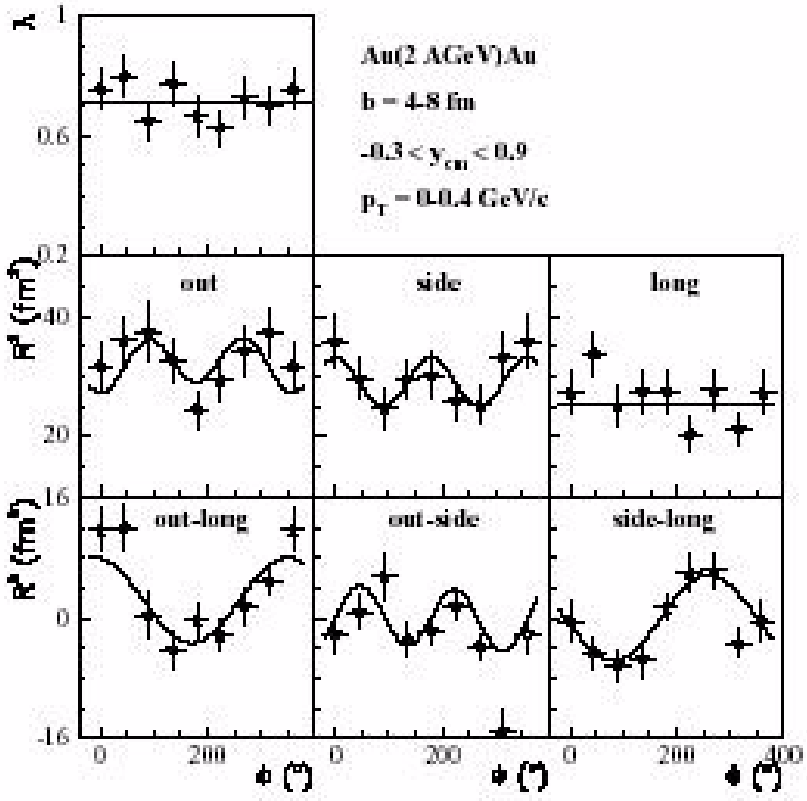

Figure 2.7: Pion interferometry results of ϕ dependent HBT radii for AGS experiment E895 using Au + Au beam–target collisions at $2AGeV$ [8].

of the transverse source, but also made the first measurements of spatial tilts in the emission region. The Φ dependence of the HBT radii are shown in Fig. 2.7 where (2.32) was used to fit the ϕ dependence of the radii which are seen to describe the overlap region of the two colliding nuclei [8].

The dynamics of the source measured at these lower energies $2 - 8AGeV$ were very different from those we find at RHIC [41, 44]. The elliptic flow was much smaller and a transition from out–of–plane squeeze–out to in–plane flow was determined at

these energies [41]. While radial flow is present at the AGS, it was ignored in the E895 azimuthally sensitive analysis due to the low p_T cut used in the analysis and to remove complexities introduces from additional dynamical contributions to the source radii. Hence while at the AGS the source dynamics were seen to be dominated by the thermal contribution, $Au + Au$ collisions at RHIC indicate a strong flow which has a large affect on the momentum distributions. The presence of flow introduces strong implicit ϕ dependencies to the spatial correlation tensor elements. The dynamics observed at the AGS allowed those dependencies to be neglected and so the source dimensions obtained in E895 from (2.32) was reflective of the actual source geometry. The emission region found was extended out–of–plane and was found to be consistent with the overlap region of the two colliding nuclei, suggesting little shape evolution of the system before freeze–out.

CHAPTER 3

THE STAR EXPERIMENT

The STAR experiment is one of four commissioned to study the physics of the Relativistic Hevy Ion Collider (RHIC), shown in Fig. 3.1. RHIC has a top collision energy for heavy nuclei of $\sqrt{s_{NN}} \sim 200GeV$. For the first year of data–taking, the collider accelerated gold (Au) nuclei to an energy of $65AGeV$. For comparison, earlier heavy ion studies have been done using fixed target experiments at the Alternating Gradient Synchrotron (AGS), which accelerated Au nuclei at various energies up to $\sqrt{s_{NN}} \sim 5AGeV$, and the Super Proton Synchrotron (SPS) at CERN, which collides various nuclei including lead (Pb) at $\sqrt{s_{NN}} \sim 20AGeV$.

The STAR detector (Solenoidal Tracker at RHIC) is comprised of several subsystems including a solenoidal magnet, a collection of particle detectors, and several triggers detectors. The solenoidal magnet is a water cooled design with a maximum field of $0.5T$. A Time Projection Chamber (TPC) is the main tracking device. Also present in the year 1 detector subsystems were a Ring Imaging Cherenkov (RICH) detector and a section of a Silicon Vertex Tracker (SVT). Additional detector subsystems were installed for the year 2 data acquisition, including the full SVT, and upgrades will continue throughout the life of the experiment. Events were triggered

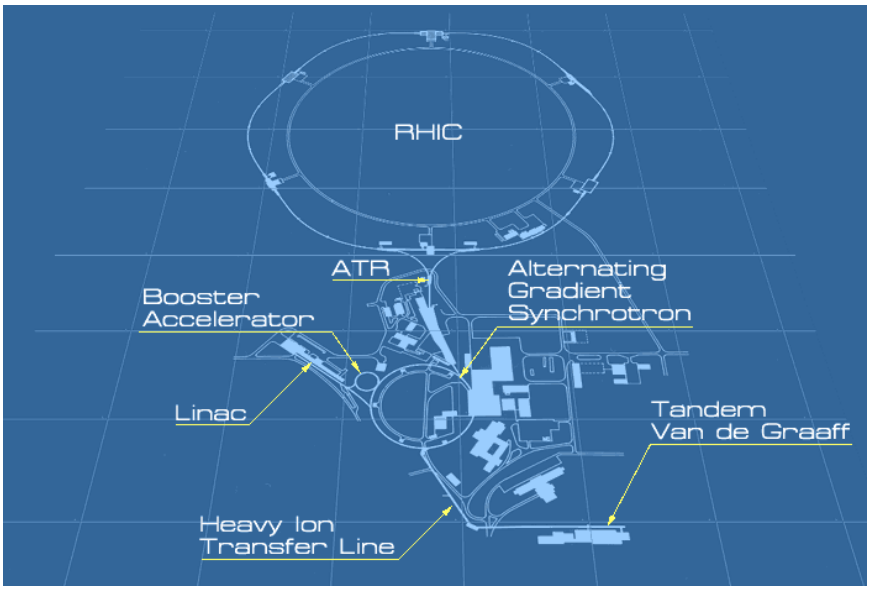

Figure 3.1: Schematic of the RHIC acclerator complex. The circumference of the RHIC ring is approximately 2.4 miles.

using a pair of detectors called the Central Trigger Barrel and Zero Degree Calorimeters. A library of software has been developed to operate the detector subsystems as well as reconstruct the recorded events. The STAR detector is shown in Fig. 3.2.

Year 1 data was recorded between June and September of 2000. Approximately 1 million minimum–bias events and 1 million central events were collected at a collision energy of $130 AGeV$. A percentage of these consist of beam gas events where a collision occurs between the Au beam and remnant gas particles in the beam pipe. The usable volume of minimum–bias data consisted of $\sim 150,000$ events.

3.1 The RHIC Accelerator

The beamline for the RHIC complex begins at a Tandem Van de Graaff (TVdG), which was developed as the first ion accelerator at Brookhaven National Laboratory

in the late 1960's. It consists of a pair of electrostatic accelerators that accelerate ions through a maximum potential difference of approximately $15.5MV$. This facility was used to accelerate the gold ions, emitted from a filament, which were then passed through a transfer line to the AGS Booster where the ion beams were further accelerated to 37% of the speed of light. During this process, gold foils along the beampipe serve to further ionize the gold atoms.

In addition to further accelerating the gold beam, the AGS serves to focus the beam through the use of an alterating gradient field produced by 240 magnets within the ring. The focusing also serves to remove any nuclei which are not fully ionized. The maximum energy of the beam from the AGS is $\sim 10AGeV$. At this point, the gold ions are traveling at $.997c$. From here they are transferred to the RHIC.

The RHIC consists of a pair of synchrotron accelerators, where the nuclei are further accelerated to their collision energy of up to $100GeV$. The transfer between the AGS and RHIC takes place through a switching magnet which send the ions through to one of the two beam pipes. Each beam orbit is 2.4 miles in circumference with six interaction points. The STAR experiment is located at the 6 o'clock position while the other RHIC experiments are positioned such that: BRAHMS (2 o'clock), PHENIX (8 o'clock), and PHOBOS (10 o'clock). At each interaction point, the two beam pipes converge allowing the crossing gold beams to interact. The crossing angle for gold ions is $\sim 100\mu rad$ [45]. The beam luminosity for 2000 was approximately 2.5% of design, $\sim 5 \times 10^{26}\ cm^{-2}\ s^{-1}$.

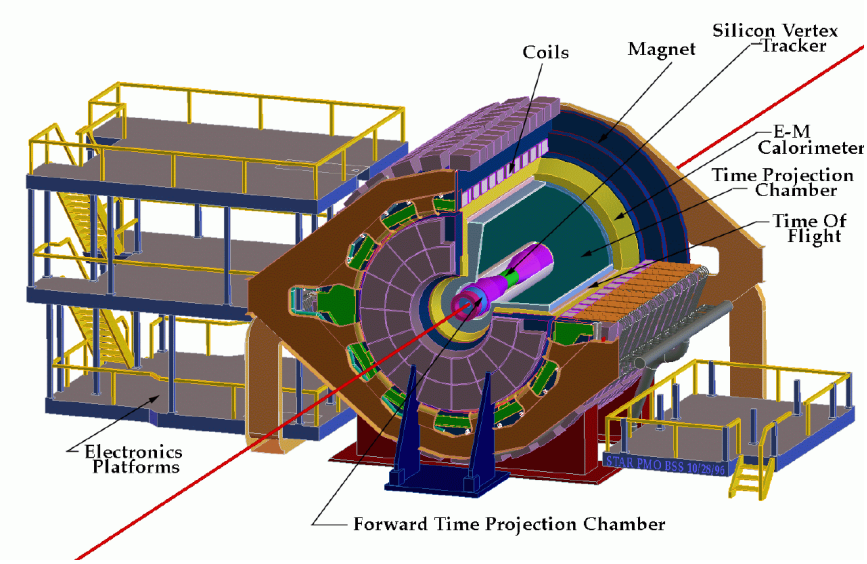

Figure 3.2: The STAR detector

3.2 The STAR Detector

3.2.1 STAR Magnet

The STAR magnet was designed to provide a uniform magnetic field along the beam direction. Originally it was designed to be a liquid helium cooled superconducting solenoidal magnet with an inner radius of $2.3m$ [46]. To reduce capital costs and allow for additional detector subsystems to be placed radially within the magnet, the design was changed to consist of a water cooled conventional warm coil copper solenoid. The new design increased the inner radius to $2.6m$ with the solenoid coils sandwiched to leave gaps allowing detector wiring to pass through. Iron return poles and yoke consisting of 30 longitudinal bars were used for field shaping/uniformity [47]. The magnet is capable of producing a magnetic field strength up to $0.5T$ requiring $1MW$ of power.

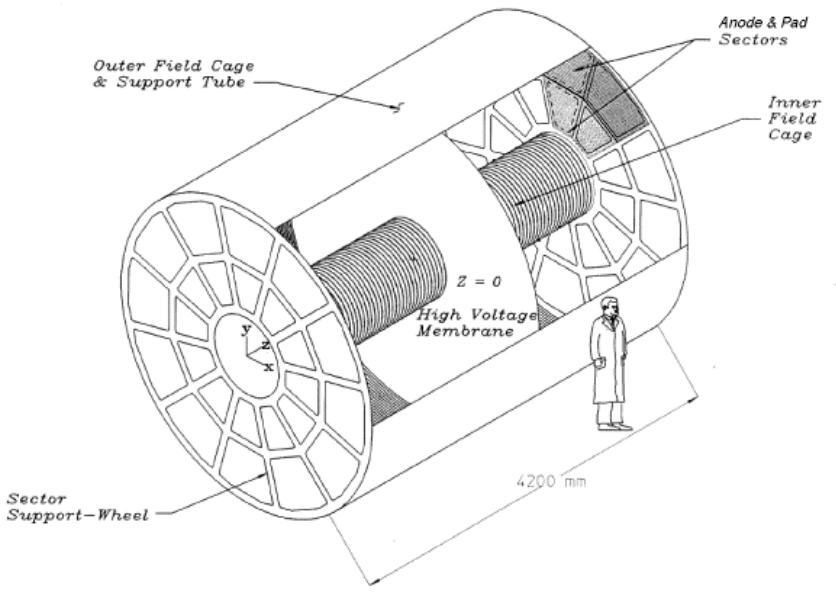

Figure 3.3: The Time Projection Chamber of the STAR detector.

The magnetic field is used to provide momentum reconstruction. In addition, the design applying electric and magnetic fields in alignment reduced signal diffusion from the dispersion of gas ionizations as they drifted towards the endcaps. Charged tracks passing through the detectors within the STAR magnet are curved to form helical tracks (if one ignores energy loss). The actual track model uses a Kalman fitter which corrects for energy loss assuming a pion mass thus allowing the momentum and charge of tracks to be determined.

3.2.2 Time Projection Chamber

The main tracking device for the STAR experiment is the Time Projection Chamber (TPC) which is a $4.2m$ long annulus with an (inner)outer radius of $(0.5)2.0m$. The readout electronics located on the end caps divide the volume of the TPC into 12

sectors with each sector further divided into 2 subsectors. The volume of the TPC is also divided into east to west halves by a high voltage central membrane and is filled with a mixture of Methane and Argon gas, $P10$. The central membrane produces a strong $\vec{E}$ field causing the electrons of the gas ionizations to drift towards the end caps. The geometry of the TPC is such that particle tracking is done for $|\eta| < 1.5$ [see Appendix A], a rapidity window containing most of the produced particles for most central collisions [46, 48]. The TPC is shown in Fig. 3.3 and was the only detector used for the event reconstruction of this analysis.

Each of the 12 sectors of the TPC is subdivided into inner and outer subsectors characterized by a change in the readout padrow geometry. The pad design consists of straight rows of pads in each subsector and is shown in Fig. 3.4. The design of the subsectors was intended to enhance the event reconstruction in two important ways. The inner sector, where the track/hit density is highest, used a smaller size pad, $2.85 \times 11.5mm^2$, in 13 rows to improve the hit resolution. This will improve tracking by reducing the occurences of split tracks which is very important for many analyses including HBT. In the outer sector, where the track density decreases, the focus of the pad geometry is on particle indentification. In this way, the pad size is increased to improve the measurements of the gas ionization. The outer subsector consists of 32 rows of $6.2 \times 19.5mm^2$ [46, 47].

The TPC gas chamber is surrounded by both an inner and outer field cage which controls the voltage drop and subsequent electric field between the high voltage central membrane and a multiwire proportional chamber (MWPC) and gating grid located just above the pad array for the two sections of each sector in the TPC. The electrons produced from particles ionizing the gas as they traverse the detector drift towards

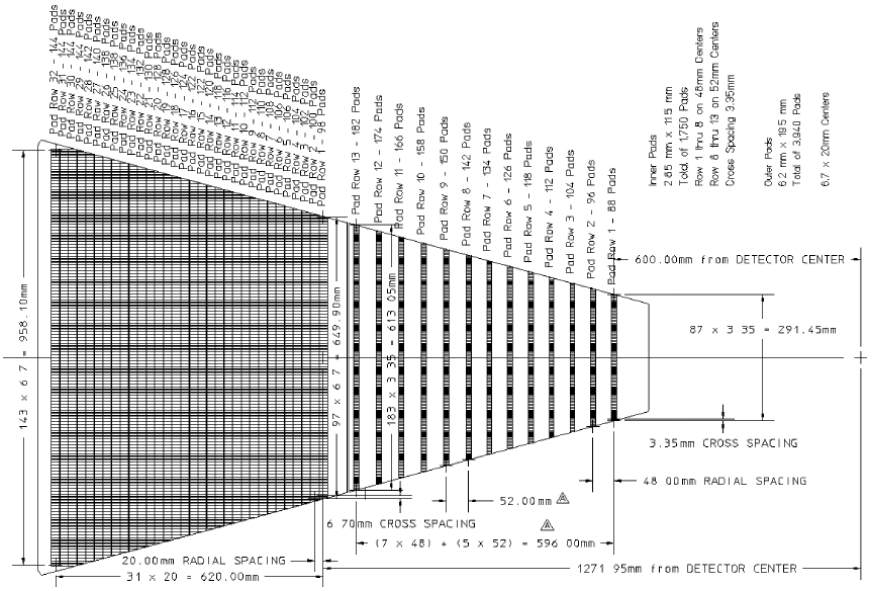

Figure 3.4: The pad layout for a sector of the TPC in STAR.

the ends of TPC and are amplified as an avalanche of electrons by the MWPC. This charge buildup is imaged onto the pads and read out with a sampling rate of $100MHz$, binned into 512 time buckets. The electrode geometry of the MWPC is shown in Fig. 3.5 and again shows a change in design elements between the inner and outer subsectors [49].

The choice of drift gas was based on several features necessary for optimal TPC performance. Among them were the constraints that the gas be under atmospheric pressure, and that the gas must have a drift velocity $v_{dft} > 2.0cm/\mu s$ in an electric field $E < 300V/cm$. A mixture of 90% argon to 10% methane (P10) was selected. The drift speed of P10 at $130V/cm$ is $5.5cm/\mu s$. Also of importance is the signal broadening introduced to the hit reconstruction by diffusion of the drift electrons in

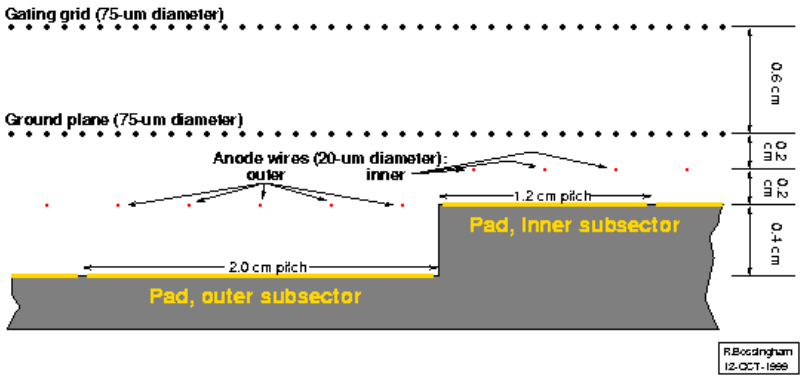

Figure 3.5: Layout of the MWPC subsectors of the TPC in STAR.

the gas chamber. The diffusion coefficients for $P10$ in the beam (transverse) direction are 320 ($540\mu m/\sqrt{cm}$) which correspond to signal widths of 0.3 ($0.8cm$) [46].

3.2.3 RICH & SVT

In addition to the main tracking detector, the STAR detector included a pair of novel detectors, the RICH and a partial installation of the SVT. The RICH is a prototypes of a detector system to be used in the ALICE/CERN experiment while the SVT is a novel drift detector made of silicon. The RICH detector is intended to extend the particle identification abilities of STAR to higher p_T, $\sim 3GeV/c$ for pions and kaons and $\sim 5GeV/c$ for protons [50]. Particle identification is done through measurements of the Cherenkov light produced when faster–than–light particles pass through the detector medium. The RICH detector was located at mid–rapidity along the $-y$ axis. The SVT installation for year 1 consisted of 1 of 36 ladders of the full SVT detector located also at midrapidity but along the $+y$ axis. The full SVT detector was installed for year 2 operation and is expected to improve the resolution of

both the primary vertex and the particle momentum. In addition, its close proximity to the primary vertex provided a better opportunity to measure short–lived particles such as Λ's.

3.2.4 Triggers

When the beam collision rate exceeds the rate at which the detector can record data, one must utilize a collection of "fast" detectors, referred to as trigger detector, to make quick decisions regarding the recording of a particular event. In addition, one may constrain the types of events saved to disk by triggering on specific event classes such as central events which are identified via their higher than average multiplicities. The year 1 triggers for STAR used two detector types, the Central Trigger Barrel (CTB) and two Zero Degree Calorimeters (ZDC).

Central Trigger Barrel

The central trigger barrel consists of 240 scintillator slats, forming an annulus just outside the STAR TPC, connected to photo multiplier tubes (PMT). Each CTB slat subtends a 6^o azimuthal angle while having a 0.5 acceptance in rapidity. The complete CTB has full azimuthal coverage and 2 units of psuedorapidity acceptance, $-1 < \eta < 1$ [51]. The CTB provides a fast measure of the particle multiplicity at midrapidity. The particles which traverse the CTB excite the scintillator medium which emits light that is detected by the PMTs. This process is substantially faster than the time required for the signal in the TPC to drift to the readout electronics on the end caps, $\sim 0.4\mu s$. This provides event triggering at $2.4MHz$. The signal from the CTB is positively correlated to the multiplicity.

Zero Degree Calorimeters

The ZDC's are a pair of calorimeter detectors located $\sim \pm 20m$ down the beam pipe, just beyond the dipole magnets used for beam steering, and have a theta coverage of $\sim 2.5mrad$. The coincidence of these signals allows discrimination against beam–gas events which would produce a signal in only one ZDC. As with the CTB, the ZDC's provide a measure of the multiplicity of particles passing though the detector, but in this case they measure the neutral spectator fragments from the collision. The production of fragment nucleons from a heavy ion collision is correlated to the centrality of the collision for very peripheral events and anticorrelated for central events.

The trigger for year 1 consisted of a combination of the signals from the CTB and the ZDC's. A plot of the CTB v. ZDC signal is shown in Fig. 3.6. The minimum–bias trigger used to collect the data used in this analysis constisted of coincidence signals in both ZDCs above threshold. The minimumbias trigger combines a coincidence cut on the ZDC signal with a requirement for the CTB signal to be above threshold. This produces an event multplicity distribution proportional to the scattering cross-section of the nuclei.

3.3 Event Reconstruction

The task of the event reconstruction software is to take the digital information from the detectors and convert it into reconstructed track from which the properties of particles emitted from the collision can be extracted. The process of event reconstruction consists of three basic steps:

1. **Hitfinding**: Locating the positions in the detectors where a track passed.

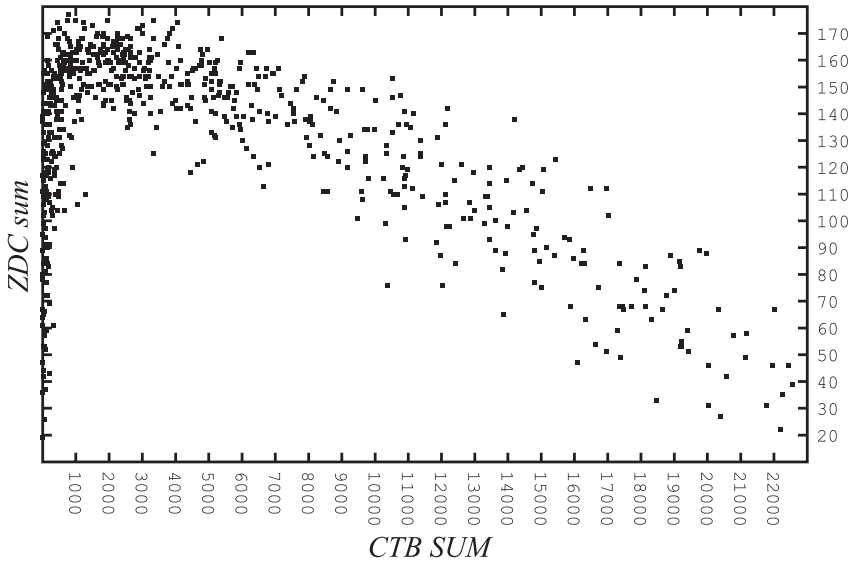

Figure 3.6: A plot of ZDC v. CTB signal.

2. **Trackfinding**: Reconstructing the tracks as sub–collections of hits which represent that paths of particles emitted from the collision.

3. **Main vertex finding**: Reconstructing the primary vertex from the track collection

Hit–finding

The hitfinding process of the event reconstruction is broken into two modules TCL and TPH which perform separate operations in the task of taking the raw data from the STAR TPC and forming a list of hit positions. The TCL module is designed to form hit clusters from the raw data tables written out by the data aquisition (DAQ). These clusters are then passed to the TPH module which forms hits from the

clusters and converts the padrow information into (x, y, z) coordinates. The hitfinding algorithm is described in detail in [9].

TCL constructs hit clusters from the output of the STAR data aquisition. The first step in the cluster formation is to generate a list of data "sequences". Sequences are lists of time buckets for a single TPC pad which contains ADC values above the readout threshold. The ADC data for one timebucket on one pad is referred to as a pixel. Each STAR event contains approximately 70 million pixels with an estimated 10% occupancy from a $Au + Au$ event. A searching algorithm is then used to group the data sequences into hit clusters. The algorithm begins at one "end" of the TPC (early time bucket of a low pad number) and finds a sequence which is not presently part of a cluster, the seed sequence. It then searches for additional unused sequences which overlap the seed or the partially constructed cluster. This process is continued until all possible clusters have been found.

Each cluster is then passed to the TPH module to deconvolute the information into hit positions. The track density in the TPC, especially in the inner subsector, is such that many TCL clusters will consist of multiple hits. The TPH module performs a peak finding algorithm to search each cluster for multiple peaks in the pad–time bucket–ADC space. Due to the finite size of each of these dimensions, multiple hits within a single cluster cannot always be resolved. This is referred to as hit–merging. The estimated merging distance in the (x, y) plane is approximately $1.5cm$. The hits found are then transformed to (x, y, z) coordinates with the z coordinate lying along the drift axis in the TPC, hence the z coordinate is calculated from the time bucket information and the known drift velocity.

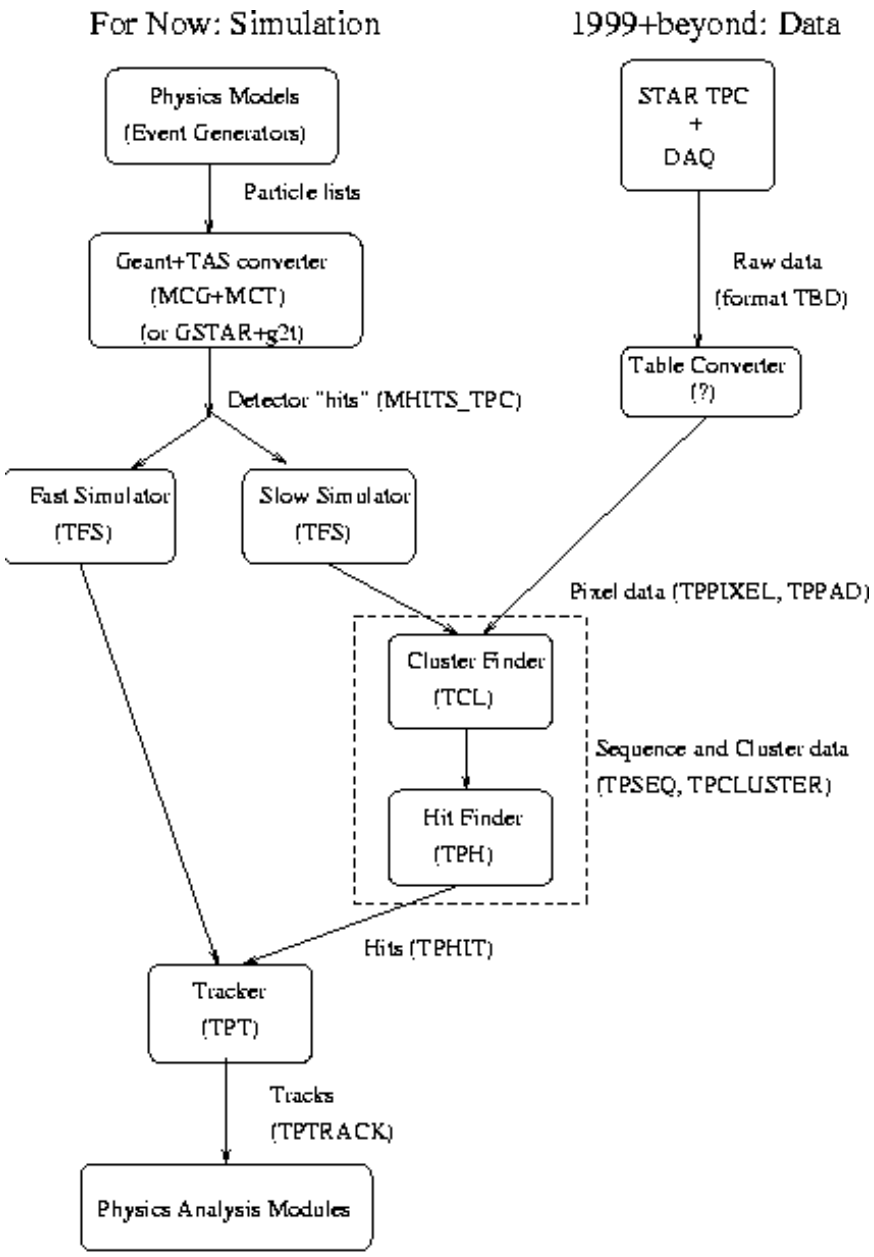

Figure 3.7: A flow chart of the event reconstruction code [9].

Track–finding

The track reconstruction module TPT fits helices to the hits provided by the hitfinding module. The track reconstruction process has four main substeps: "root" formation, segment formation, segment merging, and helix fitting. First a 3–point root is found by searching from the outside–in in the TPC for 3 hits which pass certain cuts indicating a possible track. This root is then extrapolated to search for additional hits to extend the root to a track segment. The extrapolation is done in two planes, the (x, y) and (s, z), due to the helical trajectories the track take within the TPC [52]. This produces tracks which are circular in the transverse plane and straight lines in the (s, z) plane. Here s is the path length of the track. After all segments have been formed, TPT attempts to extend segments to merge any "split" tracks. This is done by comparing helix parameters such as the helix center and radius. Finally, the segments are passed to a Kalman fitter to extract physical parameters for each track such as the transverse momentum, p_T, and particle charge. The Kalman uses a modified helical model which accounts for energy loss of the particles as they pass through the volume of the TPC. The particles charge is determined by correlating the curvature direction of the track and the magnetic field.

Main Vertex Finding

The event primary vertex is calculated through an iterative procedure which projects the track collection to an estimated primary vertex [53]. The solenoidal geometry of the STAR detector allows one to project along the beam direction or within the transverse plane to the beam point. Since the collision vertex is expected to vary by many centimeters along the beam axis, the projection was made in the

transverse plane. Initially, the entire track collection is used to estimate the main vertex position. Some of the reconstructed tracks, such as decay products or low momentum particles, will have large distances separating them from the calculated main vertex. These *outliers* are removed from the track collection for subsequent main vertex calculations. This interative procedure converges within 3–4 interations with a vertex resolution of $\sim 200\mu m$ in each direction [53].

Momentum resolution

By embedding monte carlo tracks into real events, an estimate of the momentum resolution can be obtained. The momentum resolution decreases at both high and low p_T. This is caused by multiple Coulomb scattering at low p_T while at high p_T it is caused by a reduction in the resolution of track curvature. The momentum resolution of pions in the p_T range used in this analysis is $< 5\%$.

Particle Identification

The magnitude of produced charge ionized in the TPC is proportional to the amount of energy lost. The energy lost by a particle as it travels through a gas is dependent on the velocity at which it travels and is described by a Bethe–Bloch formula,

$$-\frac{dE}{dx} = \kappa z^2 \frac{Z}{A}\frac{1}{\beta^2}\left[\frac{1}{2}\ln\frac{2m_e c^2\gamma^2\beta^2}{I^2}E_{kin} - \beta^2 - \frac{\delta}{2}\right]. \tag{3.1}$$

The Bethe–Bloch formula provides an expression for the average energy loss of a particle traversing a material and is described in detail in [54]. For each track, a truncated mean of the energy is made by removing the top 30% of ionization values along the path length of the track. The energy loss values follow a Landau distribution and with a finite number of dE/dx datum, the distribution is skewed towards higher

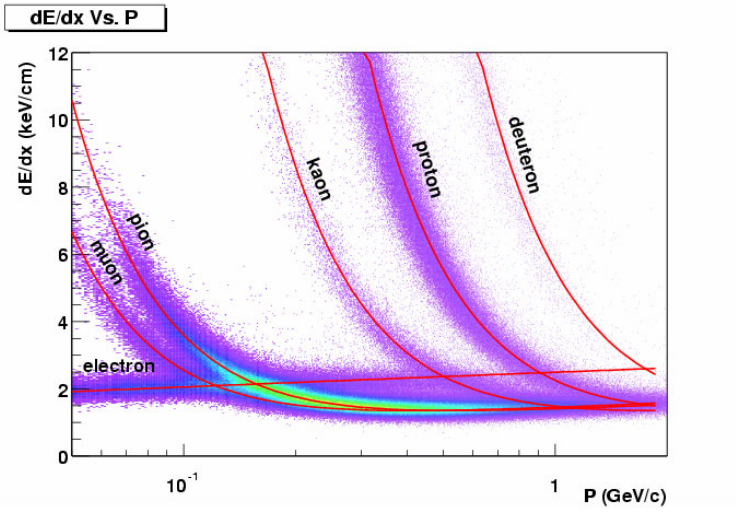

Figure 3.8: Particle identification via truncated mean energy loss vx. p values with the expected values obtained from a Bethe–Bloch parametrization.

average values. By truncating, the distribution becomes more Gaussian in which the mean is closer to the peak. For a given momentum, each particle mass will have a different velocity and hence a different dE/dx. Therefore by plotting dE/dx vs. p for all tracks, particle identification is possible. Fig. 3.8 shows the measured energy loss distribution. The curves represent the Bethe–Bloch curves for the various particles.

CHAPTER 4

DATA ANALYSIS

The previous chapters have introduced the analysis and described the detector used to collect the data analyzed. This chapter will present the method used to analyze the data and discuss issues of importance to event plane pion interferometry. Well known effects such as track splitting/merging are discussed as well as methods used to lessen the computing time required to analyze the large number of events. In addition several analysis techniques used to take into account the imperfections of the STAR detector (and how it effects event plane interferometry) are presented.

4.1 DSTs $\rightarrow$ μDSTs

The first step in the process of analyzing the data taken from the STAR detector was to reconstruct the events into collections of tracks and associated hits. This reconstructed data, referred to as data storage tape (DSTs), is then written to disk. These files are further reduced within the framework of an HBT analysis to separate the necessary data and written out to a smaller class of files called micro-DSTs (μDSTs). These typically consist of various event and track parameters such as the event multiplicity and the track DCA's, the smallest distance between a track and the collision point, while removing less important quantities. This results in faster I/O

for analysis jobs and allows for more exploration with systematic studies. For the year 1 data, taken in the summer of 2000, there are approximately 2,300 minimum–bias event DST files each of which held about 70 events for a total of ∼150,000 minimum–bias events. The decrease in data volume is accounted for by beam–gas events and low multiplicity events for which a usable event plane cannot be determined.

4.2 Event Selection

In HBT one wishes to obtain the space–time dimensions of the particle emmitting source through the study of the momentum–space distributions of particles. To do this effectively one must remove detector effects from the data sample. The construction of the HBT correlation function as the ratio of real event particle pairs, pairs from the same event, to background particle pairs, pairs taken from mixed events, provides the functionality of removing detector single particle acceptance effects. The effectiveness of this method requires that only events with similar characteristics be included in an analysis. There are 3 main identifying characteristics of events: event multiplicity, primary vertex position, and the orientation of the event plane. The mixing of dissimilar events in these categories introduces systematic behavior which corrupts the physics signal. Is this section I will discuss how these systematic behaviors are introduced, and observed in addition to the methods we used to remove these effects.

The structure of the *StHbtMaker* allows for multidimensional binning of the events within an analysis. The method creates a series of mixing buffers separating the events into different classes as they are read in. This way, only events within the same buffer are mixed, removing effects due to mixing different classes of events. While this

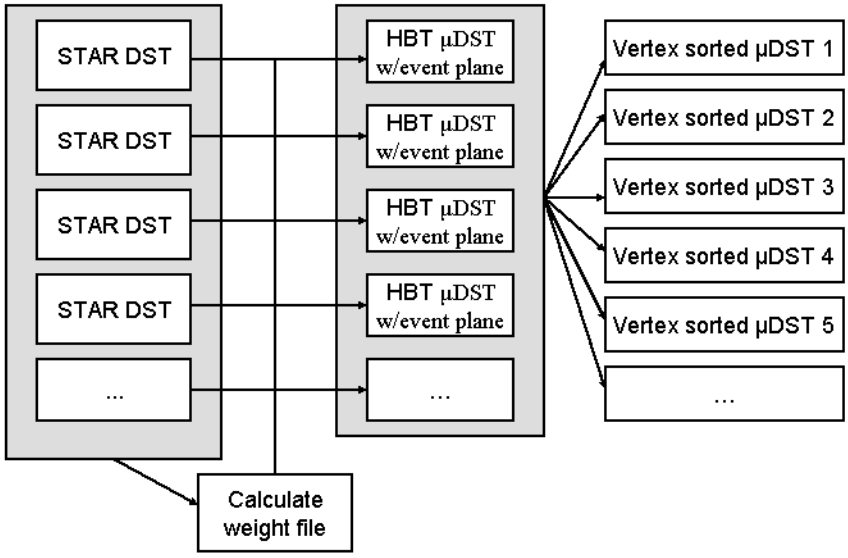

Figure 4.1: Flow chart of the process to make the μDSTs.

method is perfectly acceptable from a physics point of view, it can put tremendous demands on the computing environment one works under. This is due to the fact that numerous events are held in memory at one time, since previous events are used to mix with the current events as they are read in. It also requires one to process large amounts of data at one time to allow enough events to be read in to fill each mixing buffer and begin event mixing. To alleviate the computing requirements of the analysis, a new set of μDSTs were made to incorporate event binning according to the z_{vtx} position of the events in this analysis. A flow chart showing the process from a collection of DSTs to a set of ordered μDSTs is shown in Fig. 4.1. The two other binnings were done within the analysis.

Figure 4.2: Diagram showing simplified TPC acceptance of detector (box) of 2 events at the edge of the detector geometry. Reconstructed tracks are solid arrows, while un–reconstructed are dotted arrows.

4.2.1 Primary Vertex Position

We chose to create a set of μDSTs to separate the events according to the primary vertex position. This was done in a 2–step process. First, the original STAR DSTs were written to a set of μDSTs which required the primary vertex be within $75cm$ of the center of the TPC. These μDSTs were then read and written to a set of vertex–dependent μDSTs. For this analysis, the events were written to files containing events within $0.5cm$ "bins". This created a set of 300 μDSTs each of which contained events with a z_{vtx} within $0.5cm$ of some nominal position. A collection of sub–analyses were then run in parallel, each on a subset of the 300 files. The output histograms (numerator and denominator) were then added post run–time to create the correlation function for the entire data set.

There are 2 possible problems associated with mixing events with different primary vertex positions along the beam. The first is that the detector acceptance can change when one varies the location of the primary vertex. The change in acceptance will

introduce systematics to the correlation function formed with these events. This becomes obvious if we consider a box–like detector, which is similar to the TPC, with two events centered at different edges of the detector, see Fig. 4.2.

If we put both of these events into the same analysis mixing buffer, the numerator made from each event separately will contain low–q pairs, but when we form the denominator it will have reduced low–q statistics and enhanced high–q statistics. This comes about from the relative rapidity acceptance of the two events; the rapidity distribution for one event will be shifted towards $+y$ while the other event will be shifted towards $-y$. Fig. 4.3 shows the effect of mixing events with large differences in z_{vtx} position. The q_l projection shows a long slope in the correlation function tail which reduces the normalization of the correlation function. The reduction in the normalization is seen in the q_o and q_s projections. Along each of the three axes, the correlation function should asymptote to 1. When the q_l dependence continues to fall, the out and side components are shifted up. The data in Fig 4.3 show the out and side components asymptoting to a value greater than 1.

There are several techniques for removing this effect from the data: reduce the z_{vtx} range of accepted events (Fig. 4.4); reduce the rapidity range of accepted particles (Fig. 4.5); or to mix only events with similar z_{vtx} by binning the event collection (Fig. 4.6). Figs. 4.4 –4.6 show the desired correction effects. Each of these procedures will correct the correlation function for effects due to rapidity acceptance, but the first two methods reduce the amount of data. Therefore, we have chosen to create a binning of the events according to the vertex position and mix only events with similar verticies.

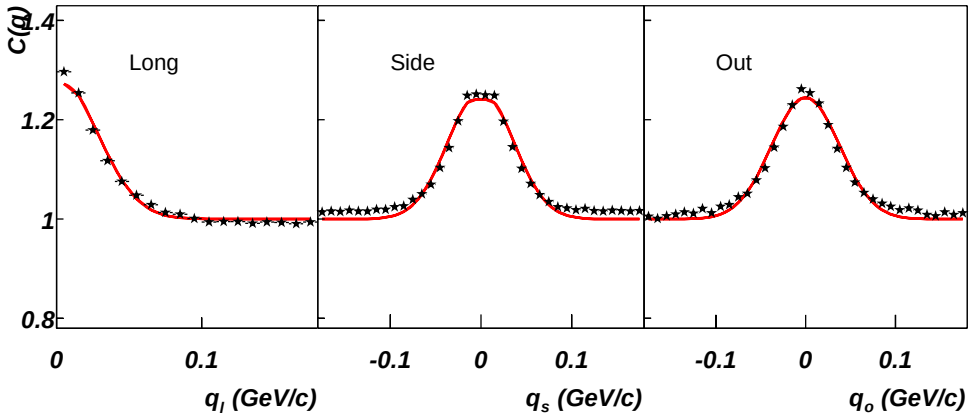

Figure 4.3: Bertsch-Pratt projections for an analysis with no vertex binning. The event vertices vary from $-75 < z_{vtx} < 75cm$ with a cut on rapidity $-1 < y < 1$. Of note is the slope in q_l which forces the normalization lower. This is evident in the offset between the data (black stars) and the fit (red line) in q_o and q_s.

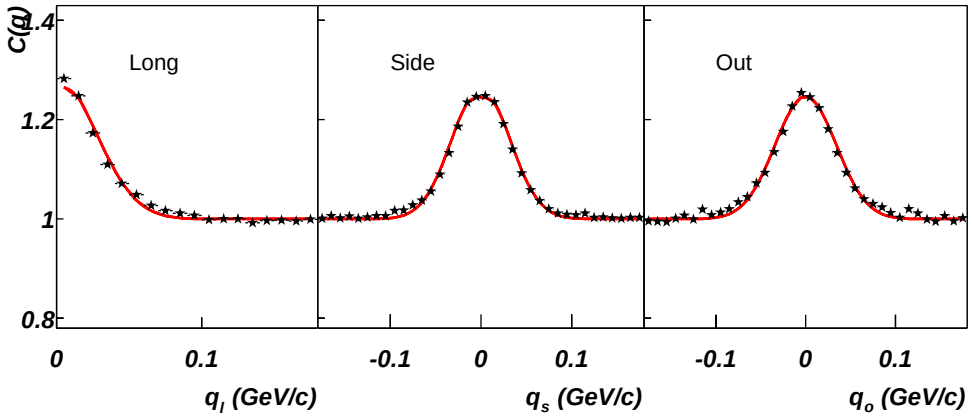

Figure 4.4: Bertsch-Pratt projections for an analysis with no vertex binning but a tighter cut on vertex position. The event vertices vary from $-35 < z_{vtx} < 35cm$ with a cut on rapidity of $-1 < y < 1$. Of note is the reduced slope in q_l improving the agreement between the data and the Gaussian fit (red line) when compared to Fig. 4.3.

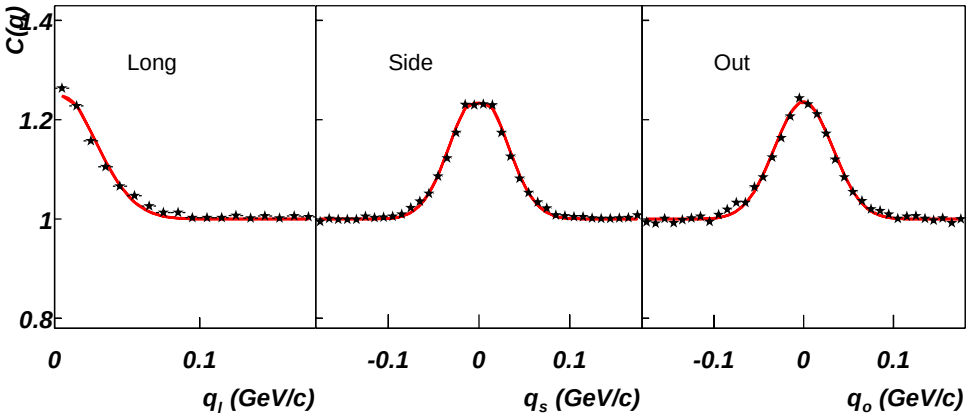

Figure 4.5: Bertsch-Pratt projections for an analysis with no vertex binning but a tighter cut on track rapidity. The event vertices vary from $-75 < z_{vtx} < 75cm$ while the rapidity cut is $-0.5 < y < 0.5$. Of note is the reduced slope in q_l improving the agreement between the data and the Gaussian fit (red line) when compared to Fig. 4.3.

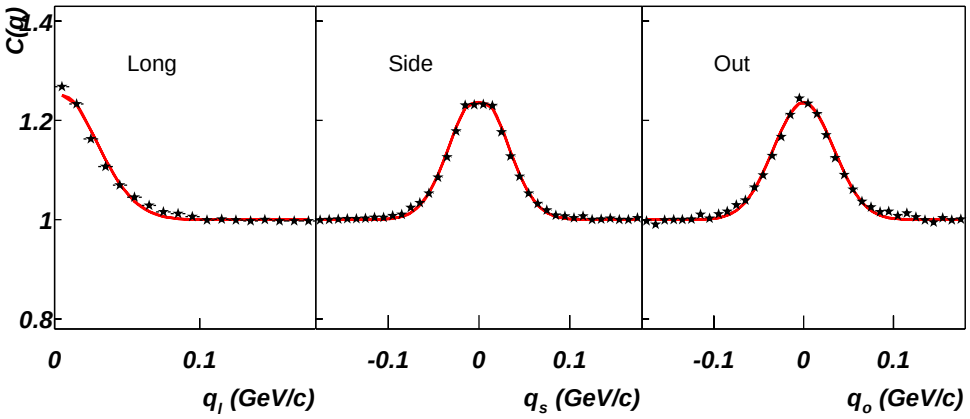

Figure 4.6: Bertsch-Pratt projections for an analysis with 10 cm vertex binning. The event vertices vary from $-75 < z_{vtx} < 75cm$ with a rapidity cut of $-1 < y < 1$. Of note is the reduced slope in q_l improving the agreement between the data and the Gaussian fit (red line) when compared to Fig. 4.3.

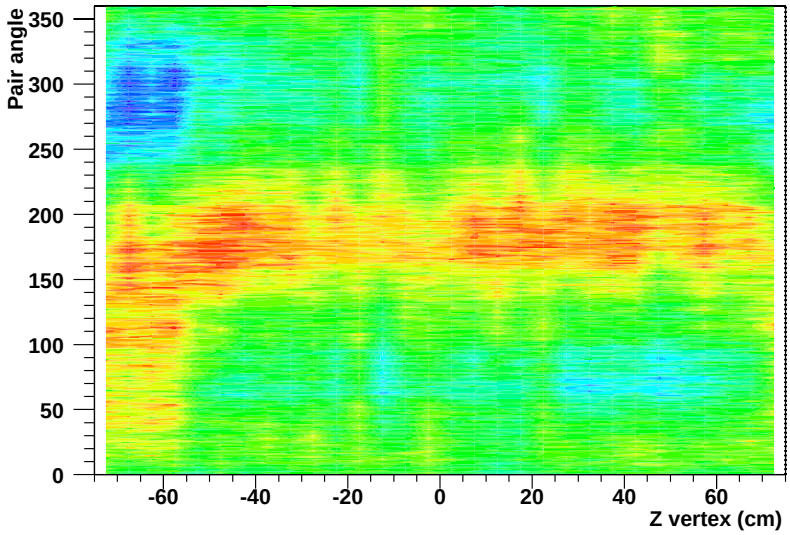

Figure 4.7: Azimuthal acceptance distribution of π^- pairs versus z_{vtx}.

In addition, the azimuthal acceptance of the detector changes as one varies the z_{vtx} position due to variances in the material present. Although the STAR detector was designed to have good azimuthal acceptance, changes in the z_{vtx} dependence of the particle acceptance are present and Figs. 4.7 and 4.8 show the vertex dependence of the azimuthal acceptance of π^- (π^+) pairs. Structures present in the distributions can be attributed to changes in the material between the collision point and the TPC.

The presence of material between the detector and the beam pipe cause different affects on the two charged pions, whose scattering cross–section are dependent on momentum [55]. It was discussed in [56] that while negatively charged pions scatter while passing through material, positively charged pions can be absorbed due to the different scattering cross–sections between charged pions and nucleons. A measure of the presence of material can be seen be looking at the distribution of photon

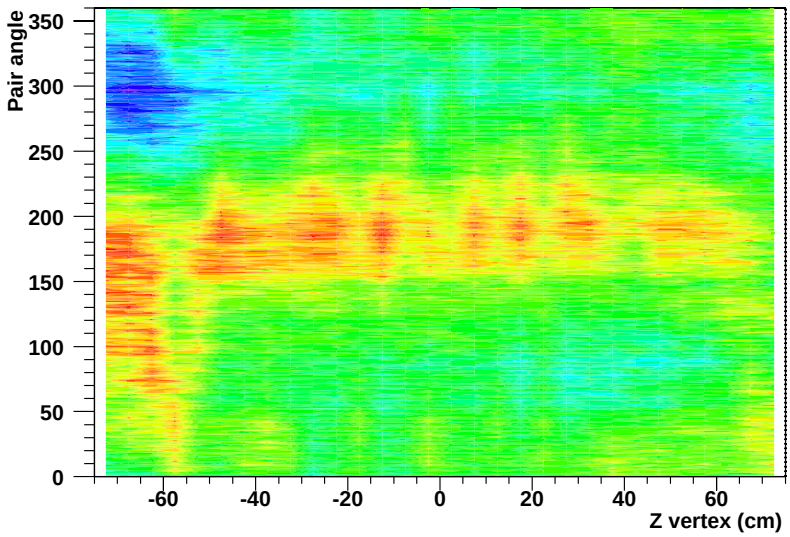

Figure 4.8: Azimuthal acceptance distribution of π^+ pairs versus z_{vtx}.

production points, $Z + \gamma \rightarrow Z + e^- + e^+$, seen in Fig. 4.9. The distribution shows a large increase in material present at $|z_{vtx}| \sim 55cm$ which corresponds to the location of the SVT and beam pipe support cone. For this analysis, an additional cut was applied to limit the $z_{vtx} < 55cm$ and hence the effects from material presence.

4.2.2 Event Centrality

In addition to the z_{vtx} binning built into the μDSTs, two event binnings were included in the analysis. The first of these was a binning with respect to the centrality of the collision. As seen in Fig. 4.10, the geometry of the overlap region is dependent on the magnitude of the impact parameter. In addition to the change in geometry, the centrality of the collision changes the dynamic properties of the system.

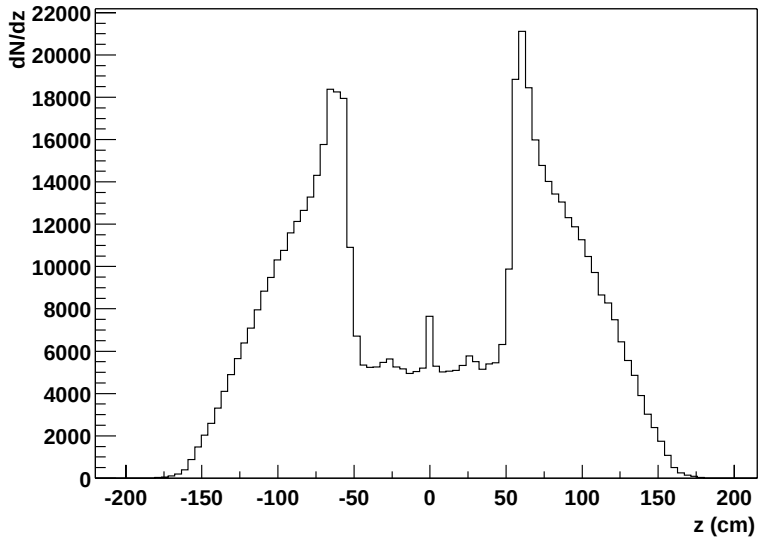

Figure 4.9: "Z" distribution of photon conversion points serving as an indicator of the amount of material between the emission region and the detector [10].

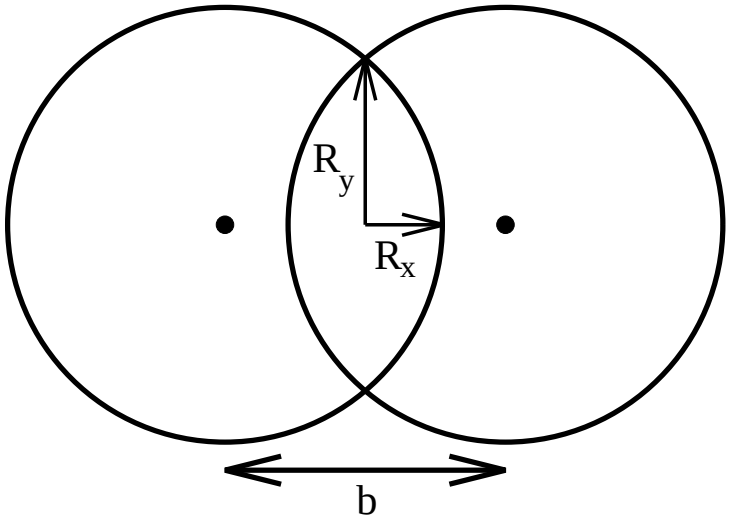

Figure 4.10: Dependence of the overlap region on the impact parameter b for non-central collisions.

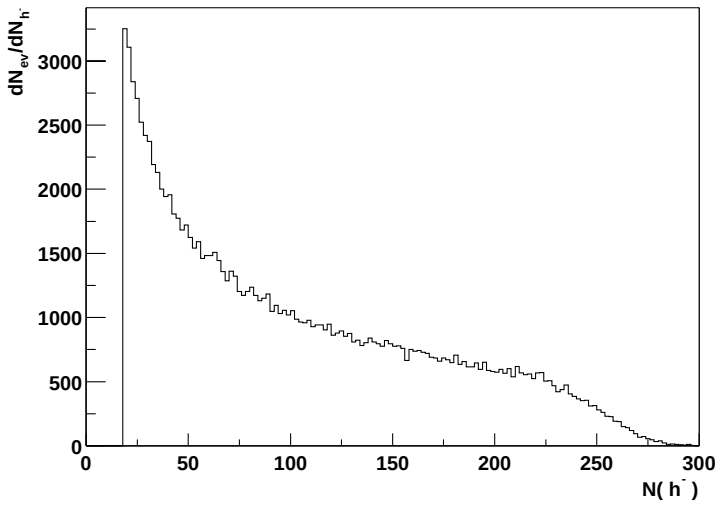

Figure 4.11: Multiplicity distribution of negative hadrons as described in the text for the minimum–bias selection of events.

The centrality of the events was estimated through the multiplicity of negative hadrons with at least 10 TPC hits, transverse DCA's less than 3 cm, and a pseudo-rapidity $|\eta| < 0.5$. This represents the STAR standard year 1 multiplicity measure. For the minimum–bias collection of events, the multiplicity varied between 0 and ~ 300 and is shown in Fig 4.11. Similar to z_{vtx}, mixing events in different centrality/multiplicty classes can introduce additional artificial structure to the correlation function. Effects to the correlation function due to multiplicity binning were studied and found to be minscule yet were included for completeness. The binning used contained 15 bins between a multiplicity of 17 to 400. The lower cut off was also used to remove low multiplicity events for which the resolution of the event plane calculation decreased and for which beam–gas contamination is high.

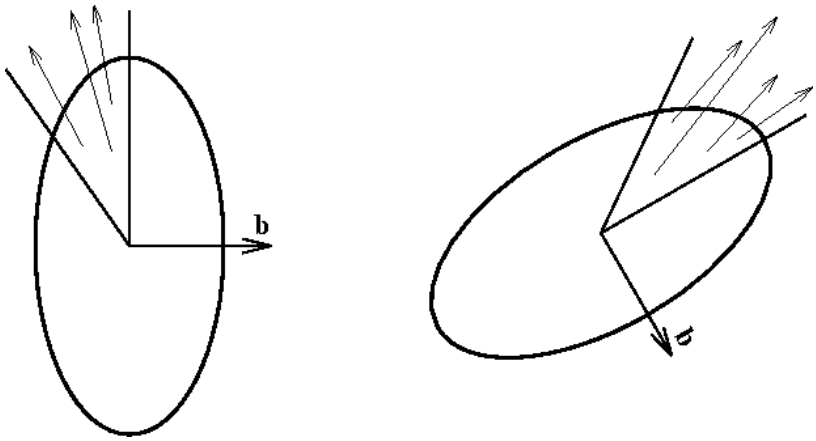

Figure 4.12: Example of two events with different laboratory event plane angles. The arrows represent particles accepted into a Φ_{rp} correlation function.

4.2.3 Event Plane Angle

In addition to binning the events according to z_{vtx} position and event multiplicity, one must also bin events according to the orientation of the event plane angle. Effects similar to those seen from vertex mixing are also present when events are mixed with different event planes. There are 3 methods one could chose to apply the event mixing within an azimuthally sensitive HBT analysis to align the events. I will briefly discuss and explain why 2 of the 3 methods will introduce detector errors to the correlation function.

The most naïve choice one could make is to do nothing to the events and analyze each in the lab frame. This choice of analysis procedure will lead to a sloping of the correlation function by introducing different relative momentum distributions in the numerator and denominator used to construct the correlation function. Fig. 4.12 shows the transverse emission regions of two possible events in the lab frame of an

experiment. The numerator for each correlation function will contain some collection of particle pairs with low–q. When one forms the denominator by mixing particles from the two events there will be virtually no low–q counts from the restriction on the relative emission angles in the correlation function and the lack of overlap in momentum space.

Another method one may chose would be to rotate events so all the event planes point in the same direction in the lab frame, say horizontally, and then analyze. In this case, the ability of the correlation function to divide out detector acceptance effects is diminished since the single–particle (and two particle) acceptances are no longer identical for "real" and "mixed" pair distributions. The effects on the correlation function in this case are not limited to the low–q region and vary depending on the geometry of the detector used.

The 3^{rd} method of aligning events within this analysis is to separate the events into a collection of bins according to the orientation of the event plane. This method continues to align the detector geometries in addition to the momentum–space acceptance of the events contained in each event mixing buffer. This is the method used in this analysis where bin widths were 7.5^{o}.

4.3 Particle Selection

After one selects the events to include in the analysis, a series of tests/cuts need to be applied to the collection of particle tracks in the events to select the desired particles to be used in the HBT analysis. As described in Chapter 3, particle identification was done through the specific ionization of the particles in the TPC. A correlation

between the momentum of the particle and the specific ionization allows one to perform particle identification. Through a set of "NSigma" cuts, a collection of particles containing pions and removing protons and kaons was made. For this analysis, pions were selected by requiring the deviation of the specific ionization to be within 2 standard deviations of the Bethe–Bloche value. These distributions are formed by projecting the dE/dx vs. p 2–dimensional distribution along sections in momentum space and fitting to a Gaussian. One however, must also consider the momentum resolution of the detector in the range of phase–space studied. We focused this analysis where the momentum resolution for pions was best, $125 < p_T < 450 MeV/c$. Below $125 MeV/c$, multiple Coulomb scattering reduces the momentum resolution of the tracking software while above $450 MeV/c$ track merging (see Sec. 4.4.2) reduces the ability to identify separate tracks. Within this range, the momentum resolution was about 2.5% [57]. To remove contributions from non-primary particles with pion decays (e.g. K and Λ) we applied a DCA (distance of closest approach to the primary vertex) cut of $3cm$ to the track collection.

4.4 Pair Selection

Results from particle interferometry require an accurate measurement of the momentum difference between pairs of particles and is very sensitive to the quality of the low relative momentum region where the quantum enhancement occurs. It is this region of phasespace in which two event reconstruction effects come into play for interferometric analyses. Here I will describe those effects and the procedures applied for removal and correction of the data.

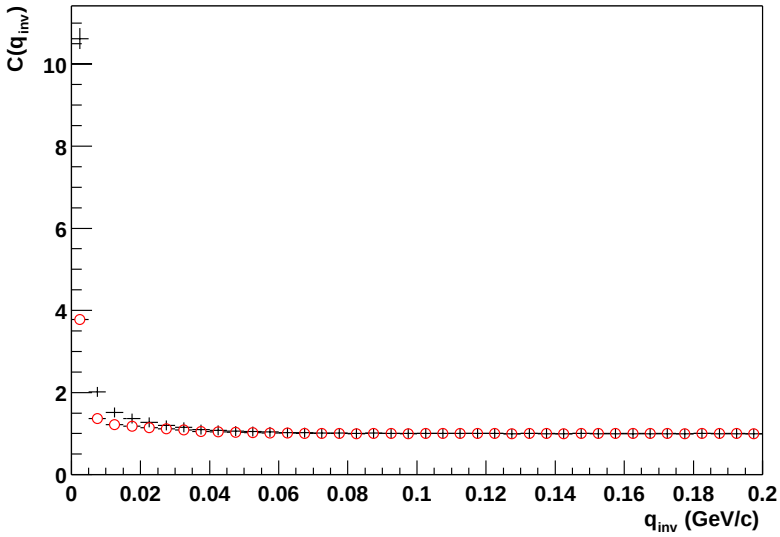

Figure 4.13: Plot of $C(q_{inv})$ to show the effects of track splitting on a correlation function from raw data (red circles) and Coulomb corrected raw data (black crosses). Of note is the large value obtained for $q_{inv} \sim 5MeV/c$.

4.4.1 Track Splitting

As described in Chapter 3, particle hits are grouped to form tracks. In the process of forming tracks, the event reconstruction code can reconstruct two separate tracks from the hits left in the TPC from one actual particle; this is referred to as track splitting. Track splitting creates an enhancement primarily in the low–q region of the correlation function and is evidenced by unphysical values for the correlation function, $C(q) > 2.0$. This is caused by an increase in the number of low–q pairs in the real event distribution as single tracks artificially appear twice with approximately the same momentum. An example of a correlation function suffering the effects of track splitting is seen in Fig. 4.13. Using a topological track measure described

below, the amount of track splitting present in the year 2000 data was found to be $\sim$ 1%. For most any other analysis in STAR, this magnitude of track splitting is negligible. However, for HBT studies the presence of even a small amount of track splitting is critical. The effects of track splitting occur exactly where the HBT signal is present and where the amount of "real" pairs is small. The primary cause of track splitting is from segmented tracks. This occurs when the track finding algorithm fails to merge two sections of track separated by a collection of empty pad rows or the sector boundaries.

A simple method to remove track splitting would be to require each track to have greater than half the number of possible hits. This method fails in HBT since it will remove good tracks thereby introducing track merging effects. To correct for track splitting, a topological cut was applied to track pairs. For each track reconstructed in the TPC, an associated hit–map is formed which represents the pad row locations of hits along the reconstructed track. This hit–map consists of a binary string of length 45 (one bit for each pad row) for which "1" indicates the presence of a hit on that padrow while "0" indicates the absence of a hit on that pad row. The hit–map does not differentiate between pad rows from separate sectors of the TPC.

As an example, the hit–map for a track with hits in pad rows 1, 4, 5, 6, 13, and 14 would be represented by: ...011000000111001. From the hit map, we can compare the hit topologies of the track pairs in the analysis to estimate the likelihood of the pair being a split track. If a single track passed through some volume of the TPC, it should be expected to leave a maximum of 1 hit on each pad row. Track pairs which consist of disjoint hit locations indicate the likelihood that they are due to a split

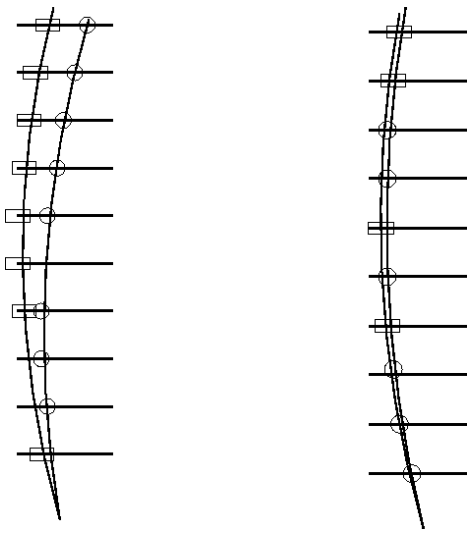

Figure 4.14: Examples of how the topology map is used to identify split tracks. Closed squares and open circles represent separate reconstructed tracks. On the left are two separate tracks while on the right is a likely split track candidate.

track. A diagram showing example hit locations for two cases of track pairs is shown in Fig. 4.14.

To remove existing split tracks from the analysis, we construct the "quality factor":

$$F_{Quality} = \frac{\sum_{n=1}^{45} A(n)}{\sum NHits}, \tag{4.1}$$

where:

$$A(n) = \begin{cases} 1 & \text{if both tracks have hits on pad row n} \\ 0 & \text{if neither track has a hit on pad row n} \\ -1 & \text{if only one track has a hit on pad row n} \end{cases}$$

describes the occupancy level of the pad row. The range of the quality factor is $[-0.5, 1.0]$. A high quality factor, $F_{Quality} \sim 1.0$, indicates a high likelihood of the track pair being due to a split track. Fig. 4.15 shows 2D plots of the numerator, denominator, and ratio of the correlation function plotted versus q_{inv} and $F_{Quality}$. The characteristic effects of track splitting are seen in both the numerator and the

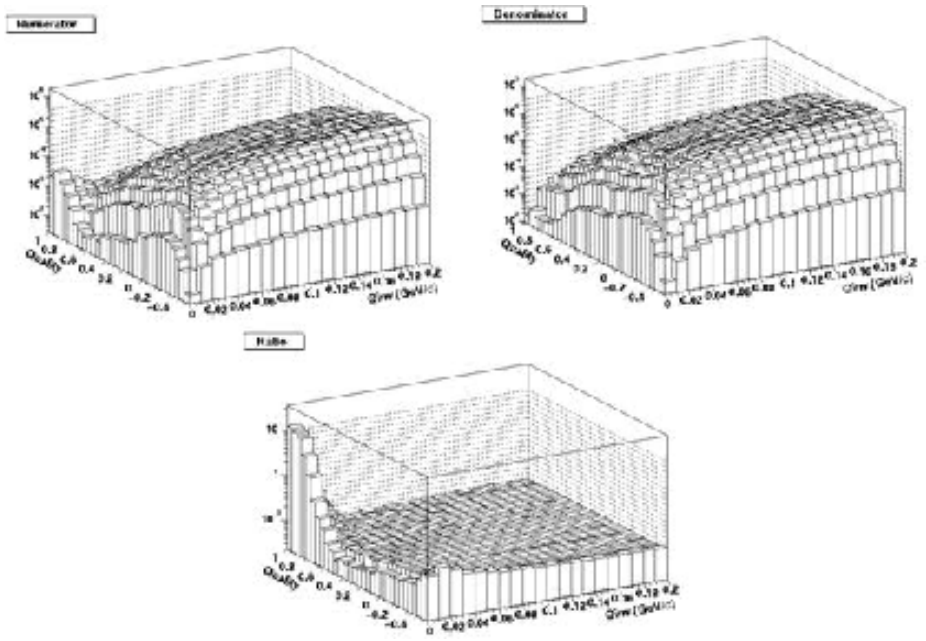

Figure 4.15: 2D histograms of the correlation function, $C(q_{inv}, F_{Quality})$ for 100K central events for Au + Au at $\sqrt{s_{NN}} = 130 GeV/c$. Shown are: (clockwise from top left) numerator, denominator, and ratio.

ratio histograms at large quality factor and small relative momentum. A series of projections of the correlation function are shown in Fig. 4.16. These projections are used to determine the degree to which cuts on the quality factor are able to remove effects due to track splitting. From these projections, a value of 0.6 was found as the most effective at removing split tracks while retaining a large fraction of the data. For this analysis a range of $-0.5 < F_{Quality} < 0.6$ was used. Simulation studies of a correlated pion source indicated that a $F_{Quality} = 0.6$ was a good value to remove the occurence of track splitting. This was later confirmed through analysis of the year 1 data.

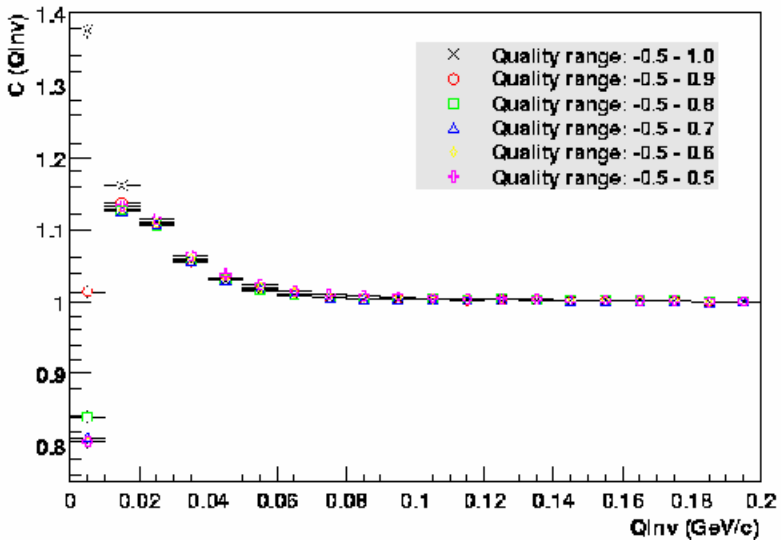

Figure 4.16: Projections of the 1D q_{inv} correlation function for various ranges of "split quality" for 100K central events for Au + Au at $\sqrt{s_{NN}} = 130 GeV/c$.

4.4.2 Track Merging

In addition to track splitting, additional low–q detector effects are seen due to track merging. In this case, the reconstruction software mis-identifies a real pair of particle tracks as one reconstructed track. Where track splitting caused an enhancement of low–q pairs in the correlation function, track merging has the opposite effect; it causes a depression in the low–q behavior of the correlation function.

To remove effects due to track merging, we used a cut on the separation distance between tracks within the TPC. There were 3 variations of separation cut tested within the HBT group: entrance separation, exit separation, and average separation. The first two cases are self-explanatory; they tested the separation between tracks when they entered(exited) the TPC at corresponding radii of 50(200)cm. The 3^{rd} cut

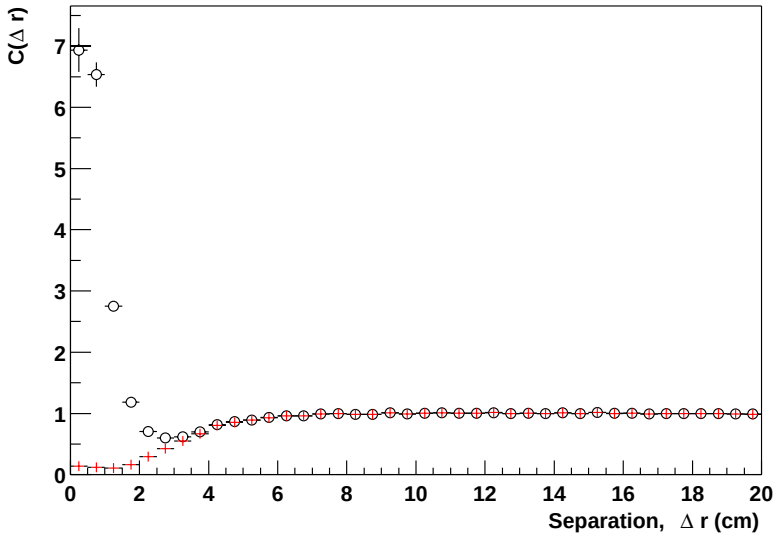

Figure 4.17: Track pair average separation (Δr) correlation function for all track pairs (black open circles) and track pairs after removal of split track candidates (red crosses).

was an average of the separation between tracks at 11 radial distances within the TPC in increments of $15cm$ beginning at the entrance radius of $50cm$. Fig. 4.17 shows the distribution of pair average separation for real events normalized by the distribution in mixed events for all pairs (open circles) and pairs which pass the track splitting cut (red crosses). The decrease in "real" track pairs, reducing the correlation function, below $\sim 6cm$ in both data sets is indicative of track merging. In addition, the open circles indicate the presence and dominance of track splitting for track separations $< 3cm$.

Note that all pair cuts (and other cuts) must be applied equally to both the numerator and denominator, to preserve identical phasespace and acceptance properties. In the case of track splitting, the primary "action" is within the numerator

	Source 1	Source 2
λ	0.45	0.55
R_o	4.3	20.0
R_s	4.5	13.0
R_l	5.0	13.0

Table 4.1: Source parameters for the event mix simulation used to model the effects due to the separation cut.

("real events"), whereas the antimerging cut, the average separation within the TPC, acts primarily on the denominator ("mixed events"). The average separation cut removes pairs from the "mixed pair" distribution which would have been merged if both tracks from the pair were present in the same event.

In addition to removing effects due to track merging, the separation cut also introduced systematic behavior to the HBT radii seen in Fig. 4.18. These effects were studied extensively in the azimuthally integrated analysis. For the diagonal fit parameters (λ, R_o^2, R_s^2, and R_l^2) the merging cut systematically reduced the parameters as the separation cut was increased. This was attributed to non–Gaussianness in the correlation function combined with the separation cut's preferential removal of low–q pairs. The same behavior is observed in the azimuthally sensitive analysis. Fig. 4.18 shows the systematic behavior introduced to the HBT parameters due to the separation cut as crosses. The dependence of a simulated double–Gaussian source to the separation cut is also shown as open circles. The Gaussian parameters used in the simulation are given in Table 4.1.

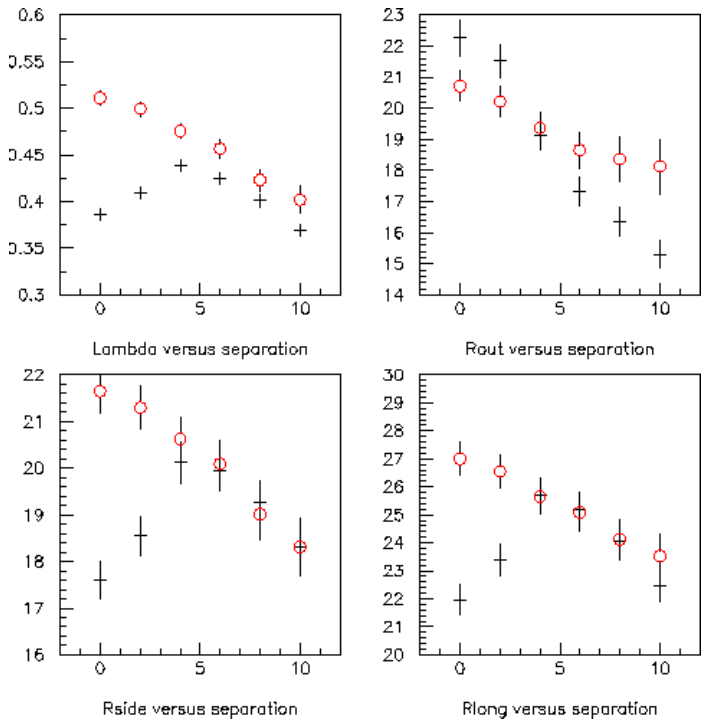

Figure 4.18: Systematic behavior of diagonal HBT parameters introduced by the average separation cut for both raw data (red crosses) and a simulated double–Guassian source (open circles).

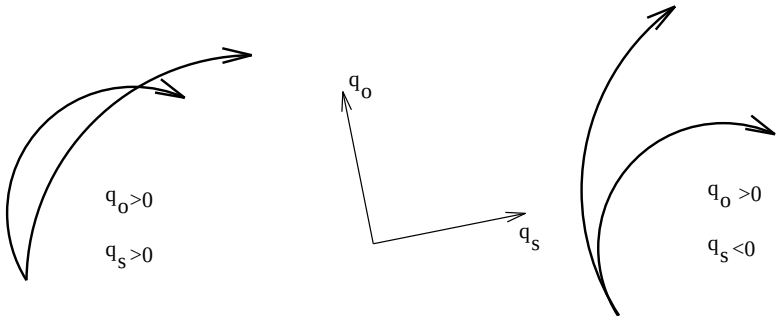

Figure 4.19: Two π^- track pairs showing the higher likelihood of track merging for pairs with a positive correlation between q_0 and q_s.

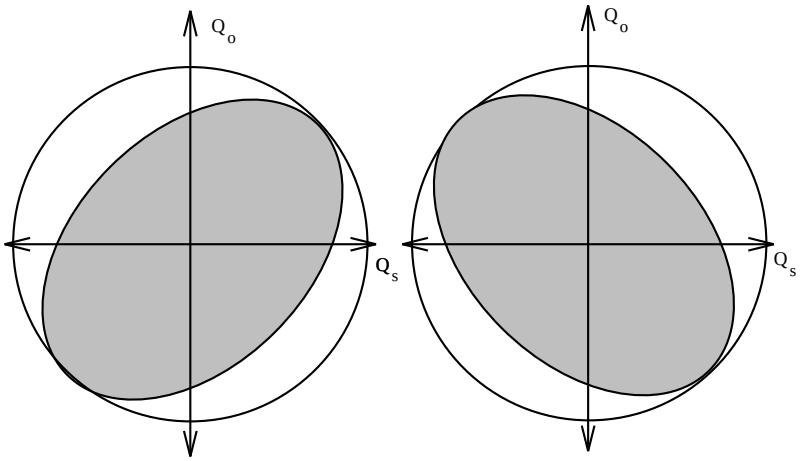

Figure 4.20: Diagram showing the change in the correlation function from an originally cylindrical source to an artificially tilted ellipsoidal source due to track merging. On the left is the tilted source caused from preferential removal of track pairs in quadrants 2 & 4 associated with π^+ while on the right is the tilted source from π^-.

The presence of track merging also introduces a systematic shift in the off–diagonal HBT radii within azimuthally sensitive analyses. Fitting a sinusoidal function,

$$R^2_{os} = p_0 + p_2 \ \sin(2\phi), \tag{4.2}$$

to the ϕ dependence of the R^2_{os} radius parameter indicated a systematic offset seen as a nonzero p_0. The cause of the offset is a preferential merging of track pairs with correlated transverse momenta, q_o and q_s as shown for π^- pairs in Fig. 4.19. In the case of π^-, there is a higher degree of track merging when $|q_o q_s| = q_o q_s$ than when $|q_o q_s| \neq q_o q_s$. For π^+, which rotate in the opposite direction, the conditions are reversed. In this way, track merging introduces a tilt in the Out–Side plane of the correlation function. For π^- the track merging removes more pairs from quadrants 1 and 3 introducing a positive tilt while for π^+ more pairs are removed from quadrants

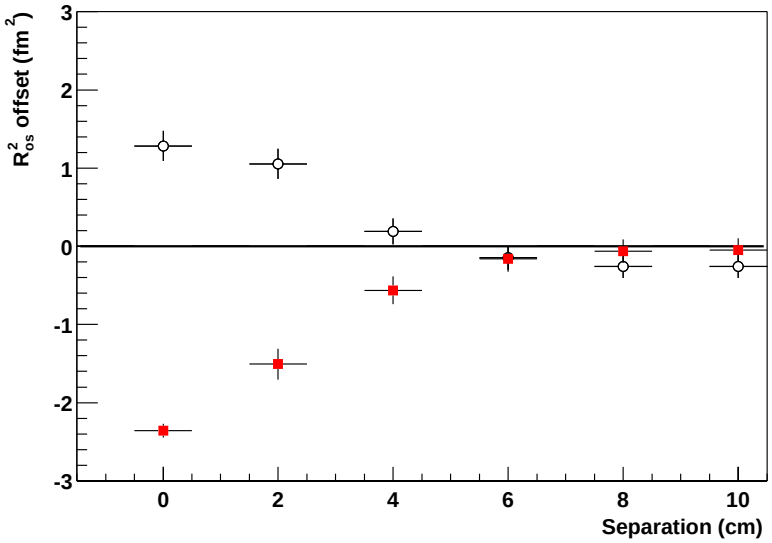

Figure 4.21: Dependence of R^2_{os} radius fit parameter, p_0, to the average track pair separation. The offsets for π^- (π^+) are shown as black open circles (red closed squares).

2 and 4 introducing a negative tilt. Fig. 4.20 shows the artificial tilt introduced to the pion source from the preferential removal of pairs correlated or anticorrelated in transverse momenta. Fig. 4.21 shows the dependence of p_0 from (4.2) on the separation cut for both π^- and π^+ analyses. Measuring the offset in the R^2_{os} radii provided another estimate of the effective lower bound to the average separation cut, $6cm$. An advantage in this case is that we know that the offset R_0 must be zero [58], providing a non–subjective standard with which to work.

4.5 Coulomb Correction

As discussed in Chapter 2, there is a Coulomb interaction between emitted particles which is not accounted for in theoretical derivations of the correlation function.

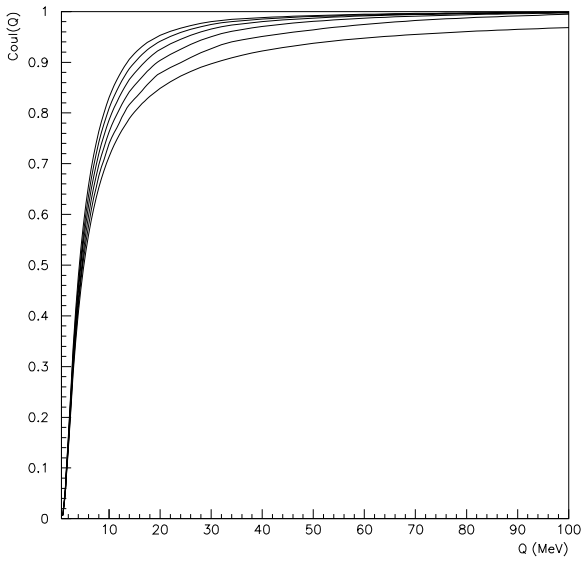

Figure 4.22: Coulomb weight as a function of relative momentum for radii (bottom–top)0, 4, 6, 8, 12, 16, $20fm$ for like sign pion pairs.

The Coulomb interaction causes a reduction in the low–q counts in the real pairs of the correlation function which reduces the correlation function. This can be seen in Fig. 2.2 where the open circles are the correlation functions prior to Coulomb corrections. To correct for this, a Coulomb weighting is applied to the denominator to account for the loss of pairs in the numerator [29]. Fig. 4.22 shows the Coulomb weight as a function of relative momentum for various source radii.

To determine this weighting factor, the Coulomb wave function was integrated and a correction value obtained for a series of spherical Gaussian sources of various radii, $0 - 20fm$ in $2fm$ increments, and pair relative velocity. This integration is quite cpu intensive. Since we need this weight for every pair in the analysis (several million), this data was tabulated into files for like and opposite sign charges:

η	$0fm$	$2fm$	...	$20fm$
η_1	$f_c(0fm, \eta_1)$	$f_c(2fm, \eta_1)$	...	$f_c(20fm, \eta_1)$
η_2	$f_c(0fm, \eta_2)$	$f_c(2fm, \eta_2)$	...	$f_c(20fm, \eta_2)$
η_3	$f_c(0fm, \eta_3)$	$f_c(2fm, \eta_3)$	...	$f_c(20fm, \eta_3)$
...	...	...	...	...

Here $\eta = Z_1 Z_2 \alpha / v_{rel}$ is a measure of the relative velocity where Z_i is the charge of particle i, $Z_i = \pm 1$. In practice, when a source radius is selected, a linear interpolating function was written to first condense the full lookup table to an array of corrections for a single source radius,

$$f_c(R, \eta) = \frac{(R - R_<) f_c(R_>, \eta) + (R_> - R) f_c(R_<, \eta)}{R_> - R_<}, \tag{4.3}$$

where $R_<(R_>)$ are the highest(lowest) radius in the full lookup table less than (greater than) the given radius, R. This then gives an array of correction values.

η_1	$f_c(R, \eta_1)$
η_2	$f_c(R, \eta_2)$
η_3	$f_c(R, \eta_3)$
...	...

Each pair to be weighted then has a given value of η. The process of interpolating between η values was done similarly to Eq. 4.3. While the radial interpolation would be done only upon the initialization of the analysis, the η interpolation was called for every pair in the denominator. To minimize the computing requirements associated with the Coulomb correction, a binary search algorithm was used to determine $\eta_<$ and $\eta_>$. This method divided the lookup array in half to determine which half contained the desired η. Through a series of these divisions, the upper and lower bounds of the η value could be found. This search procedure scales with the log of the number of entries in the data array. Search algorithms which linearly searched the data array or divided the array into equal length rows and columns were also tested. Both have performance below that of the binary search algorithm. Considerations of such

technical points are of importance to HBT studies. Correlation analyses are easily the most cpu–intensive analysis in STAR. The construction of a correlation function often takes several days, even when using an array (~ 20) computers in parallel. The performance of components used several times in an analysis (e.g. StHbtCoulomb) can determine whether a given analysis is feasible, and whether necessary checks and systematics are adequately investigated.

When one does identical particle correlations, there is a relation between η and q_{inv},

$$\eta = \frac{2Z_1 Z_2 \mu \alpha}{q_{inv}}, \tag{4.4}$$

where $\mu = \frac{m_1 m_2}{m_1 + m_2} = \frac{1}{2}m$ is the reduced mass. This relation provided the flexibility to include a "histogram" correction where a user could specify the limits of the q_{inv} histogram and receive a histogram of the correction values for the midpoints of the q_{inv} histogram bins, which allowed for the removal of the correction calculation from the mixed pair formation. This is also implemented for both the 1–dimensional q_{inv} and 3–dimensional correlation function classes. Differences between this method and the (in principle better) pair–by–pair correction procedure were seen to be small for pions. A pair–by–pair Coulomb correction for a $5fm$ source was used for this analysis.

4.6 Forming the correlation function(s)

There are a few differences between an azimuthal HBT analysis and a standard azimuthally integrated analysis. To observe the particle source from a series of angles one must construct separate correlation functions for each angle considered. The particle pairs which enter each correlation function are determined by calculating the relative angle between the pair transverse momentum, K_T, and the event plane angle,

Φ. For this analysis, four separate correlation functions were formed each with an angular width of 45^o and centered on angles: 0, 45, 90, and 135^o. For the present configuration of the STAR detector, the 1^{st} order event plane angle is not reconstuctable. This analysis was therefore done using the 2^{nd} order event plane. The 1^{st} order event plane angle tells the direction of the impact parameter, $\vec{\mathbf{b}}$, while the 2^{nd} order event plane angle is that which contains the impact parameter, but cannot discriminate between $\vec{\mathbf{b}}$ and $-\vec{\mathbf{b}}$. Therefore relative angles greater than 180^o are indistinguishable from angles $\Phi - 180^o$ as the particle pair transverse emission angle spanned the angular range of 0 to 360^o. For relative angles $\phi = \phi_{pair} - \phi_{EP} > 180^o$, the angle was transformed by subtracting 180^o. Therefore, a correlation function containing pairs centered about ϕ also contains pairs centered about $\phi + 180^o$. This restriction limits the azimuthal HBT analysis to be sensitive only to even order oscillations in the HBT fit parameters [58]. Within the restrictions of the STAR data, the transverse components of Eq. (2.32) simplify to:

$$\begin{aligned}
R_s^2 &= S_{11}\sin^2(\phi) + S_{22}\cos^2(\phi) - S_{12}\sin(2\phi) \\
R_o^2 &= S_{11}\sin^2(\phi) + S_{22}\cos^2(\phi) + S_{12}\sin(2\phi) - \\
&\quad - 2\beta_T S_{01}\cos(\phi) - 2\beta_T S_{02}\sin(\phi) + \beta_T^2 S_{00}, \\
R_{os}^2 &= S_{12}\cos^2(2\phi) + \frac{1}{2}(S_{22} - S_{11})\sin(2\phi) + \\
&\quad + \beta_T S_{01}\sin(\phi) - \beta_T S_{02}\cos(\phi), \\
R_l^2 &= S_{33} - 2\beta_l S_{03} + \beta_l^2 S_{00}
\end{aligned} \tag{4.5}$$

while the other radii: R_{ol}^2, and R_{sl}^2 vanish.

Another distinction from "standard" analyses is that one must retain the relative sign of the q components. The diagonal components of the spatial correlation tensor

provide length scales parallel to those axes. The off–diagonal terms, like R^2_{os}, provide a measure of the correlation between the q components giving a measurement of the orientation of the extension of the source. Fig. 4.23 shows the difference in the observed correlation function when one maintains the relative signs of the momentum difference (left) to the case of taking the absolute value of the momentum difference (right). The orientation of the tilt in the correlation function in q–space is lost when the absolute value is used.

To ease the demands of the computer in memory handling and swapping, the correlation function is typically reflected about one of the axes. In this analysis, the q_l component was reflected. To retain the relative q components, the other two momenta are also reflected. This method reduces the required size of the correlation function by 2.

4.6.1 Calculating the event plane angle

The experimental procedure for calculating the event plane from the DST files was a two–step process, as indicated in Fig. 4.1, built into the construction of the μDSTs. If one calculates the event plane without considerations of the acceptance of the detector, the distributions of event plane angles will be skewed by the acceptance. The first step to calculating the event plane angle was to construct a weighting file to correct for detector acceptance. With a perfect detector, a random distribution of particles should produce a flat ϕ dependence. Any structure to the ϕ dependence is indicative of acceptance effects. By then weighting the particles by the ϕ acceptance, one can correct the calculation of the event plane for detector acceptance. This was done by passing the DST events to the *StFlowMaker* which calculated the azimuthal

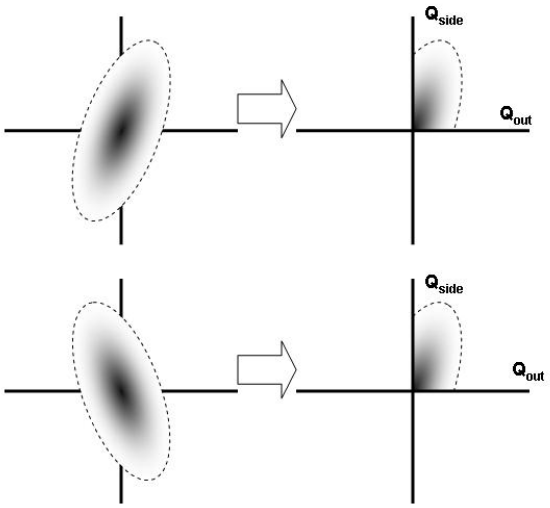

Figure 4.23: A diagram showing the effect of not considering the relative sign of the q components in an anisotropic source. The sign of the tilt angle is lost when the correlation function is folded into a single quadrant.

distributions of particles with and without p_T weighting, w_i in (2.41). These distributions were then used as an azimuthal acceptance correction to flatten the distribution of calculated event planes when the data were processed a second time [39]. As described in Chapter 2, the Event plane was calculated using the method of Poskanzer and Voloshin (2.41). The acceptance of the year 1 detector geometry was such that resolution of the first order event plane was too low to be reliable. Therefore, the second order event plane which indicates the *plane* which contains the impact parameter, but does not distinguish between angles 180 degrees apart was used.

$$\Phi_2 = \tan^{-1}\Big(\frac{\sum_i p_T \sin(2\phi_i)}{\sum_i p_T \cos(2\phi_i)}\Big)/2. \tag{4.6}$$

Here, $\phi_i = p_y/p_x$ is the transverse angle of emission for the particle. The sum in the equation is over all primary particles. An example of the event plane calculated from

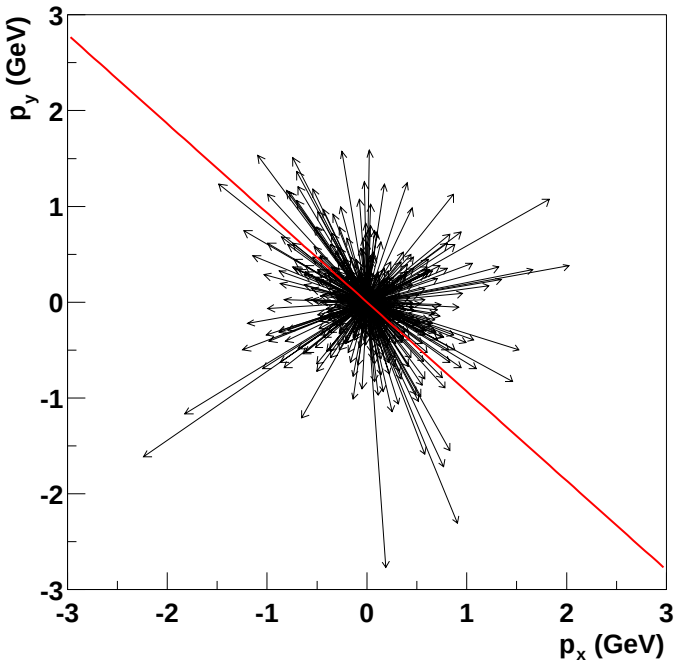

Figure 4.24: An example of the event plane calculated from a typical STAR event. The track transverse momenta (p_x, p_y) are indicated by black arrows while the reconstructed event plane is shown as a red line.

an event is shown in Fig 4.24. The event plane found from the equation represents the angle at which maximum energy is emitted from the emission region in the transverse plane. The same method was used to measure the STAR $v_2(p_T)$ [44, 12].

Finite event multplicities introduce errors to the calculation of the event plane. This causes a reduction in the magnitude of the oscillations of any variable (including $R^2_{ii}(\phi)$). Two procedures used to correct for the finite resolution of the event plane are discussed in Chapter 5. The resolution of the event plane calculation was done

through the particle flow analysis [39]

$$Res = \langle \cos(2[\phi_m - \phi_r]) \rangle = \frac{\sqrt{\pi}}{2\sqrt{2}} \chi_2 e^{-\chi_2^2/4} [I_0(\chi_2^2/4) + I_1(\chi_2^2/4)]. \tag{4.7}$$

For this analysis, $\langle \cos(2[\phi_a - \phi_b]) \rangle \sim 0.56$ which corresponds to an angular resolution of approximately 28^o.

CHAPTER 5

RESULTS AND DISCUSSION

In this chapter, the theory presented in Chapter 2 and the analysis software developed in Chapter 4 will be applied to study the azimuthal dependence of the HBT fit paramaters for $130 AGeV$ Au + Au collisions produced at RHIC and measure with the STAR detector. The data analyzed consisted of a minimum-bias collection of approximately 150,000 events recorded in the late summer of 2000. The results will be compared and interpreted within a hydrodynamic blast wave parameterization. In addition, comparisons will be made to both hydrodynamic and molecular dynamic models.

As described in Section 4.6, a series of 3–dimensional Pratt–Bertsch correlation functions are formed by binning particle pairs according to the angle between the pair momentum and the event plane. In this analysis a set of four angles were used, centered at 45, 90, 135, and 180^o; each bin has an angular width of 45^o. The 180^o correlation function is identical to 0^o and so the data points are plotted at both angles. The year 1 acceptance of the STAR detector limited the resolution of the event plane to only even order making measurements of event plane angles ϕ indistinguishable from $\phi + 180^o$. A Gaussian parameterization is used to fit the correlation functions

whose form is

$$C(\mathbf{q},\phi) = 1 + \lambda(\phi)\exp\left[-\sum_{i,j=o,s,l} q_i q_j R_{ij}^2(\phi)\right]. \tag{5.1}$$

Here, o, s, l are the Pratt–Bertsch directions (see Section 2.1.4), giving 6 independent parameters, and ϕ is the pair emission angle relative to the event plane. A combination of using the 2^{nd} order event plane and a midrapidity phase space simplifies (5.1) (see Section 2.3) to

$$C(\mathbf{q}) = 1 + \lambda e^{-q_o^2 R_o^2 - q_s^2 R_s^2 - q_l^2 R_l^2 - 2q_o q_s R_{os}^2}. \tag{5.2}$$

5.1 Separate π^- π^- & π^+ π^+ analyses

Figs. 5.1 and 5.2 show 1–dimensional projections of the correlation functions in the Pratt–Bertsch system for π^- and π^+ pairs respectively. Each row represents a different angle beginning with 45 ± 22.5^o along the top row and ending with 180 ± 22.5^o along the bottom row. The lines are projections of fits of the correlation data to (5.2). All projections are integrated over $\pm 30 MeV/c$ along the orthogonal momentum components.

The data have been corrected for both track merging and splitting as described in 4.4.1 and 4.4.2. In addition, Coulomb effects have been acccounted for by applying a correction corresponding to a $5fm$ source as described in 4.5.

Tables 5.1 (π^-) and 5.2 (π^+) list the Gaussian fit values for each relative emission angle. Note that we fit the *squared HBT radii* using a Minuit χ^2 fitting method. Figs. 5.1 and 5.2 indicate the level of agreement between the data and the Gaussian fit used to extract the source radii.

While the diagonal fit radii (R_o^2, R_s^2, and R_l^2) are required to be positive, the sign of the cross–term, R_{os}^2, is significant in that it describes the orientation of the

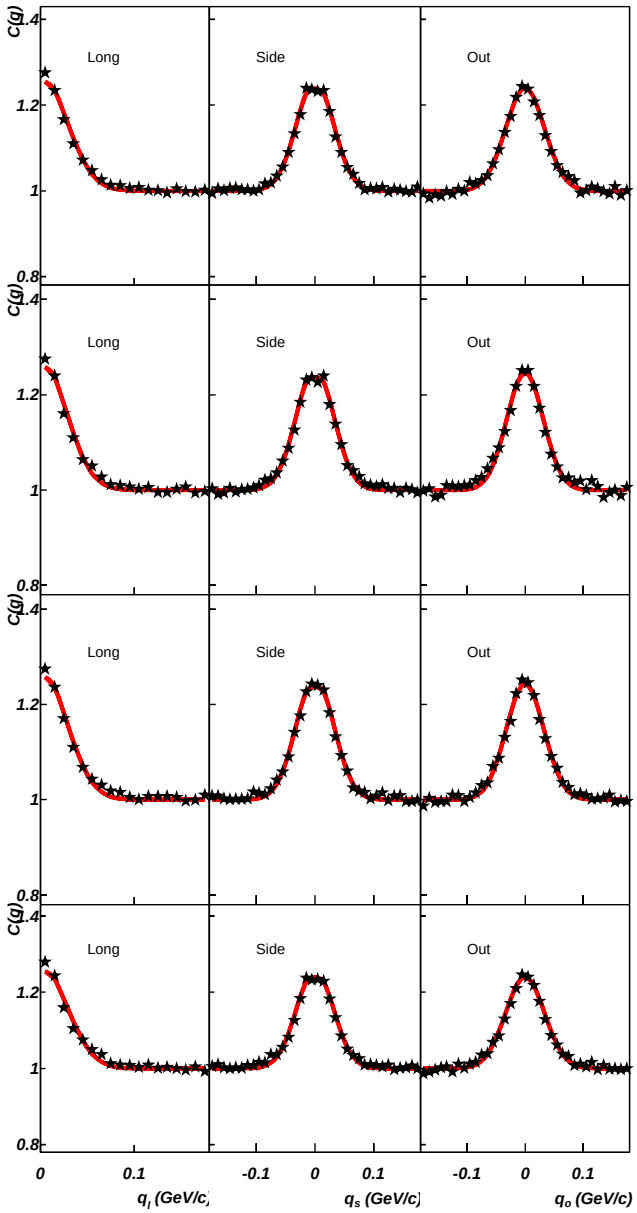

Figure 5.1: Pratt–Bertsch projections for π^- π^- pairs emitted (top–bottom) at $\phi = 45, 90, 135, 180 \pm 22.5^o$. The lines are projections of fits to (5.2). All projections are integrated over $\pm 30 MeV/c$ in the perpendicular momentum components.

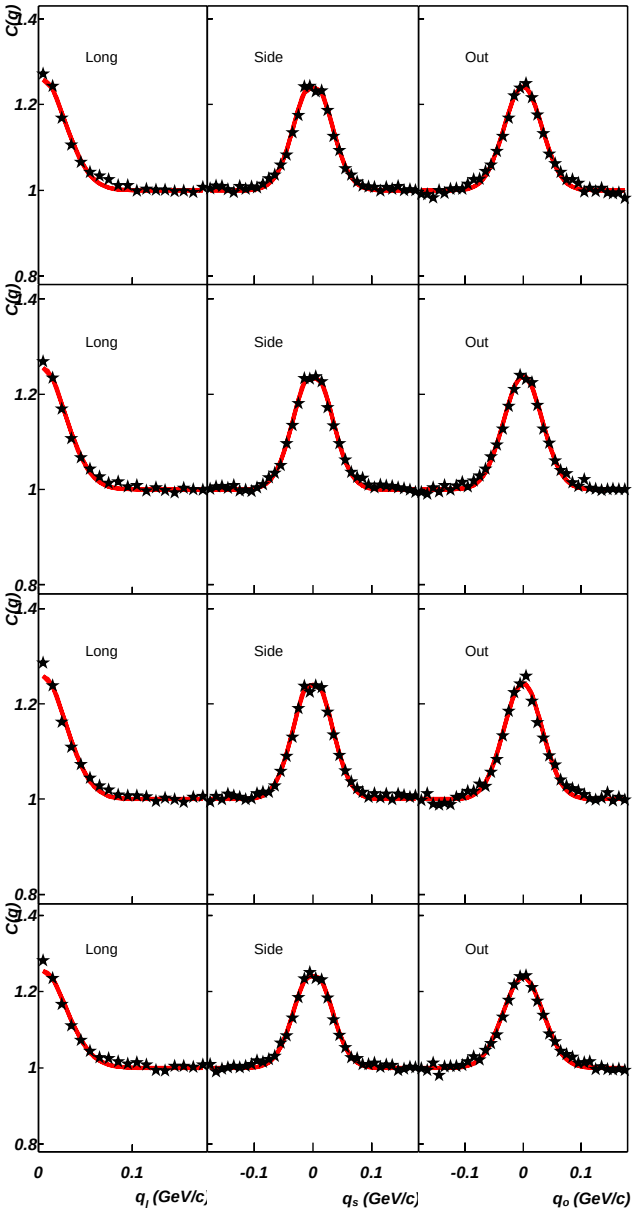

Figure 5.2: Same as Fig. 5.1, but for π^+ π^+ pairs.

ϕ (^{o})	λ	R_o^2 (fm^2)	R_s^2 (fm^2)	R_l^2 (fm^2)	R_{os}^2 (fm^2)
$0 = 180$	0.438 ± 0.007	18.0 ± 0.5	20.1 ± 0.5	25.7 ± 0.7	-0.9 ± 0.3
45	0.434 ± 0.007	17.8 ± 0.5	19.8 ± 0.5	25.3 ± 0.6	0.4 ± 0.3
90	0.442 ± 0.007	19.9 ± 0.5	19.1 ± 0.5	26.3 ± 0.7	0.2 ± 0.3
135	0.433 ± 0.007	18.3 ± 0.5	18.7 ± 0.4	25.7 ± 0.7	-0.7 ± 0.3

Table 5.1: Angular dependence of uncorrected fit parameters for (5.2) for π^- π^-.

ϕ (^{o})	λ	R_o^2 (fm^2)	R_s^2 (fm^2)	R_l^2 (fm^2)	R_{os}^2 (fm^2)
$0 = 180$	0.428 ± 0.007	16.4 ± 0.4	20.2 ± 0.5	24.8 ± 0.6	-0.1 ± 0.3
45	0.442 ± 0.007	18.6 ± 0.5	19.8 ± 0.5	26.8 ± 0.7	0.6 ± 0.3
90	0.425 ± 0.007	17.4 ± 0.5	18.8 ± 0.5	26.1 ± 0.7	-0.3 ± 0.3
135	0.436 ± 0.007	18.0 ± 0.5	19.5 ± 0.4	25.8 ± 0.7	-1.3 ± 0.3

Table 5.2: Same as Table 5.1 for π^+ π^+ pairs.

tilt of the corrrelation function in the q_o–q_s plane. As the angle varies from $0 - 180^o$, sinusoidal oscillations are observed in the transverse radii, R_o^2, R_s^2, and R_{os}^2. Theoretically, $R_{os}^2 = 0$ at both 90 and 180^o due to the symmetry of the collisions while $R_{os}^2(135^o) = -R_{os}^2(45^o)$. The longitudinal radius R_l^2 is seen to remain roughly constant, $R_l^2(\phi) \sim 26 fm^2$. The λ parameter is also expected to have no ϕ dependence. This is also seen in the fit results where $\lambda(\phi) \sim 0.44$.

The ϕ dependence of the HBT fit parameters are shown as black circles in Figs. 5.3 and 5.4. Fit parameters for $\phi = 0^o$ are also plotted as open symbols at $\phi = 180^o$. Figs 5.3 and 5.4 show that both R_s^2 and R_{os}^2 exhibit sinusoidal oscillations. The dependence of the outward radius is less certain especially in the π^- case, Fig. 5.3. This is thought to be due to the reduced statistics available in the year 1 data set. An

	$\pi-$		$\pi+$	
	$R_0\ (fm^2)$	$R_2\ (fm^2)$	$R_0\ (fm^2)$	$R_2\ (fm^2)$
R_o^2	18.4 ± 0.2	-0.9 ± 0.4	17.6 ± 0.2	-0.5 ± 0.3
R_s^2	19.4 ± 0.2	0.5 ± 0.3	19.6 ± 0.2	0.7 ± 0.3
R_{os}^2	-0.3 ± 0.2	0.5 ± 0.2	-0.2 ± 0.2	1.0 ± 0.2

Table 5.3: Values for sinusoidal fits (5.7) to the transverse radii.

analysis of year 2 pion data indicate a much improved signal in R_o^2 providing support for this argument [59]. Linear behavior is clearly seen in both uncorrected $\lambda(\phi)$ and $R_l^2(\phi)$.

The λ parameter for both π^- and π^+ is seen to be constant, $\lambda \sim 0.45$, as a function of ϕ. This result is in agreement with the azimuthally integrated results [3]. Deviations from $\lambda = 1$ in the fully corrected values are attributed to contributions from pions originating from long lived particles such as Λ and Ξ and particles misidentified as pions [3].

The transverse radii exhibit sinusoidal oscillations. Results of sinusoidal fits are shown in Table 5.3 and also shown as lines in the ϕ dependent plots of the transverse radii in Figs. 5.3 (π^-) and 5.4 (π^+). An initial interpretation of the ϕ dependence of the azimuthal HBT radii, assuming source dynamics are dominated by thermal motion, suggests the evolution to an out–of–plane extended particle source created in noncentral collisions. While the geometry of the emission region dominates the HBT signal, the presence of elliptic flow also contributes to the oscillations found in the azimuthal radii and can mask the magnitude of the actual source anisotropy

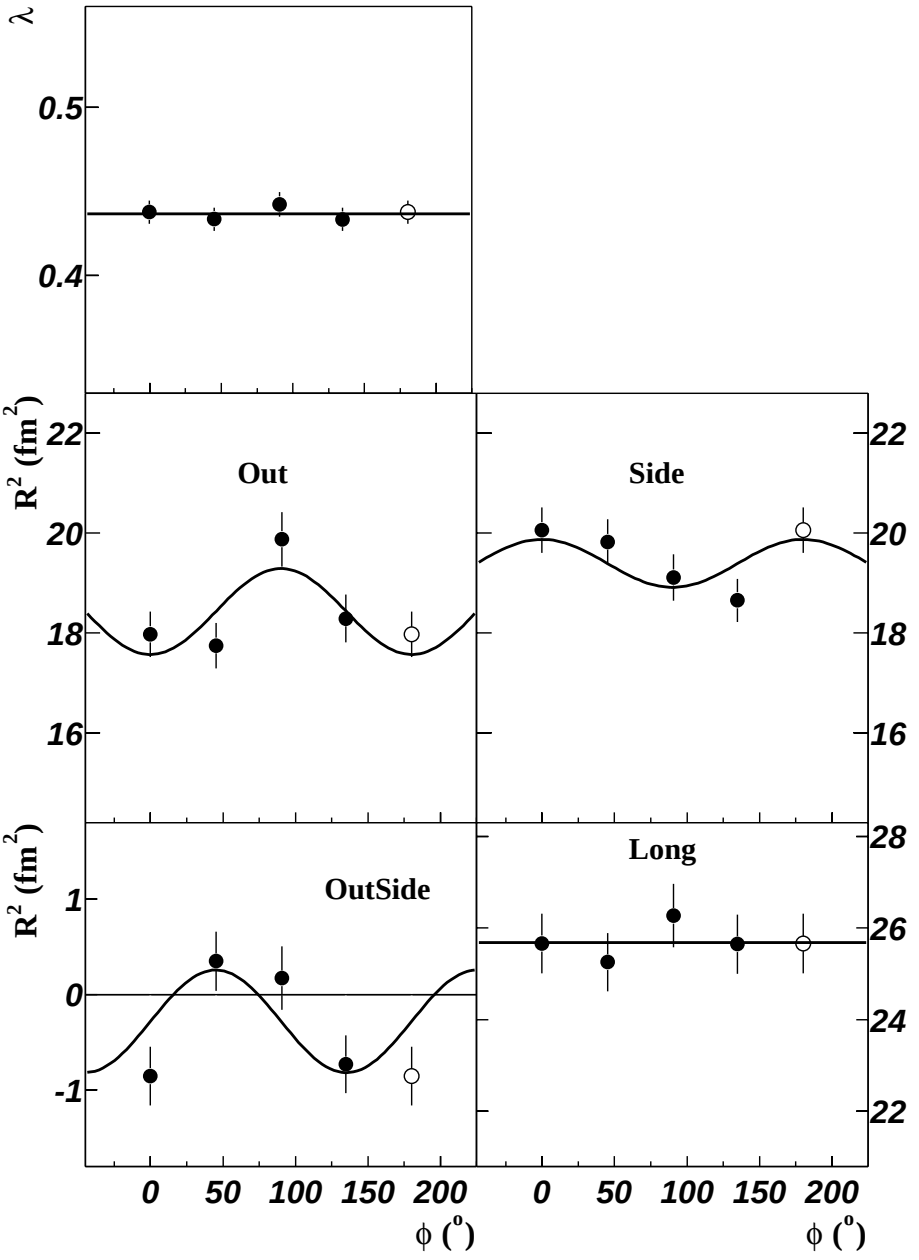

Figure 5.3: $\pi^-\pi^-$ RP HBT parameters with sinusoidal fits to transverse radii and linear fits to λ and R_l^2.

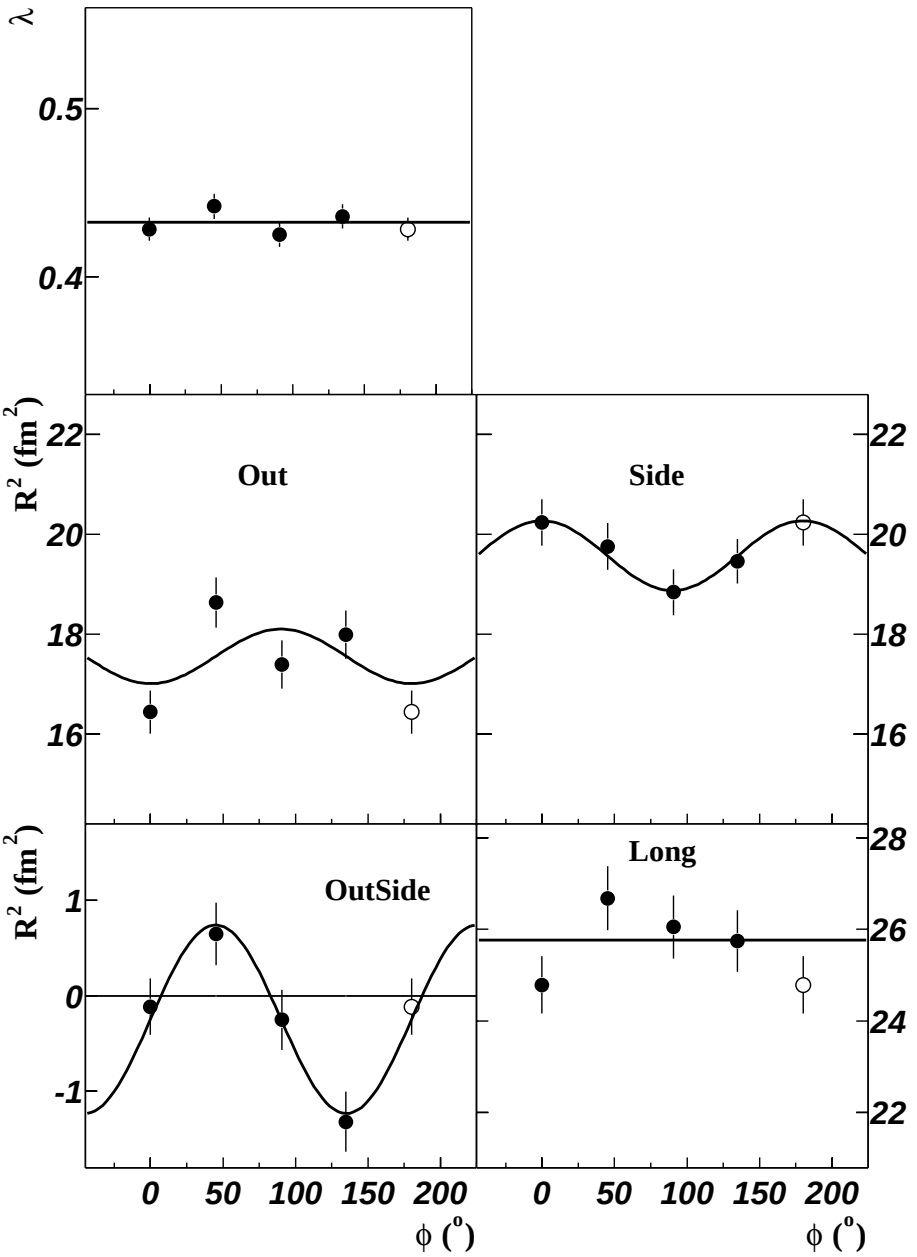

Figure 5.4: Same as Fig. 5.3 for π^+ π^+ pairs.

[60]. This will be discussed further within the context of a blast wave source model in section 5.5.

Similar to the azimuthally integrated analysis, the relative sizes of R_o^2 and R_s^2 are expected to be representative of the timescale of emission duration for low p_T particles through the ratio or difference of the radii. Strictly, this is true only when correlations between emission points and emission times and $x-p$ correlations are negligible[61]

$$R_s^2 = \langle \tilde{x_s} \rangle^2 \tag{5.3}$$

$$R_o^2 = \langle (\tilde{x_o} - \beta_T \tilde{t})^2 \rangle \tag{5.4}$$

$$R_o^2 - R_s^2 = \beta_T^2 \langle \tilde{t}^2 \rangle - 2\beta_T \langle \tilde{x_o} \tilde{t} \rangle + \langle \tilde{x_o}^2 - \tilde{x_s}^2 \rangle. \tag{5.5}$$

When one neglects the second term of (5.5) and noting that $\tilde{x_o}^2 = \tilde{x_s}^2$ for an azimuthally symmetric source with no $x-p$ correlations, the difference in the out and side can radii can be expressed as

$$R_o^2 - R_s^2 \;\; = \;\; \beta_T^2 \langle \tilde{t}^2 \rangle. \tag{5.6}$$

The ratio of R_o^2 to R_s^2 is also influenced by the amount of radial flow in the source. The presence of flow squeezes the emission region of higher p_T particles to the surface of the source volume. This reduces the depth of the emission region faster than the surface cross-section thereby reducing the relative size of the outward versus the sideward radii. The amount of collective flow at RHIC indicates the presence of a substantial amount of space–momentum correlations making relation (5.6) overly naïve requiring model comparisons to obtain predictions for the emission timescale.

The limited statistics available for the separate analyses reduced the significance of the oscillations measured for both π^- and π^+ and made any interpretations less

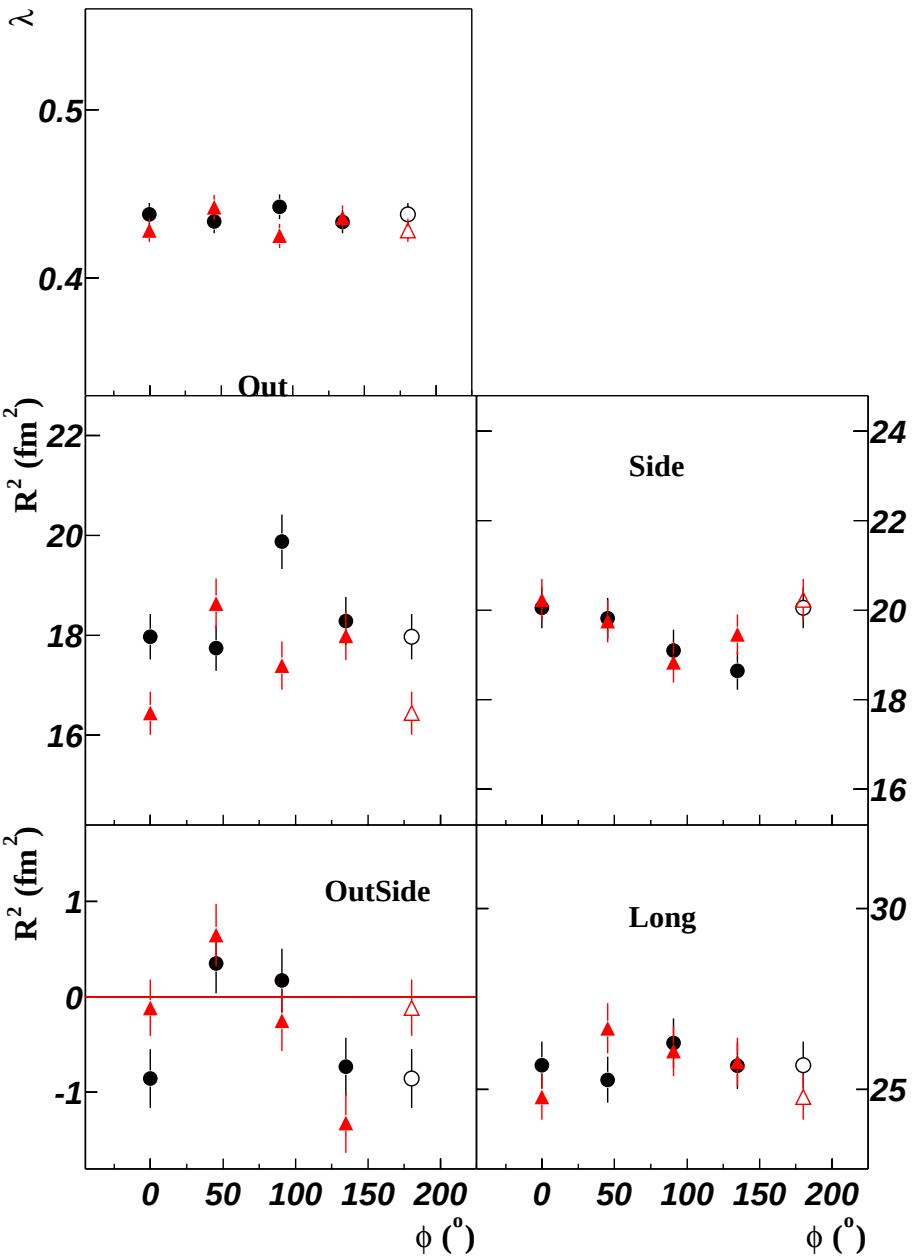

Figure 5.5: Comparison plot of π^+ π^+ (red triangles) and π^- π^- (black circles) results.

Correlation Function	χ^2/NDF
45^o	32678.9 / 32000
90^o	32259 /32000
135^o	32663.9 / 32000
180^o	32782.4 / 32000

Table 5.4: Table of χ^2 and number of degrees of freedom (NDF) for comparison of π^- and π^+ angular correlation functions.

certain. In all aspects, the results obtained from the π^- analysis is found to be roughly consistent with those obtained from π^+. Table 5.4 shows the χ^2 comparison of the π^- and π^+ correlation functions. Of note is the normalized χ^2 values which indicte good agreement between the two data sets. This is in agreement with the fitted HBT parameters. A plot of the ϕ dependence of the corrected HBT fit parameters for both π^- and π^+ is shown in Fig. 5.5. In both cases, the oscillation in R_o^2 is less than convincing. This may be due to a lack of statistics as higher statistics analysis of year 2 suggests. To alleviate this restriction, an analysis containing correlations for both π^- and π^+ are combined to produce a charged pion analysis.

5.2 ϕ Dependent HBT with Charged Pions

The symmetry of emission of charged pions allows one to combine the analyses of π^- and π^+ to reduce statistical errors in the HBT fit radii. To do this, the correlation functions formed from independent analyses for π^- and π^+ are summed. This is done by adding the real pair distribution and mixed pair distributions separately and forming the correlation function subsequently by dividing these distributions.

ϕ (^{o})	λ	R_o^2 (fm^2)	R_s^2 (fm^2)	R_l^2 (fm^2)	R_{os}^2 (fm^2)
$0 = 180$	0.433 ± 0.005	17.2 ± 0.4	20.3 ± 0.3	25.4 ± 0.5	-0.5 ± 0.2
45	0.438 ± 0.005	18.2 ± 0.4	19.9 ± 0.3	26.1 ± 0.5	0.5 ± 0.2
90	0.434 ± 0.005	18.6 ± 0.4	19.1 ± 0.3	26.3 ± 0.5	-0.0 ± 0.2
135	0.436 ± 0.005	18.2 ± 0.3	19.2 ± 0.3	25.9 ± 0.5	-1.0 ± 0.2

Table 5.5: Azimuthal dependence of the raw HBT fit parameters for a like sign charged pion analysis.

The cuts used to remove merged and split tracks and the correction procedures were identical to those of the separate analyses.

The Pratt–Bertsch projections for the summed analysis are shown in Fig. 5.6. Projections of a fit to (5.2) are included as a red line. In both cases, the projections integrate over $\pm 30 MeV/c$ in the perpendicular axes. Similar to the separate π^- and π^+ analyses, the χ^2/DOF is ~ 1 and varied from 1.032 @ 90^o to 1.050 @ 45^o and again indicate a good agreement between the experimental correlation function and the Gaussian ansatz, at the 99% confidence level [62]. The corrected fit parameters are also included in Table 5.8.

Figure 5.7 shows the dependence of the uncorrected ϕ dependence of the HBT fit values which are also shown in Table 5.5. The oscillations in the transverse radii are more clearly defined and indicate a magnitude of oscillation of approximately $2fm^2$. Linear fits are included for both λ and R_l^2. The transverse radii are fit to 2^{nd} order sinusoidal functions. The R_s^2 fit parameter, which is most closely related to geometric shape, naïvely indicates the presence of an out–of–plane extended source. To extract the true source shape, contributions from both source geometry and dynamics must be considered making the interpretation model dependent.

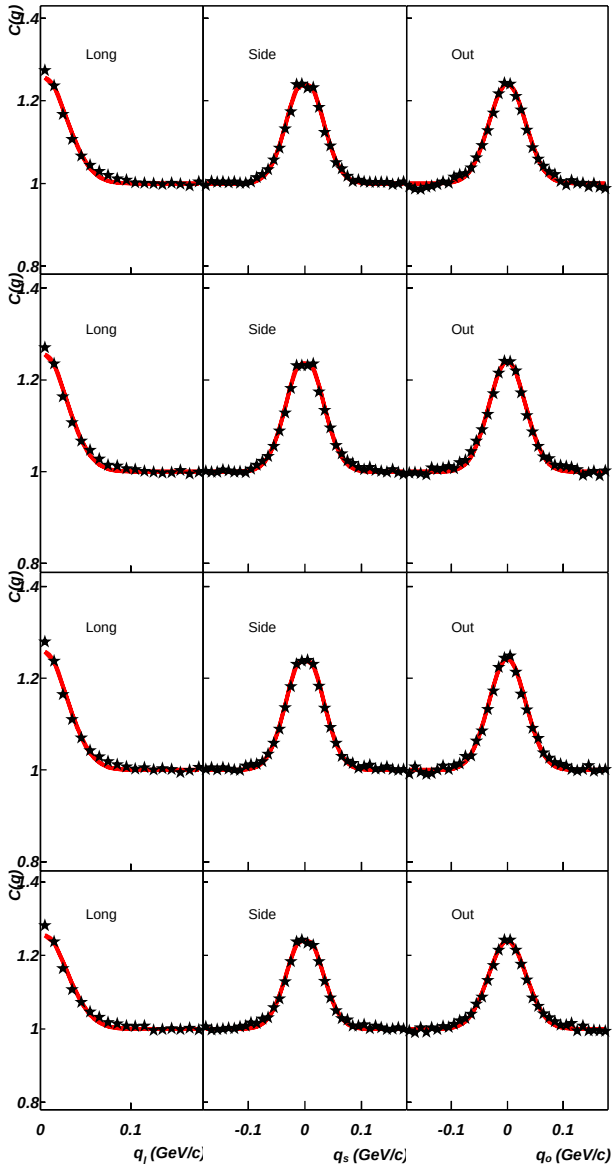

Figure 5.6: Pratt–Bertsch projections for same sign charged pion pairs emitted (top–bottom) at $\phi = 45, 90, 135, 180 \pm 22.5^o$ relative to the event plane angle. The lines are projections of fits to (5.2). Projections are integrated over $\pm 30 MeV/c$ in the perpendicular momentum components.

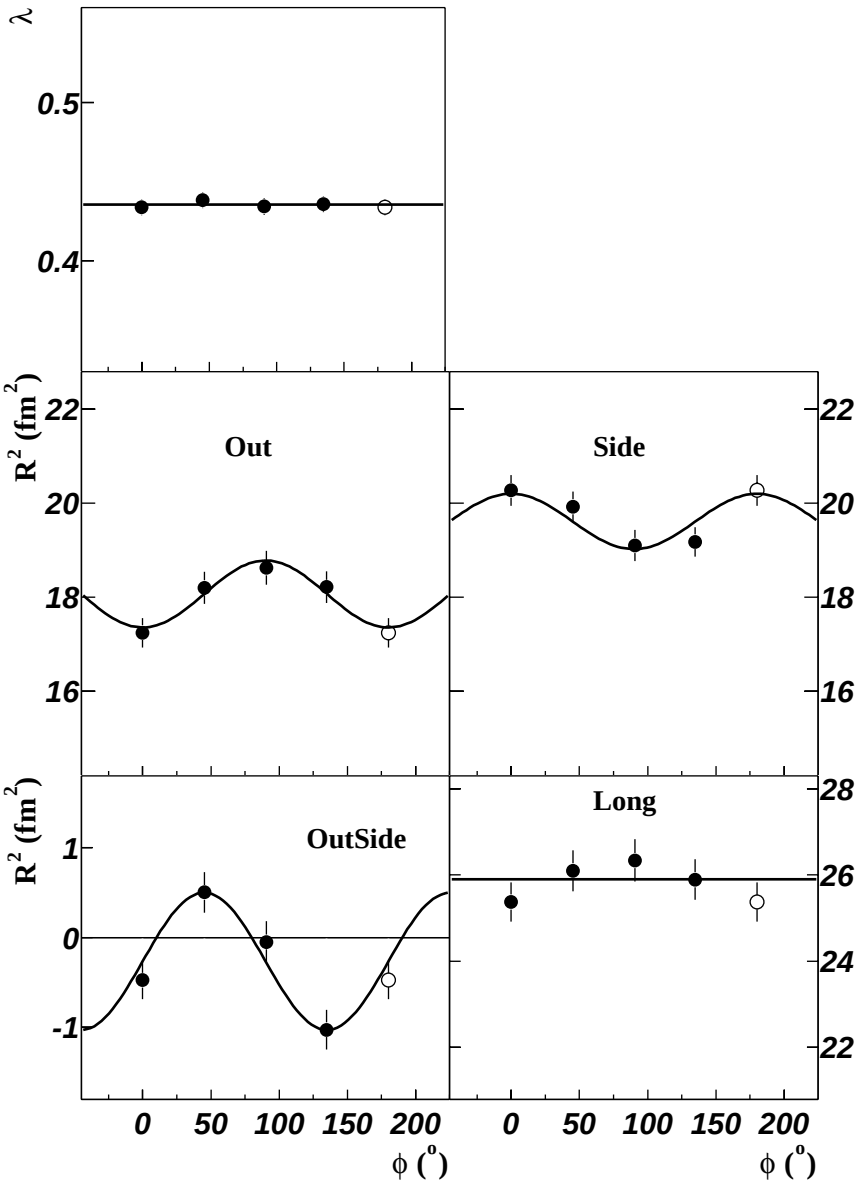

Figure 5.7: Dependence of the HBT fit parameters from (5.2) as a function of the pair emission angle relative to the event plane for a summed π^- and π^+ analysis. Linear fits to λ and R_l^2 and 2^{nd} order sinusoidal fits to the transverse radii are included.

5.3 Data Corrections

5.3.1 Track Merging

The average separation cut used to remove effects due to track merging introduced a systematic reduction to the diagonal HBT fit parameters, λ, R_o^2, R_s^2, and R_l^2. Simulation studies for the azimuthally integrated analysis indicated the cause of the reduction as due to non–Gaussianess in the correlation function [3]. A double Gaussian source simulation was used to estimate the reduction as described in Section 4.4.2 and shown in Fig. 4.18. A linear fit to the slope of the fit parameters versus separation cut showed λ to be reduced by $\sim 14\%$ while the radii were reduced by 16, 11, and 8% for R_o^2, R_s^2, and R_l^2 respectively. This is a similar reduction to that found in [3].

5.3.2 Event Plane Resolution

Finite event plane resolution reduces the magnitude of the measure oscillations in the HBT radii as a function of ϕ. Two methods to correct the data for this effect were studied. The first method which is pictorially intuitive was first developed yet is technically incorrect. It is included here due to the work that was devoted to it and to serve as a reference to the correction method used for data that has been presented at various conferences. This method applies the correction to the fitted radii themselves to increase the magnitude of oscillation in the transverse HBT radii only. The second correction method is applied to the correlation functions, the numerator and denominator separately. Finite event plane resolution distorts the ϕ dependence of the relative momenta reducing the oscillations in the HBT radii by smearing the entries in the numerator and denominator histograms. The second and

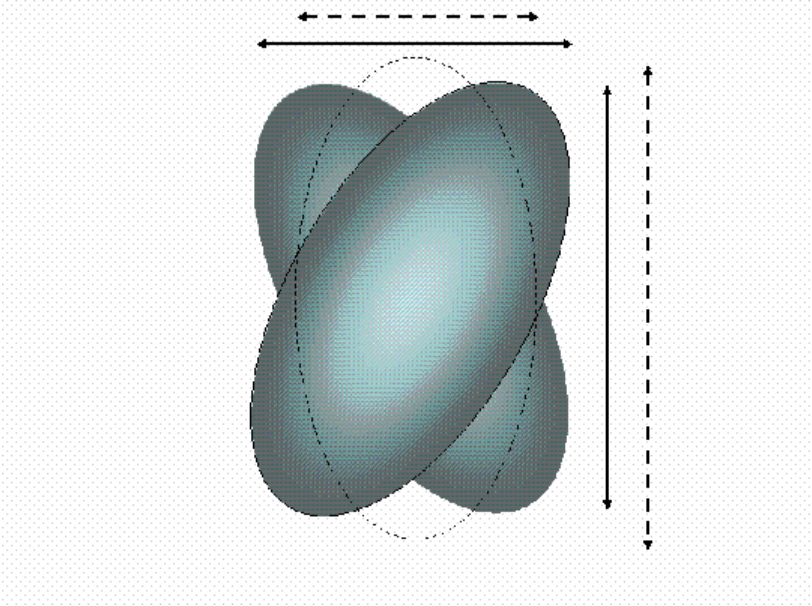

Figure 5.8: Diagram showing the effect of finite event plane resolution on the measured transverse HBT radii as assumed in the intuitive method. The dotted arrows represent the actual widths of the source while the solid arrows indicate the widths measured through experiment.

correct method to account for finite event plane resolution corrects the distortions in the histograms themselves prior to the Gaussian fits.

Intuitive Radii Correction

Fig. 5.8 shows the pictorial representation of the assumed effect of finite event plane resolution to the ϕ dependent source radii. In this method, it is assumed the oscillations in the radii themselves are reduced from the imperfect resolution of the event plane by forming a superposition of sources misaligned to the measured event plane. Note that this method treats the longitudinal radius R_l^2 as being ϕ independent. Correction method 2 (see Section 5.3.2) will show this not to be a valid

ϕ (^{o})	λ	R_o^2 (fm^2)	R_s^2 (fm^2)	R_l^2 (fm^2)	R_{os}^2 (fm^2)
$0 = 180$	0.503 ± 0.007	20.6 ± 0.8	22.6 ± 0.8	27.8 ± 0.7	-1.3 ± 0.6
45	0.498 ± 0.007	20.2 ± 0.8	22.2 ± 0.8	27.4 ± 0.6	0.8 ± 0.6
90	0.507 ± 0.007	24.0 ± 1.0	20.9 ± 0.8	28.4 ± 0.8	0.5 ± 0.6
135	0.498 ± 0.007	21.1 ± 0.9	20.1 ± 0.8	27.8 ± 0.7	-1.1 ± 0.6

Table 5.6: Azimuthal dependence of the π^- π^- HBT fit parameters corrected for both the separation systematic and finite event plane resolution.

assumption. A two step process is used to correct the radii for this effect. First the ϕ dependence of the radii are fit to sinusoidal functions

$$R_{o,s}^2 = R_0 + R_2 \cos(2\phi) \tag{5.7}$$

$$R_{os}^2 = R_0 + R_2 \sin(2\phi). \tag{5.8}$$

The transverse radii are then scaled by the event plane resolution factor, $\langle \cos(2(\psi - \psi')) \rangle$ described in Section 4.6.1

$$R'_{o,s,os}[\phi_i] = R_0 + \frac{1}{\langle \cos(2(\psi - \psi')) \rangle} (R_{o,s,os}[\phi_i] - R_0). \tag{5.9}$$

This method increases the magnitude of the transverse oscillations while retaining the mean value by which they oscillate. The resolution factor for the minimum–bias event collection used in this analysis was measured to be approximately 0.56 corresponding to a angular resolution of $\sim 28^o$. The azimuthal dependence of the corrected HBT radii are shown in Tables 5.6, 5.7, and 5.8.

Fig. 5.9 shows the charged pion summed analysis HBT radii. The raw data are shown as black circles with the corrected radii for separation systematic (green squares) and with the radii resolution correction (red triangles). Also included is a hydrodynamic model parameterization calculation for the transverse radii which is

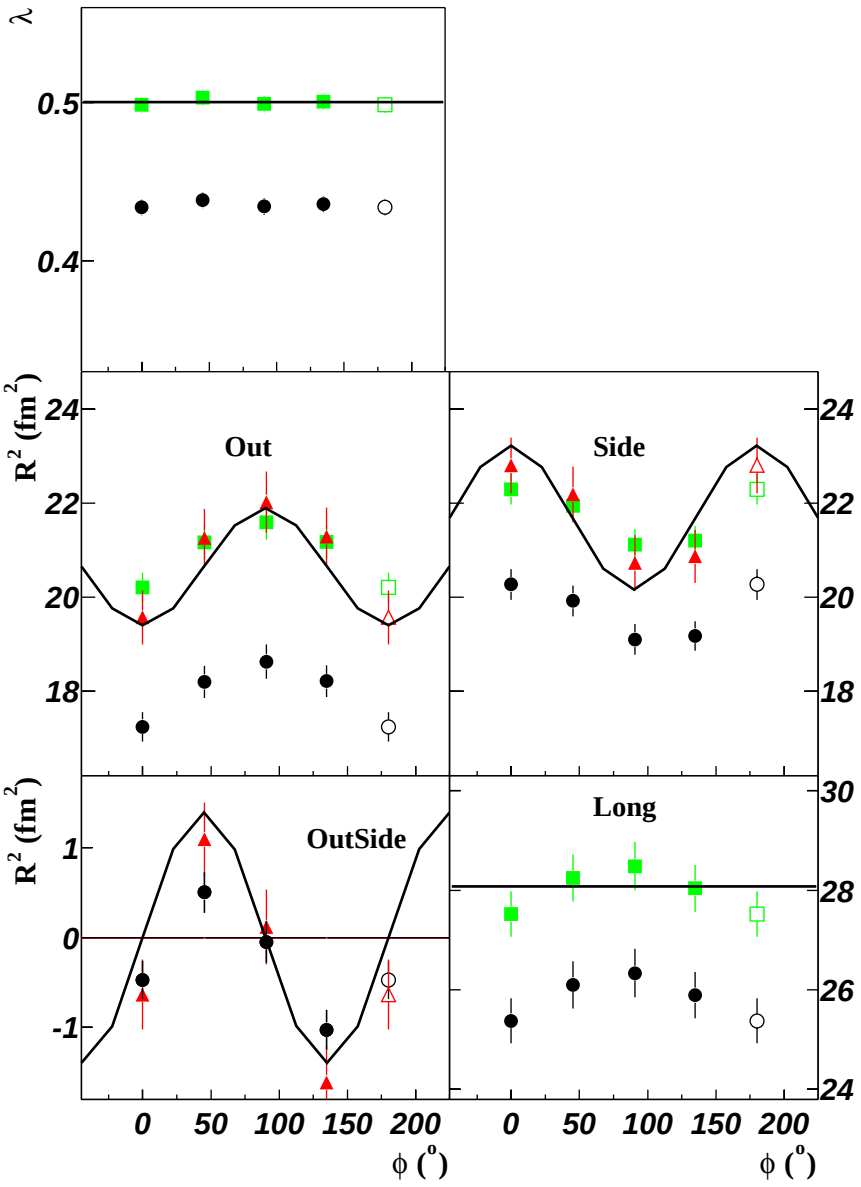

Figure 5.9: Dependence of the HBT fit parameters from (5.2) as a function of the pair emission angle relative to the event plane for a summed π^- and π^+ analysis. The black circles are the raw data while the green squares are the data corrected for the systematic reduction in fit parameters due to the track merging cut. The red triangles are the data after applying a (parameter) correction for event plane resolution in addition to the merging correction. The lines represent the results of a blast wave calculation using the parameters in Table 5.10.

ϕ (^{o})	λ	R_o^2 (fm^2)	R_s^2 (fm^2)	R_l^2 (fm^2)	R_{os}^2 (fm^2)
$0 = 180$	0.493 ± 0.007	18.6 ± 0.8	22.8 ± 0.8	26.9 ± 0.6	-0.0 ± 0.5
45	0.507 ± 0.007	22.4 ± 0.9	21.9 ± 0.8	28.8 ± 0.7	1.3 ± 0.6
90	0.490 ± 0.007	20.2 ± 0.9	20.3 ± 0.8	28.2 ± 0.7	-0.3 ± 0.6
135	0.501 ± 0.007	21.3 ± 0.9	21.4 ± 0.8	27.9 ± 0.7	-2.1 ± 0.6

Table 5.7: Same as Table 5.6 for π^+ π^+ pairs.

ϕ (^{o})	λ	R_o^2 (fm^2)	R_s^2 (fm^2)	R_l^2 (fm^2)	R_{os}^2 (fm^2)
$0 = 180$	0.499 ± 0.005	19.6 ± 0.6	22.8 ± 0.6	27.5 ± 0.5	-0.6 ± 0.4
45	0.503 ± 0.005	21.3 ± 0.6	22.2 ± 0.6	28.2 ± 0.5	1.1 ± 0.4
90	0.499 ± 0.005	22.0 ± 0.7	20.7 ± 0.6	28.5 ± 0.5	0.1 ± 0.4
135	0.500 ± 0.005	21.3 ± 0.6	20.9 ± 0.6	28.0 ± 0.5	-1.6 ± 0.4

Table 5.8: Same as Table 5.6 for summed π^+ π^+ and π^- π^-.

described in Section 5.5. The resolution correction is seen to approximately double the magnitude of oscillation in the 3 transverse radii.

Histogram Correction

While the previously described event plane resolution correction procedure is intuitive and can be understood easily graphically, it is technically incorrect. The smearing of the correlation function by imperfect event plane reconstruction is exprected to diminish the amplitudes of the oscillations in the transvserse radii, but the effect it has on a correlation function is truely present in the individual bins of the separate histograms from the real and mixed pair distributions. The distribution of

reconstructed event planes follows the form[39]

$$p(\phi_m - \phi_R) = \int \frac{v'_m dv'_m}{2\pi\sigma^2} \times \exp\Big(- \frac{v_m^2 + v'^2_m - 2v_m v'_m \cos[m(\phi_m - \phi_R)]}{2\sigma^2}\Big), \quad (5.10)$$

where σ is a factor dependent on the event multiplicity. The correlations are also distorted from finite binning of the correlation functions in ϕ, reducing the amplitudes of oscillations in the radii through an additional distribution,

$$f_\Delta(\phi - \Phi) = \frac{1}{\Delta}\ \theta(\phi - \Phi + \frac{1}{2}\Delta)\ \theta(\frac{1}{2}\Delta - \phi + \Phi), \quad (5.11)$$

where Δ is the angular width of the bins.

A model independent correction method was introduced in [58] to account for both finite event plane resolution and binning of the correlation functions in finite ϕ bins. In the construction of the correction method, the correlation function histograms (both numerator and denominator) are expanded into Fourier series

$$\begin{aligned} H(\mathbf{q}, \Phi - \psi_m) &= H_0^{exp}(\mathbf{q}) + 2\sum_{n=1}^{n_{bin}} [H_{c,n}^{exp}(\mathbf{q}) \cos(n(\Phi - \psi_m)) + \\ &\quad + H_{s,n}^{exp}(\mathbf{q}) \sin(n(\Phi - \psi_m))]. \end{aligned} \quad (5.12)$$

Here, $H_{c,n}^{exp}$ is used to represent either the numerator (N) or denominator (D) Fourier components of the histogram expansion obtained from

$$H_{c,n}^{exp}(\mathbf{q}) = \frac{1}{n_{bin}} \sum_{i=1}^{n_{bin}} H_{exp}(\mathbf{q}, \Phi_i) \cos(n\Phi_i) \quad (5.13)$$

and

$$H_{s,n}^{exp}(\mathbf{q}) = \frac{1}{n_{bin}} \sum_{i=1}^{n_{bin}} H_{exp}(\mathbf{q}, \Phi_i) \sin(n\Phi_i). \quad (5.14)$$

This is similar to the expansion of the momenta distribution used to calculate the flow coefficients, v_n, from (2.38).

By folding the Fourier expansions with the effects of event plane binning and resolution one can obtain the histogram correction:

$$H(\mathbf{q},\Phi_i) = H_{exp}(\mathbf{q},\Phi_i) + 2\sum_{n=1}^{n_{bin}} \zeta_{n,m}(\Delta)[H_{c,n}^{exp}(\mathbf{q})\cos(n\Phi_i) + \\ + H_{s,n}^{exp}(\mathbf{q})\sin(n\Phi_i)]. \tag{5.15}$$

The $\zeta_{m,n}$ coefficients contain both binning and resolution effects

$$\zeta_{n,m}(\Delta) = \frac{n\Delta/2}{\sin(n\Delta/2)\langle\cos(n(\psi_m - \psi_R))\rangle_p} - 1, \tag{5.16}$$

where, $\langle\cos(n(\psi_m - \psi_R))\rangle$ is the resolution factor obtained from the sub–events. This is identical to the correction procedure for elliptic flow, but in this case, the correction is applied for *every* $\vec{q}$ *and* ϕ *bin* separately for the numerator and denominator. In the case of binned data points, only Fourier components $n \leq n_{\phi bin}$ contribute [58].

The results of applying the histogram resolution correction to the data is shown in Fig. 5.10. The fit parameters are also shown in Table 5.9. In comparison with the radial correction discussed in Section 5.3.2, we see that the correction values obtained through the histogram bin content method is approximately the same as the fit parameter correction. The blast wave parameterization used to describe the transverse radial oscillation continues to roughly agree with the data. This parameterization makes no prediction for the structure of the ϕ dependence of the longitudinal radius although it is clear that an oscillation is present in the corrected $R_l^2(\phi)$.

5.4 Correction Uncertainties

Uncertainties in the correction associated with both the separation cut and the event plane resolution introduce systematic error to the fully corrected radii. As with the azimuthally integrated analysis, the error due to the separation cut was

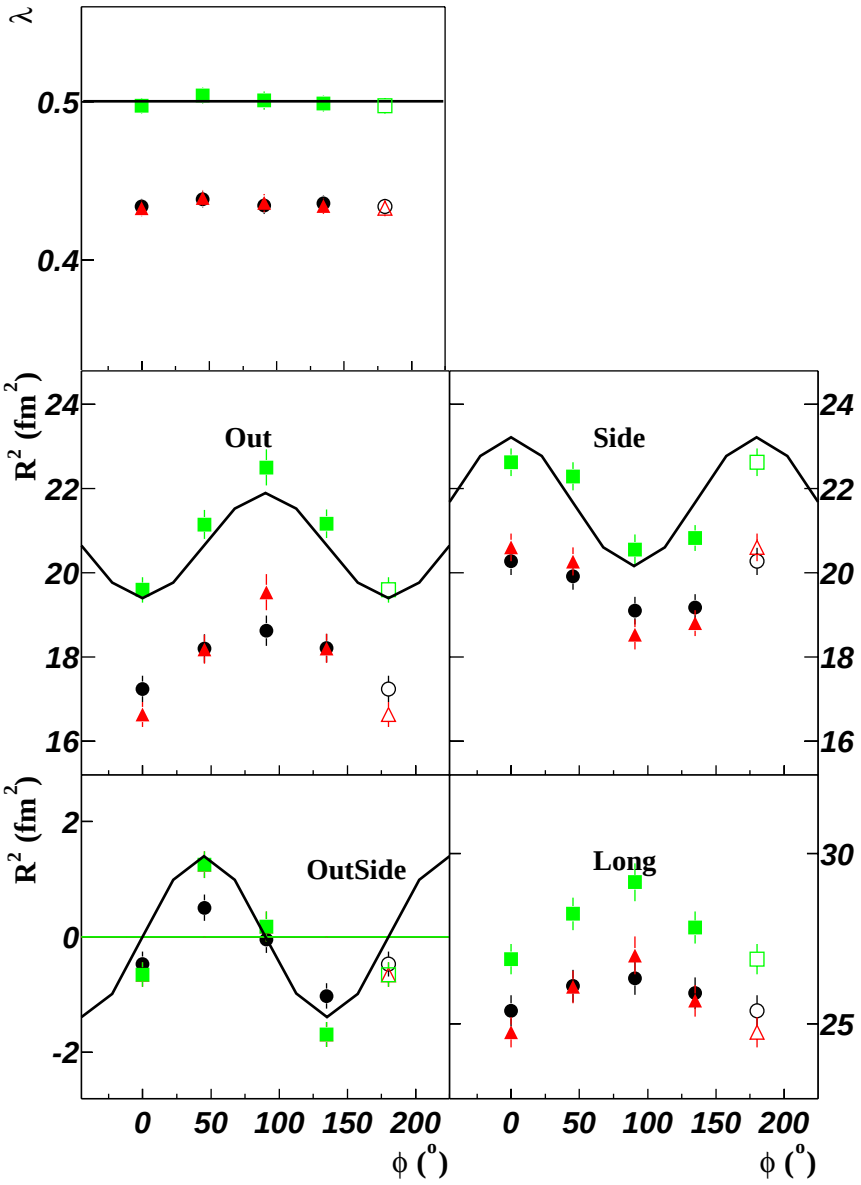

Figure 5.10: The ϕ dependent HBT radii: raw fit values are shown as black circles while event plane resolution corrected (histogram bin content method) values are shown as red triangles and additionally corrected radii for the separation systematic are shown as green squares. A comparison to the transverse HBT radii from the blast wave hydrodynamic model are included as black lines in R_o^2, R_s^2, and R_{os}^2 while both λ and R_l^2 are fit to linear functions.

ϕ (^{o})	λ	R_o^2 (fm^2)	R_s^2 (fm^2)	R_l^2 (fm^2)	R_{os}^2 (fm^2)
$0 = 180$	0.433 ± 0.005	16.6 ± 0.3	20.6 ± 0.3	24.7 ± 0.4	-0.7 ± 0.2
45	0.439 ± 0.005	18.2 ± 0.3	20.3 ± 0.3	26.0 ± 0.5	1.2 ± 0.2
90	0.436 ± 0.006	19.5 ± 0.4	18.5 ± 0.4	27.0 ± 0.6	0.2 ± 0.3
135	0.434 ± 0.005	18.2 ± 0.3	18.8 ± 0.3	25.7 ± 0.5	-1.7 ± 0.2

Table 5.9: ϕ dependent HBT fit parameters corrected for event plane resolution using the histogram correction method.

estimated to be equal to the correction itself, between $8-16\%$ for λ, R_l^2, R_o^2, and R_s^2. An additional source of systematic error is introduced from the Coulomb correction. By varying the source correction radius, a variance of $\approx 10\%$ in the diagonal fit parameters is found while the cross term radius, R_{os}^2, was little changed.

5.5 Towards a consistent description of the source

STAR was envisioned as a flexible detector designed to provide a means to correlate the mesurement of many observables to better characterize the freeze–out configuration. By combining the measurements of several quantities, one can take advantage of the sensitivities of each observable to various source characteristics to obtain a more detailed picture of the evolution of the emission region. This also provides more constraints on dynamic models of the collision. Hydrodynamic models are seen to well reproduce the charged particle spectra and v_2 as a function of $p_T \lesssim 1GeV/c$ measured at RHIC by STAR and PHENIX [63]. Comparisons with both RQMD and hydrodynamic models indicate that although neither is successful at predicting the size of the HBT radii they both reproduce the phases and magnitudes of the oscillations in the transverse HBT radii shown in Figs 5.11 and 5.12. From the figures one

notices the discrepancy between the sideward radii where the both model calculations predict a squared radius $\sim 10fm^2$ whereas the data give sidward radii $\sim 20fm^2$. The outward radii in both model agree reasonably well in magnitude, but the relative sizes of out and side are suggestive of very different dynamical properties between the models and the data. In [2], the effects of including a dilute rescattering phase to a hydrodynamic simulation on the source geometry was investigated. To measure the source anisotropy, they included a s_2' parameter,

$$s_2' = \left\langle \frac{x^2 - y^2}{x^2 + y^2} \right\rangle. \tag{5.17}$$

The results show that the inclusion of the dilute rescattering from RQMD lengthens the lifetime of the source. This allows the in–plane elliptic flow produced during the early hydrodynamic phase to push the initial spatial anisotropy from out–of–plane extended, $s_2' \sim -0.015$, to a final in–plane extended source, $s_2' \sim 0.015$. This is important, since late stage hadronic interactions actually worsen the "RHIC HBT Puzzle" [63]. The Teaney/Shuryak calculation provides a qualitative feature (in–plane or out–of–plane shape) to study in the data, which reflects the late hadronic stage.

In [12], the identified particle $v_2(p_T)$ STAR results were compared to a hydrodynamic–inspired circular blast wave parametrization first introduced by Siemens and Rasmussen in the late 70's [64]. This parameterization provides a convenient formalism to describe the freeze–out configuration of the emission region formed in the heavy ion collisions. It also has the flexibilty to be used to describe a variety of obserables each of which is sensitive to different parameters of the model.

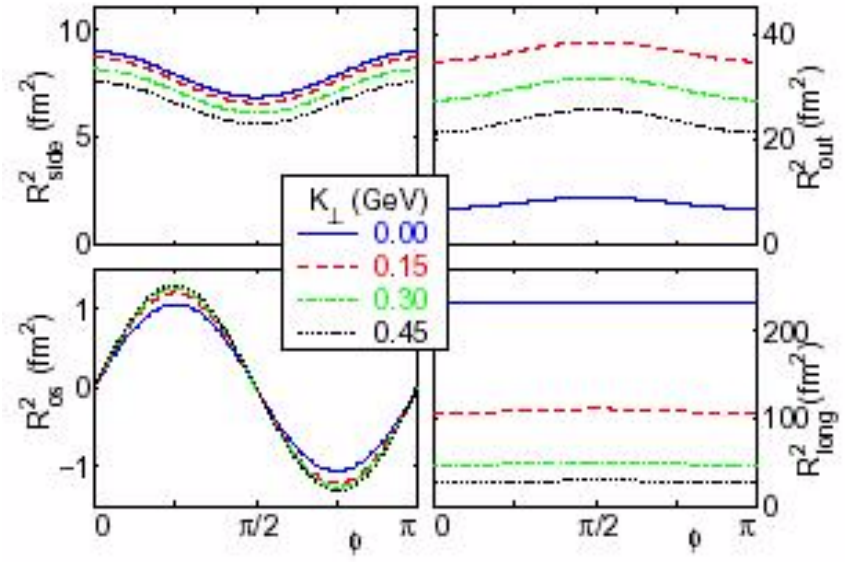

Figure 5.11: Azimuthal oscillations of the HBT radii at $Y = 0$ for $b = 7fm$ Au + Au collisions at $\sqrt{s_{NN}} = 130GeV$ from hydrodynamic simulation [11].

In the Boltzmann approximation, the freeze-out spectrum can be simplified to the form,[65]

$$\frac{d^4N}{dy\ dm_T^2\ d\phi_p} \sim \int d\phi_b\ K_1(\beta(\phi_b))\ e^{\alpha(\phi_b)\cos(\phi_b-\phi_p)}. \tag{5.18}$$

This provides an analytic expression for the elliptic flow

$$v_2(p_T) = \frac{\int d\phi_b\ \cos(2\phi_b)\ I_2(\alpha(\phi_b))K_1(\beta(\phi_b))}{\int d\phi_b\ I_0(\alpha(\phi_b))K_1(\beta(\phi_b))}. \tag{5.19}$$

In the above equations, ϕ_b is the flow boost angle perpendicular to the freeze–out surface, $\alpha(\phi) = (p_T/T)\sinh(\rho(\phi))$, and $\beta(\phi) = (m_T/T)\cosh(\rho(\phi))$ where $\rho(\phi) = \rho_0 + \rho_2\cos(2\phi)$ represents the radial flow which may oscillate with ϕ. Fig. 5.13 shows the STAR $v_2(p_T)$ for identified pions, kaons, and protons. The dotted lines in Fig. 5.13 are fits to (5.19). An additional spatial anisotropy of the form $(1 + s_2\cos(2\phi_b))$ was

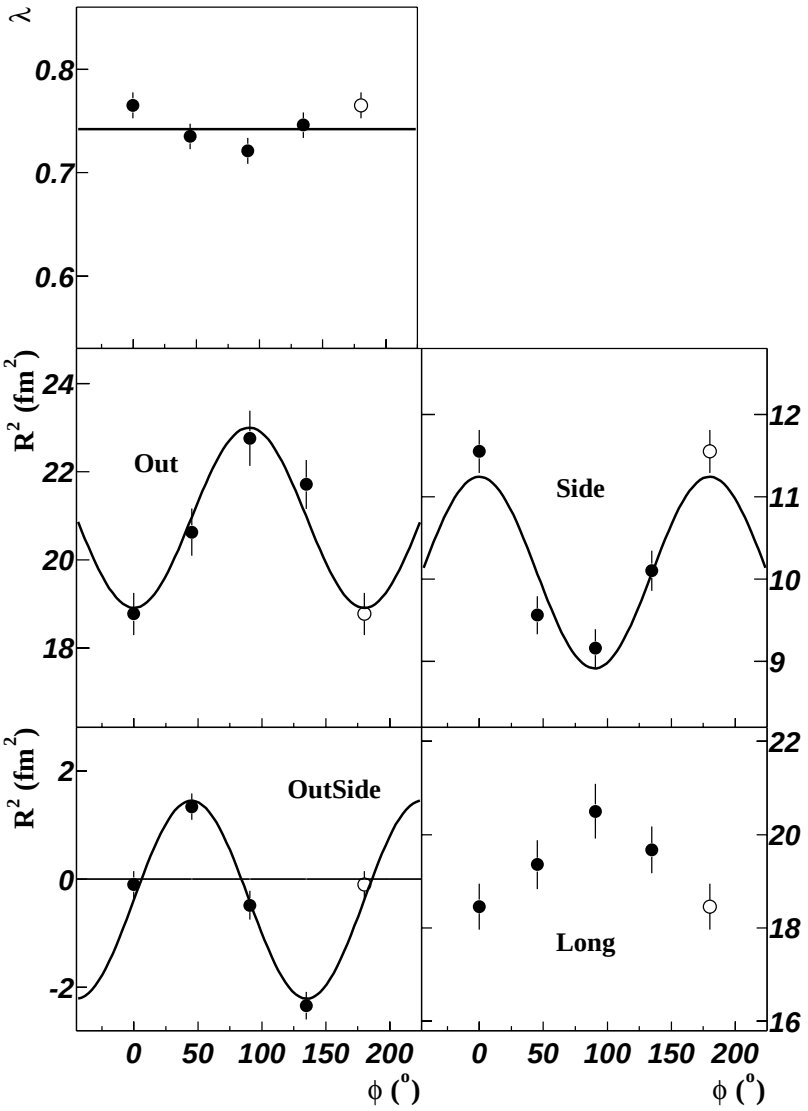

Figure 5.12: Azimuthal dependence of the pion HBT radii from a RQMD simulation at RHIC energies. Also included are linear fits to $\lambda(\phi)$ and $R_l^2(\phi)$ while the transverse radii are fit to second order sinusoidal functions (see (5.7)).

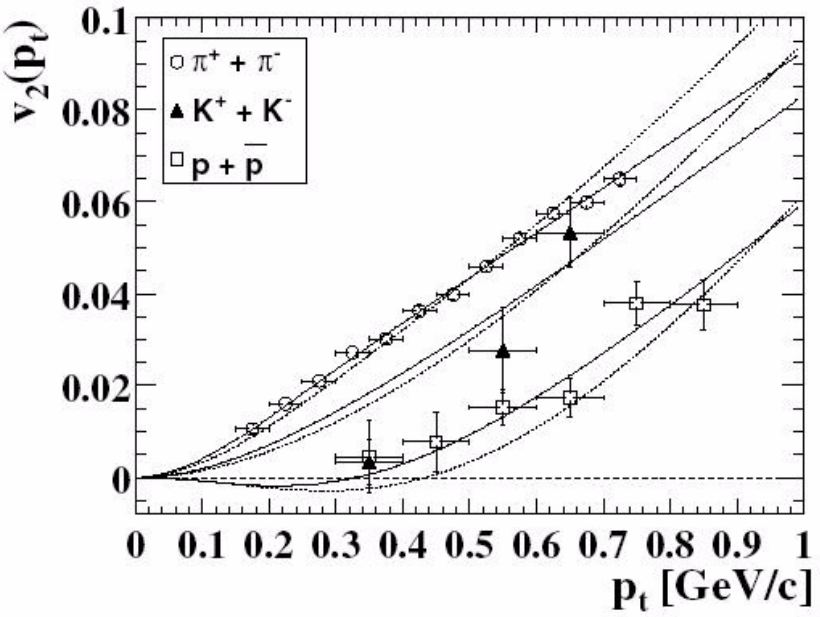

Figure 5.13: Differential elliptic flow for pions, kaons, and protons + antiprotons for minimum–bias events. The solid lines show the fit with the modified blast wave model, and the dotted lines are fits with the unmodified model.[12]

$T_f(MeV)$	ρ_0	ρ_2	s_2	$R_y(fm)$	$\tau(fm/c)$
135 ± 19	0.58 ± 0.03	0.09 ± 0.02	0	—	—
101 ± 24	0.61 ± 0.05	0.04 ± 0.01	0.04 ± 0.01	—	—
100	0.61	0.04	0.04	11.7	2.2

Table 5.10: Blast wave fit parameters for the STAR $v_2(p_T)$ results without a spatial anisotropy (top row) and with (middle row). Also, the parameters used to describe the $R^2_{i,j}(\phi)$ seen in Figs. 5.15 and 5.16 are shown in the bottom row.

introduced to (5.19) and also fit to the data seen as solid lines in Fig. 5.13.

$$v_2(p_T) \;=\; \frac{\int d\phi_b \;\cos(2\phi_b)\; I_2(\alpha(\phi_b))K_1(\beta(\phi_b))(1+2s_2\cos(2\phi_b))}{\int d\phi_b \; I_0(\alpha(\phi_b))K_1(\beta(\phi_b))(1+2s_2\cos(2\phi_b))}. \tag{5.20}$$

With the inclusion of a spatial anisotropy, the now modified blast wave is able to reproduce the STAR $v_2(p_T)$ very well. Table 5.10 shows the fit values for the two cases of the blast wave [12].

The improvement of the fit to the Huovinen model when a nonzero s_2 was included provided a strong indication of the presence of some type of spatial anisotropy. While the nonzero s_2 provides evidence suggesting a spatially anisotropic source, it is ambiguous as to its character. Examination of (5.20) reveals that $s_2 > 0$ indicates more source elements emitting in–plane. Note that $\rho_a > 0$ means the in–plane sources have stronger boost. Both $s_2 > 0$ and $\rho_a > 0$ produce/contribute to the elliptic flow signal $v_2(p_T)$, but in different ways. There are several ways to modify the source function to account for more source elements emitting in–plane. We consider two limiting cases:

1. The transverse source remains circular, but has a higher density in–plane

2. The source density is constant, but the source shape is extended out–of–plane

shown in Fig. 5.14 The original construction of the freeze–out geometry consisted of

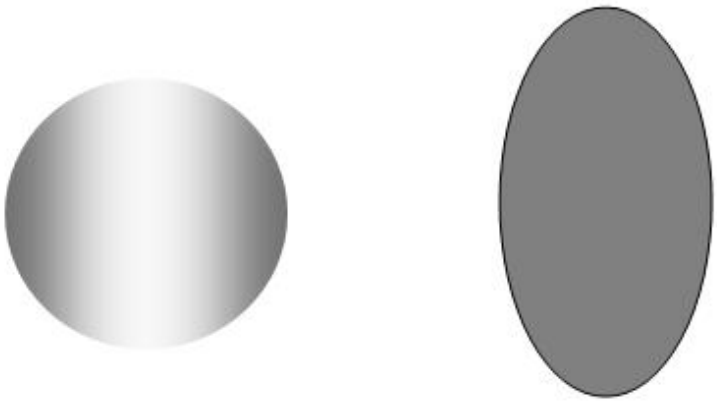

Figure 5.14: Example diagrams of the two limiting cases of the interpretation of the s_2 parameter. A modulated source density within a circular emission region is shown to the left while a source characterized by uniform density, but extended out–of–plane, is shown to the right.

Parameter	Symbol	Spectra	Elliptic Flow (v_2)	$R_{ij}(p_T, \phi)$
Temperature	T	Yes	Yes	Yes
Radial flow	ρ_0	Yes	Yes	Yes
Flow anisotrpy	ρ_a		Yes	Yes
Coordinate anisotropy	s_2		Yes	Yes
Interpretation of s_2				Yes
Source size	R_{ij}			Yes
Particle emission duration	τ			Yes

Table 5.11: A table indicating the sensitivity to each of the blast wave parameters of various observables from STAR.

a circular annulus, and so a natural interpretation of the s_2 parameter would be as a modulation of the particle density in the circular source. In this case, a positive s_2 would indicate an increase on the number of sources in–plane, while a negative s_2 would indicate a larger number of sources out–of–plane. However, another possible interpretation of the spatial anisotropy is a change in the geometric extension of a homogeneous source. The elliptic flow boost is normal to the freeze–out surface indicating that, within this interpretation, a positive s_2 represents a source extended out–of–plane. Table 5.11 shows the dependencies of the particle spectra, elliptic flow, and ϕ dependent HBT.

The particle spectra are related to the phase space density function by

$$E_p \frac{d^3 N_a}{d^3 \vec{p}} = \int d^4x \; S_a(x, p). \tag{5.21}$$

From (5.18), one finds a blast wave source function

$$S(\mathbf{x}, \mathbf{p}) = K_1(\beta(\phi_b)) e^{\alpha(\phi_b)\cos(\phi_b - \phi_p)} \delta(r - R) \tag{5.22}$$

where $\delta(r-R)$ provides the shell structure of the annulus of radius R. By modifying (5.22) to be a continuous function in coordinate space, the implications of the two limiting cases of the s_2 parameter on the transverse HBT radii can be calculated within the blast wave parameterization. The modulated source density can be included by replacing the delta function in (5.22) with $(1+s_2\frac{r}{R}\cos(2\phi_b))\Theta(R-r)$ while the elliptical source function can be modeled with $\Theta(1-\sqrt{y^2-\eta^2x^2}/R_y)$, where $\eta = R_y/R_x$ and

$$\Theta(x) = \begin{cases} 0 & \text{if } x < 0 \\ 1 & \text{if } x > 0. \end{cases} \tag{5.23}$$

This results in modified blast wave source functions for the two cases (modulated density and elliptical source shape)

$$S(\mathbf{x},\mathbf{p}) = K_1(\beta(\phi_b))e^{\alpha(\phi_b)\cos(\phi_b-\phi_p)}(1+s_2\frac{r}{R}\cos(2\phi_b))\Theta(R-r), \tag{5.24}$$

$$S(\mathbf{x},\mathbf{p}) = K_1(\beta(\phi_b))e^{\alpha(\phi_b)\cos(\phi_b-\phi_p)}\Theta(1-\sqrt{y^2-\eta^2x^2}/R_y). \tag{5.25}$$

The time dependence of the particle emission is included through a Gaussian distribution $\exp(-t/(2\tau))$ to produce an emission time–scale of τ. To remove any discontinuities in the momentum boost at $r=0$, a gradient r/R is applied to the flow field

$$\rho(\phi) = \frac{r}{R}(\rho_0 + \rho_a\cos(2\phi)). \tag{5.26}$$

The s_2 parameter from the blast wave fit to the v_2 is different from the s_2' used in [2] and is related to η by [60]

$$s_2 \approx \frac{1}{2}\frac{\eta^3-1}{\eta^3+1}. \tag{5.27}$$

The ϕ dependence of the transverse HBT radii are now calculated by combining (2.16) and (2.33):

$$\begin{aligned}
\langle x\rangle(\phi_p, p_T) &= \frac{\int r\ dr\ d\phi\ dt\ (r\cos(\phi))\ S(r,\mathbf{p})}{\int r\ dr\ d\phi\ dt\ S(r,\mathbf{p})} \\
\langle y\rangle(\phi_p, p_T) &= \frac{\int r\ dr\ d\phi\ dt\ (r\sin(\phi))\ S(r,\mathbf{p})}{\int r\ dr\ d\phi\ dt\ S(r,\mathbf{p})} \\
\langle \tilde{x}^2\rangle(\phi_p, p_T) &= \frac{\int r\ dr\ d\phi\ dt\ (r\cos(\phi))^2\ S(r,\mathbf{p})}{\int r\ dr\ d\phi\ dt\ S(r,\mathbf{p})} - \langle x\rangle^2 \\
\langle \tilde{y}^2\rangle(\phi_p, p_T) &= \frac{\int r\ dr\ d\phi\ dt\ (r\sin(\phi))^2\ S(r,\mathbf{p})}{\int r\ dr\ d\phi\ dt\ S(r,\mathbf{p})} - \langle y\rangle^2 \\
\langle \tilde{x}\tilde{y}\rangle(\phi_p, p_T) &= \frac{\int r\ dr\ d\phi\ dt\ (r\cos(\phi))(r\sin(\phi))\ S(r,\mathbf{p})}{\int r\ dr\ d\phi\ dt\ S(r,\mathbf{p})} - \langle x\rangle\langle y\rangle
\end{aligned} \tag{5.28}$$

and

$$\begin{aligned}
R_o^2(\phi_p, p_T) &= \langle \tilde{x}^2\rangle \sin^2(\phi_p) + \langle \tilde{y}^2\rangle \cos^2(\phi_p) - \langle \tilde{x}\tilde{y}\rangle \sin(2\phi_p) \\
R_s^2(\phi_p, p_T) &= \langle \tilde{x}^2\rangle \cos^2(\phi_p) + \langle \tilde{y}^2\rangle \sin^2(\phi_p) + \langle \tilde{x}\tilde{y}\rangle \sin(2\phi_p) \\
R_{os}^2(\phi_p, p_T) &= \langle \tilde{x}\tilde{y}\rangle \cos(2\phi_p) + \frac{1}{2}(\langle \tilde{y}^2\rangle - \langle \tilde{x}^2\rangle)\sin(2\phi_p)
\end{aligned} \tag{5.29}$$

The ϕ dependence of the HBT radii in equation (5.29) are simplified versions of (2.32) when measuring the 2^{nd} order event plane.

Using (5.28) and (5.29), the ϕ dependence of the transverse HBT radii were calculated for the two limiting cases of source anisotropy. It was found that while the presence of an anisotropic flow boost introduces oscillations in the radii, the phases and magnitudes of the oscillations are dominated by the spatial anisotropy. Figs. 5.15 and 5.16 show comparison plots of the ϕ dependence of the HBT fit parameters with various blast wave parameterizations. In Fig. 5.15, the transverse radii are compared to the blast wave modified with a solid elliptical source characterized by the parameters in Table 5.10. The full parameterization is shown as a black line, while the

separate contributions are shown for the momentum anisotropy (red dashed line) and the spatial anisotropy (green dotted line). A similar comparison is shown in Fig. 5.16 for a source anisotropy characterized by a density modulation. The results indicate that to describe both the $v_2(p_T)$ measurement and ϕ dependence of the HBT radii, the source spatial anisotropy must be dominated by the geometry of the source as opposed to its density. Assuming a geometry anisotropy in the emission region, an out–of–plane source extension $R_y = 11.7fm$ is found. An $s_2 = 0.037$, corresponds to an in–plane extension $R_x = 11.1fm$. The emission duration was also varied to achieve good agreement between the relative sizes of R_o^2 and R_s^2. The emission time obtained from the blast wave parameterization was $\tau = 2.2fm/c$.

The presence of positive ρ_a alone introduces oscillations in the transverse radii consistent in phase with those measured, yet the magnitude of the oscillations requires some additional spatial anisotropy. The oscillations introduced to the transverse radii from the s_2 parameters were found to be dependent upon the character of the modulation they described. When the modulation was described by an elliptic spatial extension, the oscillations obtained from a positive s_2 agreed in phase and when properly chosen could describe the ϕ dependence of the transverse radii alone. If the source was assumed circular in the transverse plane with a modulated source density, the oscillations from a positive s_2 introduced oscillations opposite those observed in the data in R_s^2 and R_{os}^2. The magnitude of the oscillations are also much reduced from those measured. In particular, the R_o^2 ϕ dependence is almost non–existent.

The freeze–out geometry obtained from the blast wave parameterization allows an estimation of the freeze–out time of the overlap region of the collisions. Weighting the multiplicity distribution by the approximate number of pairs generated, $n(n-1)/2$,

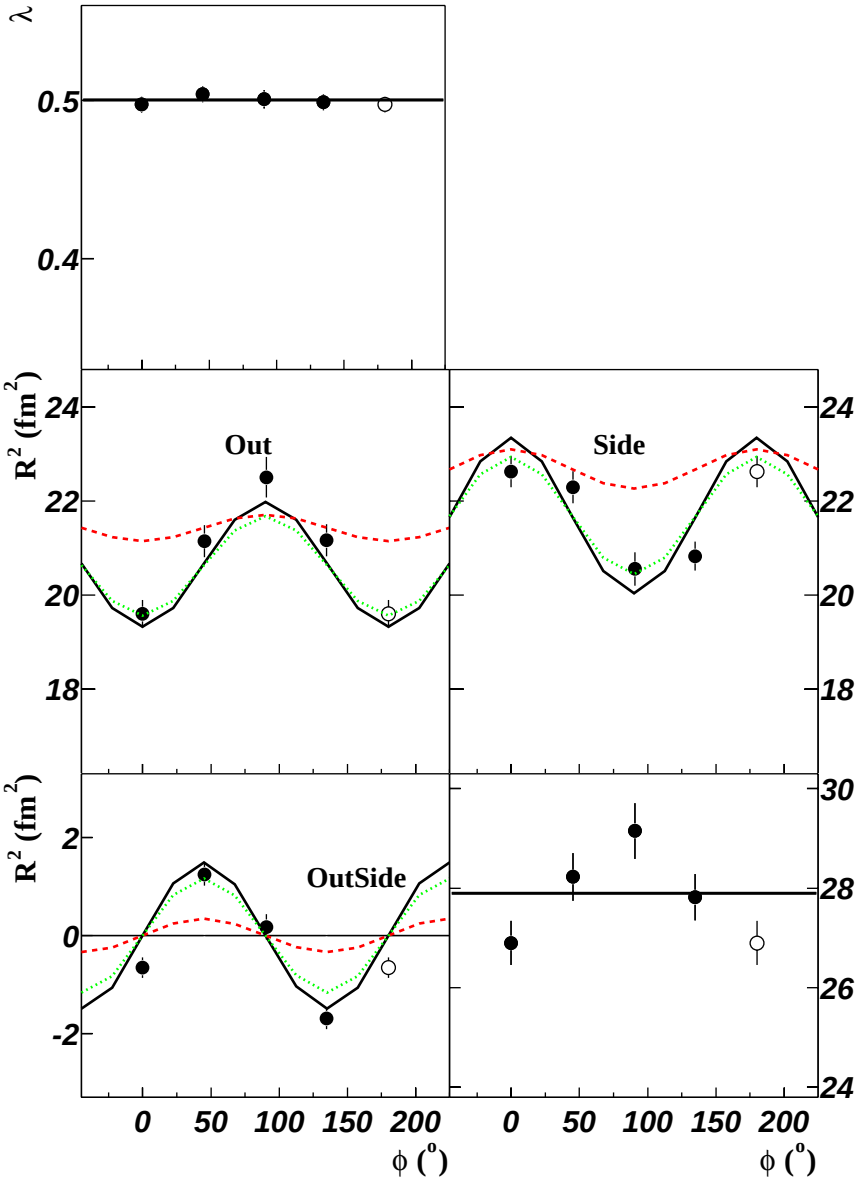

Figure 5.15: The (histogram bin content) corrected ϕ dependent HBT fit parameters with a comparison to the blast wave results using Table 5.10. The full blast wave calculation is shown as a black line, while the separate contributions are shown as a red dashed line ($\rho_a = 0.037$, $s_2 = 0$) and a green dotted line ($\rho_a = 0$, $s_2 = 0.037$).

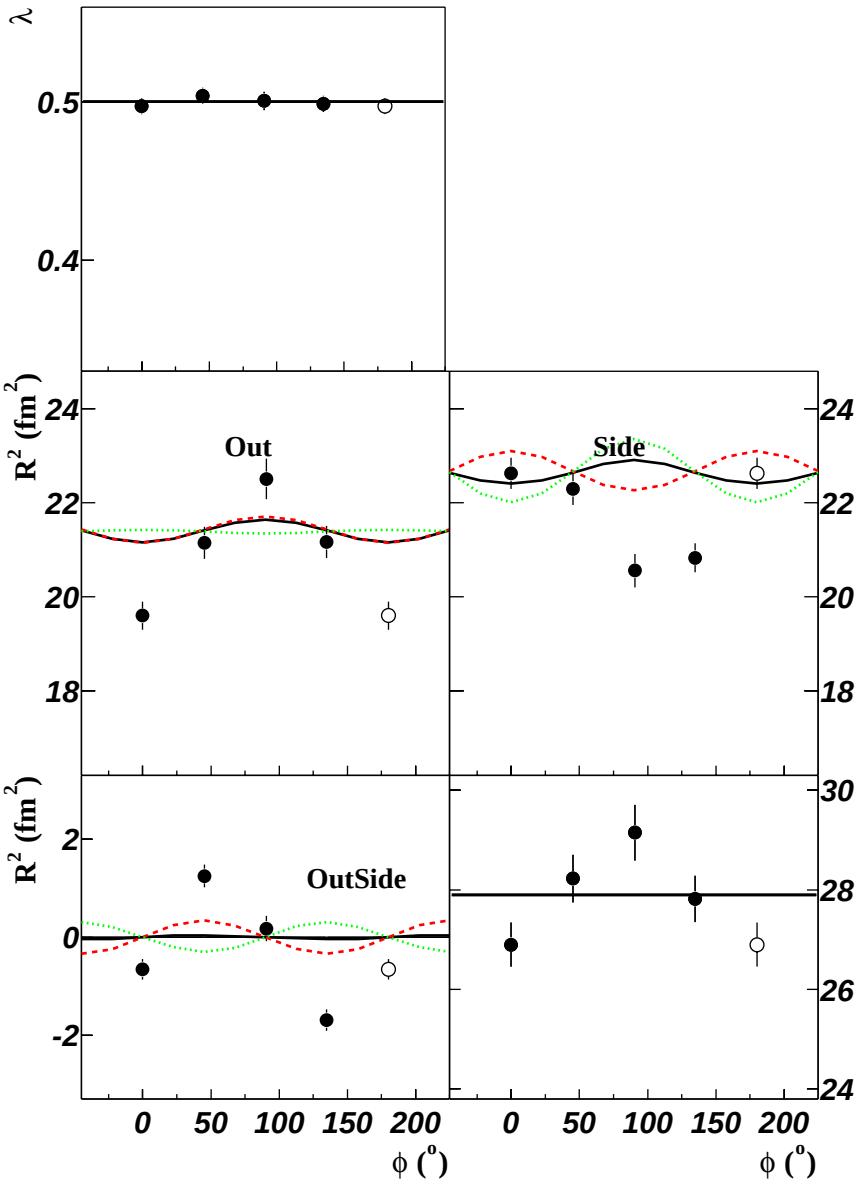

Figure 5.16: Same as Fig. 5.15 but for the density modulated source.

one can estimate the average impact parameter and aspect ratio, $\eta = R_y/R_x$, of the initial overlap region. For the minimum–bias events used in this analysis, an average centrality of 18% was found corresponding to an impact parameter of $\sim 4.2fm$. The extensions of the elongated source of the overlap region are related to the impact parameter via

$$R_x(b, R_{Au}) = R_{Au} - \frac{1}{2}b \tag{5.30}$$

$$R_y(b, R_{Au}) = \sqrt{R_{Au}^2 - \frac{1}{4}b^2}. \tag{5.31}$$

The "lengths of homogeneity" are then calculated as

$$\langle \tilde{x}^2 \rangle = \frac{2}{3}\left(\frac{A_0(R,b,\theta) - A_1(R,b,\theta) + A_2(R,b,\theta) - A_3(R,b,\theta)}{D(R,b,\psi)} \right) \tag{5.32}$$

$$\langle \tilde{y}^2 \rangle = \frac{2}{3}R^4\left(\frac{B_0(R,b,\psi) - B_1(R,b,\psi)}{D(R,b,\psi)} \right) \tag{5.33}$$

where

$$\begin{aligned}
A_0(R,b,\theta) &= \theta\left(\frac{3}{8}R^4 + 6R^2b^2\right), \\
A_1(R,b,\theta) &= \sin(\theta)\left(\frac{9}{2}R^3b - 8Rb^3\right), \\
A_2(R,b,\theta) &= \sin(2\theta)\left(\frac{1}{4}R^4 + 3R^2b^2\right), \\
A_3(R,b,\theta) &= \frac{1}{2}\sin(3\theta)R^3b + \frac{1}{32}\sin(4\theta)R^4, \\
B_0(R,b,\psi) &= \frac{3}{16}\pi - \frac{3}{8}\psi, \\
B_1(R,b,\psi) &= \frac{1}{4}\sin(2\psi) + \frac{1}{32}\sin(4\psi), \\
D(R,b,\psi) &= \frac{\pi}{2}R^2 - 2R^2\left(\frac{\psi}{2} + \frac{\sin(2\psi)}{4}\right), \\
\theta &= \sin^{-1}\left(\frac{\sqrt{R^2-4b^2}}{R}\right), \text{ and} \\
\psi &= \sin^{-1}\left(\frac{2b}{R}\right).
\end{aligned} \tag{5.34}$$

The overlap region can be approximated by an ellipse with equivalent lengths of homogeneity. The aspect ratio of the corresponding ellipse is found to be $\eta = 1.31$. The positive elliptic flow present at RHIC increases the in–plane radius faster than out–of–plane thus reducing the aspect ratio as a function of time, as seen in Fig. 5.17. Fig. 5.17 shows the $\epsilon_x(t)$ parameter, where

$$\epsilon_x = \frac{\langle\langle y^2 - x^2\rangle\rangle}{\langle\langle y^2 + x^2\rangle\rangle}, \tag{5.35}$$

for a hydrodynamic simulation and shows the evolution of the almond shaped overlap region as a function of time after the collision. The s_2 parameters from the blast wave provide a measurement of the aspect ratio of the freeze–out configuration of the emission region from (5.27) giving $\eta = 1.05$. By including time dependence in the aspect ratio,

$$\eta = \eta(t) = \frac{R_y(t)}{R_x(t)} = \frac{R_y(0) + \langle v_y\rangle t}{R_x(0) + \langle v_x\rangle t}, \tag{5.36}$$

the freeze–out time obtained is $t = 11.2 fm/c$. The expansion velocities, v_x and v_y, are obtained from the blast wave parameters, ρ_0 and ρ_a from Table 5.10. This time represents the elapsed time from the impact to the time pion emission ceases and includes the emission timescale also found from the blast wave, $\tau = 2.2 fm/c$. Model predictions which incorporate a phase transition to a QGP predict a dramatic increase in the lifetime of the particle source, as seen in Fig. 1.3, followed by a decrease in the lifetime as the source becomes explosive. The short life–time and large flow velocities are indicative of an explosive source suggesting that the energy densities created at RHIC may be well above the threshold for creating QGP and are producing explosive sources.

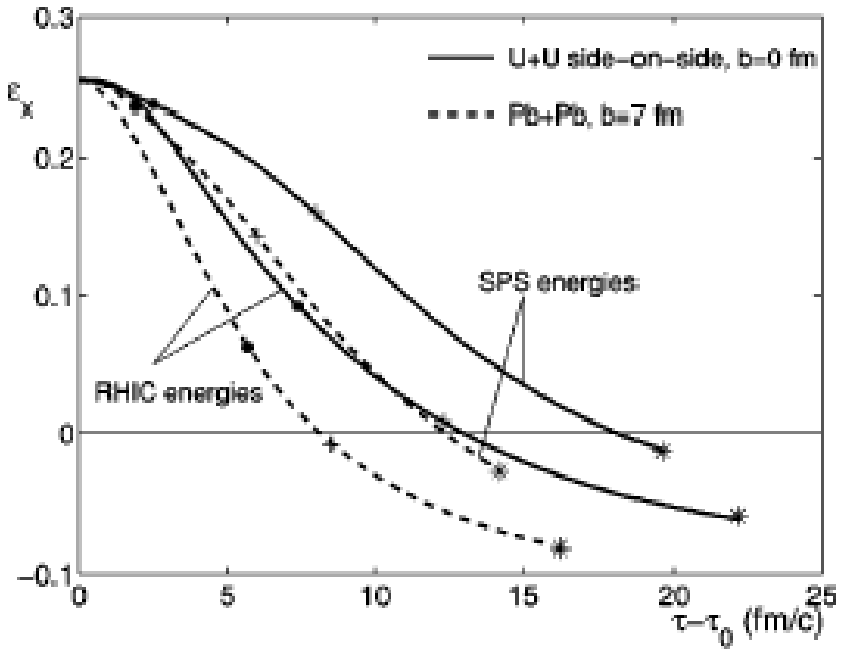

Figure 5.17: Time dependence of the eccentricity parameter for hydrodynamic simulations as SPS and RHIC collision energies.

Presently, the blast wave has been successful in reproducing a wide variety of measurements made by STAR within a consistent set of parameters. In addition to describing the measurements of elliptic flow and the ϕ dependence of the transverse HBT radii, the blast wave also can be used to extract parameters to describe the particle spectra and HBT correlations from non–identical particle pairs. Fits to the spectra with the blast wave parameterization provide information about the source temperature T and the radial flow boost ρ_0. Results from fitting the STAR particle spectra indicate a temperature and flow boost consistent with that which describes both the elliptic flow and $R^2_{o,s,os}(\phi)$ [66]. Comparison with dynamical models suggest a more complex freeze–out process is present at RHIC. Hydrodynamics is successful at reproducing much of the dynamical properties at RHIC yet fails to predict accurate HBT radii [67]. Including a less dense model to reproduce the later stages of the emission region, such as RQMD, increases the difference between model and data [2]. In addition, the inclusion of a hadronic scattering stage increases the lifetime of the emission region and predicts a change in the average source shape, as seen in Fig. 1.4, in contrast to what the STAR data describe.

CHAPTER 6

CONCLUSIONS

The STAR experiment was designed as a large acceptance detector ideally suited to provide correlations between many observables on an event–by–event basis. By correlating the measurement of several quantities, a more detailed characterization of the freeze–out configuration is possible which will further constrain dynamical models. In the summer of 2000, the collisions provided by the RHIC accelerator complex created the most dense state of matter for experimentalists to study in a laboratory by colliding Au nuclei at $\sqrt{s_{NN}} = 130 AGeV$.

Further progress with this analysis would be possible with some modifications to the STAR detector. The addition of FTPC's should provide the ability to reconstruct the 1^{st} order event plane thereby giving a full 3–dimensional view of the particle emitting source. Year 2 data taken in the summer and fall of 2001 are expected to expand the systematics available for the azimuthally sensitive analysis. The increased statistics will provide an opportunity to perform the first systematic studies of pion interferometry relative to the event plane to improve the resolution of the picture of the fundamental properties of compressed nuclear matter which are being drawn from STAR data.

The study of interferometry in heavy ion collisions provides a method to probe the spatial and dynamic properties of the emission region. Noncentral collisions are inherently anisotropic in both spatial and momentum space. The analysis of the ϕ dependence of the HBT radii provides a wealth of information about the freeze–out conditions of the emission region. Although both hydrodynamic and molecular dynamic models fail to accurately reproduce the magnitudes of the R_o^2 and R_s^2 radii, both correctly predict the phases and magnitudes of the oscillations in the ϕ dependence of the transverse radii: R_o^2, R_s^2, and R_{os}^2 seen in both the π^- and π^+ separate analyses in addition to the combined charged pion analysis. However, the "most realistic" scenario of hydrodynamics + RQMD get the wrong shape, see Fig. 5.17.

A hydrodynamic inspired blast wave parameterization of the freeze–out configuration was introduced to describe the STAR $v_2(p_T)$ measurement. The results of the fit indicated the presence of a spatial anisotropy, evidenced by a nonzero s_2 parameter. The blast wave was further modified to account for a more realistic solid emission region. It was found that the data could be reproduced using the same parameters as the v_2 analysis while also including both an emission timescale, τ, and an out–of–plane radius, R_y. The modified blast wave reproduces the ϕ dependence of the transverse HBT radii when the s_2 parameter characterized an out–of–plane extended source. The spatial anisotropy corresponds to a source eccentricity $\eta = R_y/R_x \approx 1.05$. This may be compared to $\sim 1.3 - 1.4$ at the AGS, which was consistent with entrance channel overlap configuration.

Using an estimate for the geometry of the initial overlap region and the average freeze–out geometry obtained through the blast wave parameterization, an estimate for the source life time was found to be $t \approx 11.2 fm/c$. The similarity of the sizes of R_o^2

and R_s^2 is also suggestive of a short lived source. Using a blast wave parameterization of the freeze–out conditions, the ϕ dependence of the transverse radii indicate a emission duration, $\tau \approx 2.2 fm/c$. Combined with the strong dynamics found in the radial and elliptic flow, these results are strong indicators of an explosive source, possibly well above the threshold for creating a quark–gluon plasma.

APPENDIX A

RELEVANT VARIABLES

The STAR detector is located at the ∼6 o'clock position, at the southern end of the RHIC collider ring. The coordinate system is defined to be right–handed with the $+z$ axis defined by the direction of the clockwise RHIC beam, approximately west. Positive y is defined to point vertically upwards, and the $+x$ axis is perpedicular to both and points south. The origin of the coordinate system is located at the center of the STAR solonoidal magnet [68].

In heavy ion experiments, the standard variables to represent the motion of the particle is (p_T, ϕ, y) where p_T is the transverse momentum of the particle relative to the beam, ϕ is the direction of transverse motion, and y is the rapidity. The rapidity of a particle is a measure of its forward (beam direction) energy and is defined by:

$$y = \frac{1}{2} \ln \Big(\frac{E + p_z}{E - p_z} \Big). \tag{A.1}$$

Rapidities are invariant under Lorentz transformations making it easy to shift particle rapidities to a boosted frame and hence allow comparisons of results of different experiments. The rapidity can be approximated by the psuedorapidity,

$$\eta = \frac{1}{2} \ln \Big(\frac{1 + \cos(\theta)}{1 - \cos(\theta)} \Big) \tag{A.2}$$

where θ is the angle between the beam axis and the momentum of the particle. In the limit of massless particles, $y = \eta$. The transverse momentum, p_T, of a particle is defined as the length of the momentum vector perpendicular to the beam axis,

$$p_T = \sqrt{p_x^2 + p_y^2}. \tag{A.3}$$

To measure the energy exiting the collision fireball perpendicular to the beam axis, one uses the transverse mass,

$$m_T = \sqrt{p_T^2 + m^2}. \tag{A.4}$$

An invariant form of the momentum difference is defined as q–invariant, q_{inv}, and is the standard variable used in 1–dimensional HBT analyses. It is defined as the length of the 4–momentum difference between to particles,

$$q_{inv} = \sqrt{q^\mu q_\mu} = \sqrt{-((\Delta E)^2 - (\Delta \mathbf{p})^2)}. \tag{A.5}$$

The s_2' parameter used by Teaney and Shuryak to describe the spatial anisotropy is a measure of the difference in length of the transverse radii:

$$s_2' = \left\langle \frac{x^2 - y^2}{x^2 + y^2} \right\rangle. \tag{A.6}$$

This can be related to the s_2 parameter used in the blast wave model through (5.27)

$$s_2' \approx \left\langle \frac{\sqrt[3]{(\frac{1+2s_2}{1-2s_2})^2} - 1}{\sqrt[3]{(\frac{1+2s_2}{1-2s_2})^2} + 1} \right\rangle. \tag{A.7}$$

BIBLIOGRAPHY

[1] D.H. Rischke and M. Gyulassy. The Time–Delay Signature of Quark–Gluon–Plasma Formation in Relativistic Nuclear Collisions. *Nucl. Phys. A.*, 608:479, 1996.

[2] D. Teaney, J. Lauret, and E.V. Shuryak. A Hydrodynamic Description of Heavy Ion Collisions at the SPS and RHIC. *nucl–th/0110037*, 2001.

[3] C. Adler et al. (STAR Collaboration). Pion Interferometry of $\sqrt{s_{NN}} = 130GeV$ Au + Au Collisions at RHIC. *Phys. Rev. Lett.*, 87:082301, 2001.

[4] M.A. Lisa, et al. (E895 Collaboration). Bombarding Energy Dependence of π^- Interferometry at the Brookhaven AGS. *Phys. Rev. Lett.*, 84:2798, 2000.

[5] I.G. Bearden, et al. (NA44 Collaboration). High energy Pb + Pb collisions viewed by pion interferometry. *Phys. Rev. C*, 58:1656, 1998.

[6] R. Soltz, et al. (E866 Collaboration). Systematic investigation of two–pion correlations at the AGS. *Nucl. Phys. A.*, 661:439c, 1999.

[7] S.V. Afanasiev, et al. (NA49 Collaboration). New results from NA49. *Nucl. Phys. A.*, 698:104a, 2002.

[8] M.A. Lisa et al. (E895 Collaboration). Azimuthal Dependence of Pion Interferometry at the AGS. *Phys. Lett. B*, 496:1, 2000.

[9] M.A. Lisa. The STAR–TPC Clusterfinder/Hitfinder – STAR Note 238. *STAR Note*, SN0238, 1996.

[10] I. Johnson. private communication.

[11] U. Heinz and P.F. Kolb. Emission angle dependent pion interferometry at RHIC and beyond. *hep-ph/0206278*, 2002.

[12] C. Adler et al. (STAR Collaboration). Identified Particle Elliptic Flow in Au + Au Collisions at $\sqrt{s_{NN}} = 130GeV$. *Phys. Rev. Lett.*, 87:182301, 2001.

[13] A.A. Penzias and R.W. Wilson. A Measurement of Excess Antenna Temperature at 4080 mc/s. *ApJ*, 42:419, 1965.

[14] J.C. Mather et al. A Preliminary Measurement for the Cosmic Microwave Background Spectrum by the Cosmic Background Explorer. *ApJ*, 354:L37–L34, 1990.

[15] S. Pratt et al. Detailed predictions for two–pion correlations in ultrarelativistic heavy–ion collisions. *Phys. Rev. C.*, 42:2646, 1990.

[16] M. Gyulassy et al. Hot Spots and Turbulent Initial Conditions of Quark–Gluon Plasmas in Nuclear Collisions. *Nucl. Phys. A.*, 613:397, 1997.

[17] D. Teaney and E.V. Shuryak. Unusual Space–Time Evolution for Heavy Ion Collisions at High Energies due to the QCD Phase Transition. *Phys. Rev. Lett.*, 83:4951, 1999.

[18] R. Hanbury-Brown and R.Q. Twiss. A Test of a New Type of Stellar Interferometer of Sirius. *Nature*, 178:1046, 1956.

[19] G. Goldhaber et al. Influence of Bose–Einstein Statistics on the Antiproton–Proton Annihilation Process. *Phys. Rev.*, 120:300, 1960.

[20] S. Bekele et al. (STAR Collaboration). Correlations of Charge and Neutral kaons in AuAu collisions at $\sqrt{s} = 200GeV/NN$ using the solenoidal tracker at RHIC (STAR). Poster presented The XVI International Conference on Ultrarelativistic Nucleus–Nucleus Collisions, 2002.

[21] U. Wiedemann and U. Heinz. Particle Interferometry for Relativistic Heavy–Ion Collisions. *Phys. Rep.*, 319:145, 1999.

[22] M. Gyulassy et al. Pion interferometry of nuclear collisions. I. Theory. *Phys. Rev. C.*, 20:2267, 1979.

[23] S. Pratt. Pion Interferometry for Exploding Sources. *Phys. Rev. Lett.*, 53:1219, 1984.

[24] G.C. Wick. The Evaluation of the Collision Matrix. *Phys. Rev.*, 80, 1950.

[25] Yu.M. Sinyukov and Lörstad. On intensity interferometry at high multiplicities. *Z. Phys. C.*, 69:587, 1994.

[26] S. Chapman, J.R. Nix, and U. Heinz. Extracting source parameters from Gaussian fits to two–particle correlations. *Phys. Rev. C.*, 52:2694, 1995.

[27] M.A. Lisa, U. Heinz, and U.A. Wiedemann. Tilted Pion Sources from Azimuthally Sensitive HBT Interferometry. *Phys. Lett. B*, 489:287, 2000.

[28] M.G. Bowler. Extended sources, final state interactions, and Bose–Einstein correlations. *Z. Phys. C*, 39:81, 1988.

[29] S. Pratt. Coherence and Coulomb effects on pion interferometry. *Phys. Rev. D.*, 33:72, 1986.

[30] A. Messiah. *Quantum Mechanics*. John Wiley & Sons, 1961.

[31] W.A. Zajc et al. Two–pion correlations in heavy ion collisions. *Phys. Rev. C.*, 29:2173, 1984.

[32] H.W. Barz et al. Coulomb effects on particle spectra in relativistic nuclear collisions. *Phys. Rev. C.*, 57:2536, 1998.

[33] G. Bertsch et al. Pion interferometry in ultrarelativistic heavy–ion collisions. *Phys. Rev. C.*, 37:1896, 1988.

[34] U. Wiedemann. Two–particle interferometry for noncentral heavy–ion collisions. *Phys. Rev. C*, 57:266, 1998.

[35] H. Heiselberg and A. Levy. Elliptic flow and Hanbury–Brown–Twiss correlations in noncentral nuclear collisions. *Phys. Rev. C*, 59:2716, 1999.

[36] H. Heiselberg. Emission Times and Opacities from Interferometry in Noncentral Relativistic Nuclear Collisions. *Phys. Rev. Lett.*, 82:2052, 1999.

[37] G.T. van Belle et al. Altair's Oblateness and Rotation Velocity from Long–Baseline Interferometry. *ApJ*, 559:1155, 2001.

[38] J.-Y. Ollitrault. Anisotropy as a signature of transverse collective flow. *Phys. Rev. D*, 46:229, 1992.

[39] A.M. Poskanzer and S.A. Voloshin. Methods for analyzing anisotropic flow in relativistic nuclear collisions. *Phys. Rev. C*, 58:1671, 1998.

[40] J.-Y. Ollitrault. Determination of the reaction plane in ultrarelativistic nuclear collisions. *Phys. Rev. D*, 48:1132, 1993.

[41] C. Pinkenberg et al. (E895 Collaboration). Elliptic Flow: Transition from Out–of–Plane to In–Plane Emission in Au + Au Collisions. *Phys. Rev. Lett.*, 83:1295, 1999.

[42] H. Liu et al. (E895 Collaboration). Sideward Flow In Au + Au Collisions between 2A and 8A GeV. *Phys. Rev. Lett.*, 84:5488, 2000.

[43] J. Barrette et al. (E877 Collaboration). Directed flow and particle production in $Au + Au$ collisions from experiment E877 at the AGS. *Nucl. Phys. A.*, 590:259c, 1995.

[44] K.H. Ackermann et al. (STAR Collaboration). Elliptic Flow in Au + Au Collisions at $\sqrt{s_{NN}} = 130GeV$. *Phys. Rev. Lett.*, 86:402, 2001.

[45] J Dunlop. private communication.

[46] J. Harris et al. STAR: Conceptual Design Report. Technical Report PUB–5347, DOE, 1992.

[47] J. Harris et al. STAR Project conceptual Design Report Update. Technical Report PUB–5347 Rev., DOE, 1993.

[48] S.J. Sanders, (BRAHMS Collaboration). Charged Particle Multiplicities at BRAHMS. In *Proceedsings of the* 17^{th} *Winter Workshop on Nuclear Dynamics*, 2001.

[49] W. Betts et al. Studies of Several Wire and Pad Geometries for the STAR TPC. *STAR Note*, SN0263, 1996.

[50] G.J. Kunde et al. A Ring Imaging Cherenkov Detector for STAR. *STAR Note*, SN0349, 1998.

[51] H. Crawford et al. CTB Requirements Document. *STAR Note*, 1998.

[52] J.T. Mitchell and I.M. Sakrejda. Tracking for the STAR TPC: Documentation and User's Guide. *STAR Note*, SN0190, 1994.

[53] S. Margetis and D. Cebra. Main Vertex reconstruction in STAR. *STAR Note*, SN0089, 1992.

[54] W. Blum and L. Rolandi. *Particle detection with drift chambers*. Springer–Verlag, 1993.

[55] D.E. Groom, (Particle Data Group). Review of Particle Physics. *Eur. Phys. J. C*, 15:1–878, 2000.

[56] A. Marín et al. Detection of charged pion and protons in the segmented electromagnetic calorimeter TAPS. *Nucl. Instr. and Meth. A.*, 417:137, 1998.

[57] Manuel Calderón de la Barca Sanchez. *Charged Hadron Spectra in Au + Au Collisions at* $\sqrt{s_{NN}} = 130GeV$. PhD thesis, Yale University, 2001.

[58] U. Heinz et al. Symmetry constraints for the emission angle dependence of Hanbury–Brown–Twiss radii. *Phys. Rev. C*, 66:044903.

[59] D. Magestro. private communication.

[60] M.A. Lisa and R.C. Wells. Model Calculations of Azimuthally–sensitive HBT in STAR, 2001.

[61] B. Tomášik et al. Space–time Characteristics of the Fireball from HBT Interferometry. *Acta. Phys. Slov.*, 47:81, 1997.

[62] E. Kreyszig. *Introductory Mathematical Statistics*. John Wiley & Sons, Inc., 1970.

[63] U. Heinz and P.F. Kolb. Two RHIC puzzles: Early thermalization and the HBT problem. In 18^{th} *Winter Workshop on Nuclear Dynamics*, 2002.

[64] P.J. Siemens and J.O. Rasmussen. Evidence for a Blast Wave from Compressed Nuclear Matter. *Phys. Rev. Lett.*, 42:880, 1979.

[65] P. Huovinen et al. Radial and elliptic flow at RHIC: further predictions. *Phys. Lett. B*, 503:58, 2001.

[66] M. Kaneta et al. (STAR Collaboration). Chemical and Kinetic Freeze–out Properties at RHIC. Poster presented The XVI International Conference on Ultra-relativistic Nucleus–Nucleus Collisions, 2002.

[67] U. Heinz and P.F. Kolb. Early thermalization at RHIC. *Nucl. Phys. A.*, 702:269, 2002.

[68] H Matis. STAR Coordinate System. *STAR Note*, CSN0121, 1993.